

**Investigation of up and down-converting rare earth ions
doped ZnTiO₃ for photovoltaic applications**

by

Sefako John Mofokeng

(Master of Science in Nanoscience)

A thesis submitted in partial fulfilment of the requirements for the degree

Doctor of Philosophy

in the

College of Science, Engineering and Technology

Department of Physics

at the

University of South Africa

Republic of South Africa

Promoter: Professor M.S. Dhlamini

Co-Promoters: Doctor L.L. Noto

Professor O.M. Ntwaeaborwa

Professor B.M. Mothudi

October 2019

“For I know the plans I have for you, declares the LORD, plans for welfare and not for evil, to give you a future and a hope.”

– Jeremiah 29:11

***This thesis is dedicated to my son
Lebohang Tlhonolofatso Mofokeng***

Declaration

(i) I, **Sefako John Mofokeng**, declare that the Doctor of Philosophy degree research thesis or interrelated, publishable articles/published articles, that I herewith submit for the Doctor of Philosophy qualification at the University of South Africa is my independent work, and that I have not previously submitted it for qualification at another institution of higher education.

(ii) I, **Sefako John Mofokeng**, further declare that the title “Investigation of up and down-converting rare earth ions doped ZnTiO₃ for photovoltaic applications” is my own work and that all the sources that I have used or quoted have been indicated and acknowledged by means of complete references.

Signature



Date

October 2019

Acknowledgements

First and foremost, I would like to give thanks to God, Almighty for strength, wisdom and his grace to help me complete this research. With Him, nothing is impossible and without Him I would not have the wisdom and physical abilities to do it especially in difficult times. I am very grateful to God who has carried me from the beginning until the end. I am sending sincere gratitude to:

- My promoter, **Prof. Mokhotjwa Simon Dhlamini** for having accepted to be my promoter in PhD research and his encouragement, support and esteemed guidance along the length of my PhD research.
- It is my pleasure to express deepest thanks to my co-promoter **Dr. Luyanda L. Noto** for his patience, guidance, suggestions and all the valuable inputs in analysis of data and helping me organize my ideas during my experimental work and write up of manuscripts and thesis.
- My other co-promoters, **Prof. Odirileng M. Ntwaeaborwa and Prof. Bakang M. Mothudi** for valuable comments and generous contribution of knowledge during the course of my research.
- **Prof. Robin E. Kroon** from University of the Free State for his valuable assistance in photoluminescence measurements and analysis of data.
- **Mr. Lucas Erasmus** from University of the Free State for his valuable assistance with Pulsed Laser Deposition (PLD) system.
- **Dr. M.M. Duvenhage** from University of the Free State for TOF-SIMS measurements.
- University of South Africa physics department staff members, fellow students and my friends for their assistance, valuable inputs and discussions in this research.
- I am grateful for the financial support from the National Research Foundation (NRF) and University of South Africa (UNISA).

- Most importantly, I would like to thank my family for their various forms of support, constant source of love and strength which helped sustain me throughout this endeavor. I am also very grateful to my family to be part of my vision and their continuous guidance in my life.

Abstract

We are living in an age where the demand for energy is growing rapidly. This means that supplies to easily accessible oil and natural gas is unlikely to keep up with the demand as times goes on. The world will have to use energy more efficiently and increase its use of other sources of energy. This study is aiming at developing materials that will improve the power conversion efficiency of photovoltaic cells by using up and down-converting phosphor materials. $\text{ZnTiO}_3\text{-Zn}_2\text{TiO}_4$ composite and ZnTiO_3 phosphors doped with Er^{3+} , Yb^{3+} , Eu^{3+} and Al^{3+} , which display up and down-converted luminescence were synthesized by a simple high temperature conventional solid state reaction method. The structure, particle morphology, absorption, photoluminescent properties and elemental distribution were analyzed using X-ray diffraction (XRD), scanning electron microscopy (SEM), UV-Vis-NIR absorption spectrometer, photoluminescence (PL) spectroscopy and time of flight secondary ion mass spectroscopy (TOF-SIMS), respectively.

$\text{ZnTiO}_3\text{-Zn}_2\text{TiO}_4$ composite doped with different concentration of Er^{3+} ions was synthesized via solid state chemical reaction method at 1100 °C. The X-ray diffraction (XRD) confirmed the crystallization of both the hexagonal ZnTiO_3 and cubic spinel Zn_2TiO_4 phases of the composite. The SEM images of $\text{ZnTiO}_3\text{-Zn}_2\text{TiO}_4\text{:Er}^{3+}$ composite showed that the particle morphology was made up of faceted hexagons. Furthermore, the $\text{ZnTiO}_3\text{-Zn}_2\text{TiO}_4\text{:Er}^{3+}$ phosphors were excited in the near-infrared (NIR) region using a laser diode with a wavelength of 980 nm and displayed both green and red up-conversion emission bands in the visible range at 543, 553, 650 – 670 nm. These emission bands correspond to ${}^2\text{H}_{11/2}$, ${}^4\text{S}_{1/2} \rightarrow {}^4\text{I}_{15/2}$ and ${}^4\text{F}_{9/2} \rightarrow {}^4\text{I}_{15/2}$ transitions of Er^{3+} ions. However, the interaction mechanisms involved in the up-conversion process of $\text{ZnTiO}_3\text{-Zn}_2\text{TiO}_4\text{:Er}^{3+}$ phosphor is discussed with the help of an energy-level schematic diagram and the number of the photons involved in the up-conversion luminescence process were of a double photon mechanism. The decay lifetimes were studied by fitting the luminescence decay curve with a single-component exponential decay.

Er^{3+} and Yb^{3+} incorporated zinc titanate (ZnTiO_3) phosphor powders were synthesized using conventional solid-state reaction method at 800 °C. A $\text{ZnTiO}_3\text{:Er}^{3+},\text{Yb}^{3+}$ phosphor that resembled an eandrewsite single phase with space group $R\text{-}\bar{3}$ (148) was obtained, as proven

by X-ray diffraction (XRD). The SEM image showed a surface morphology composed of agglomerated irregular shaped particles. The energy band gap of ZnTiO₃ was engineered by incorporating different concentration of the dopant ions. After irradiating ZnTiO₃:Er³⁺ with a 980 nm laser beam, the phosphor up-converted the photon energy to display green and red emissions in the visible range that were positioned at 527, 545 and 665 nm. Enhancement of the luminescence intensity of ZnTiO₃:Er³⁺ phosphor was achieved by variation of Er³⁺ concentration. Co-doping with Yb³⁺ ions proved to be effective in enhancing the luminescence intensity of the optimized Er³⁺ ion emission and new emission bands at 410 and 480 nm, through an energy transfer mechanism were observed. The enhancement of the lifetime of the up-conversion luminescence was also achieved by co-doping ZnTiO₃:Er³⁺ phosphor with Yb³⁺ ion. The energy transfer mechanisms involved in Er³⁺- Yb³⁺ co-doped ZnTiO₃ phosphor was illustrated and discussed in detail.

The ZnTiO₃:Er³⁺, Yb³⁺ thin films were successfully deposited by pulsed laser deposition (PLD) by varying the silicon (100) substrate temperature. The distribution of the ions in the films was investigated and the TOF-SIMS showed that the ions were homogeneously distributed throughout the ZnTiO₃ host lattice which indicated a successful incorporation of the Er³⁺ and Yb³⁺ ions. The optical response of the phosphors revealed that the reflectance percentages of the ZnTiO₃:Er³⁺, Yb³⁺ vary with the silicon substrate temperature due to the differences in the thickness and morphological roughness of the thin films. The ZnTiO₃:Er³⁺, Yb³⁺ thin films also exhibited up-conversion emission from Er³⁺ electronic transitions, with violet, blue, green and red emission lines at 410, 480, 525, 545 and 660 nm from ²H_{9/2} → ⁴I_{15/2}, ⁴F_{7/2} → ⁴I_{15/2}, ²H_{11/2} → ⁴I_{15/2}, ⁴S_{3/2} → ⁴I_{15/2} and ⁴F_{9/2} → ⁴I_{15/2} transitions, respectively. These up-conversion emissions were enhanced by increasing the silicon substrate temperature during the deposition.

ZnTiO₃ host co-doped with Eu³⁺ and Al³⁺ was synthesized by solid state reaction to convert the UV photons to visible photons. Charge compensation effects of Al³⁺ incorporated ZnTiO₃:Eu³⁺ as a co-dopant ion was reported in detail. The structural and morphological characterization show that the addition of Eu³⁺ and Al³⁺ does not affect the phase formation and the surface morphology of the host. The visible emission intensity of Eu³⁺ ions for an optimal concentration of 2 mol% under 395 nm excitation, was enhanced by incorporating Al³⁺. The energy level diagram showing the charge compensation mechanism was proposed for the co-doped system.

Keywords

Luminescence, conventional solid-state reaction, up-conversion, down-conversion, energy transfer, rare earth ions, zinc titanates, erbium, ytterbium, europium, charge compensator.

Acronyms

❖ Al³⁺	Aluminium trivalent ions
❖ CIE	Commission Internationale de l'Eclairage
❖ DCL	Down-conversion luminescence
❖ Eu³⁺	Europium trivalent ions
❖ Er³⁺	Erbium trivalent ions
❖ ET	Energy transfer
❖ FE-SEM	Field emission scanning electron microscopy
❖ LED	Light emitting diode
❖ Ln³⁺	Lanthanide ions
❖ PL	Photoluminescence
❖ PLD	Pulsed Laser Deposition
❖ PV	Photovoltaic cells
❖ RE³⁺	Rare earth ions
❖ Si	Silicon
❖ TOF-SIMS	Time of Flight Secondary Ion Mass Spectroscopy
❖ UCL	Up-conversion luminescence
❖ UV-Vis -NIR	Ultraviolet-visible-near infrared spectroscopy
❖ XRD	X-ray diffraction
❖ Yb³⁺	Ytterbium trivalent ions

Table of contents

Declaration	ii
Acknowledgements	iii
Abstract	v
Keywords	vii
Acronyms	vii
Table of contents	viii
List of Figures	xiii
List of Tables	xvii
Chapter 1: Introduction	1
1.1. Renewable energy	1
1.2. Problem statement	2
1.3. Research aim and objectives	3
1.3.1. Aim of the study	3
1.3.2. Objectives of the study	3
1.4. Organization of the thesis	3
1.4.1. Supervision	3
1.4.2. Collaborations	4
1.5. Thesis layout	4
1.6. References	5
Chapter 2: Theoretical Background	7
2.1. Introduction	7
2.2. Solar cells	7
2.3. Dye-sensitized solar cells	8
2.4. Fundamentals of luminescence	9
2.4.1. Intrinsic luminescence	11

2.4.2. Extrinsic luminescence	11
2.5. ZnTiO ₃ nanoparticles	11
2.6. Up-conversion mechanism	13
2.7. Down-conversion mechanism	14
2.8. Rare earth ions	15
2.9. Energy transfer mechanism	18
2.10. Synthesis and film fabrication	20
Chapter 3: Experimental Techniques	27
3.1. Introduction	27
3.2. X-ray Diffractometer	27
3.3. Field Emission Scanning Electron Microscopy	29
3.4. UV-Vis-NIR absorption Spectroscopy	30
3.5. Photoluminescence Spectroscopy	32
3.6. Time-of-Flight Secondary Ion Mass Spectrometry	34
3.7. References	36
Chapter 4: Structural and optical evaluation of NIR up-converting Er³⁺ doped ZnTiO₃-Zn₂TiO₄ composite phosphor	38
4.1. Introduction	38
4.2. Experimental procedure	39
4.3. Results and discussion	39
4.3.1. Structural and morphological analysis	39
4.3.2. UV-Vis-NIR analysis	41
4.3.3. Up-conversion analysis	42
4.4. Conclusion	43
4.5. References	45
Chapter 5: Structural and optical evaluation of NIR up-converting xmol%Er³⁺ doped ZnTiO₃-Zn₂TiO₄ composite phosphor	47

5.1. Introduction	47
5.2. Experimental procedure	48
5.3. Results and discussion	48
5.3.1. Structural analysis	48
5.3.2. Morphological analysis	50
5.3.3. UV-Vis analysis	51
5.3.4. Up-conversion luminescence analysis	52
5.4. Conclusion	56
5.5. References	58
Chapter 6: Up-conversion luminescence properties of Er³⁺ doped ZnTiO₃ phosphor ...	60
6.1. Introduction	60
6.2. Experimental procedure	61
6.3. Results and discussion	61
6.3.1. Structural analysis	61
6.3.2. Morphological analysis	62
6.3.3. UV-Vis-NIR analysis	63
6.3.4. Up-conversion luminescence analysis	64
6.4. Conclusion	71
6.5. References	72
Chapter 7: Up-conversion luminescence properties and energy transfer mechanism of ZnTiO₃: Er³⁺, Yb³⁺ phosphor	74
7.1. Introduction	74
7.2. Experimental procedure	76
7.3. Results and discussion	76
7.3.1. Structural analysis	76
7.3.2. Morphological analysis	77
7.3.3. UV-Vis-NIR analysis	78

7.3.4. Up-conversion luminescence analysis	79
7.4. Conclusion	87
7.5. References	88
Chapter 8: Up-conversion luminescence properties of ZnTiO₃: Er³⁺, Yb³⁺ thin films synthesized by pulsed laser deposition	
8.1. Introduction.....	92
8.2. Experimental procedure.....	93
8.3. Results and discussion	94
8.3.1. Structural and morphological analysis	94
8.3.2. TOF-SIMS analysis.....	96
8.3.3. UV-Vis-NIR analysis.....	100
8.3.4. Up-conversion luminescence analysis	100
8.4. Conclusion	105
8.5. References	106
Chapter 9: Al³⁺ charge compensation in ZnTiO₃:Eu³⁺ phosphor synthesized by conventional solid-state reaction method.....	
9.1. Introduction.....	108
9.2. Experimental results.....	109
9.3. Results and discussion	110
9.3.1. Morphological and structural analysis	110
9.3.2. Optical properties analysis.....	111
9.4. Conclusion	118
9.5. References	119
Chapter 10: Summary and Future work	
10.1. Summary.....	122
10.2. Future work.....	124
10.3. List of publications.....	125

10.4. Research presentations 127

List of Figures

Figure 2.1: Schematic diagram of a DSSCs. S and S* represents a ground and excited states of dye sensitizer molecule and S ⁺ represents a dye sensitizer hole (the oxidized dye molecules)	8
Figure 2.2: Jablonski schematic diagram showing the electronic states responsible for luminescence emission of ion A. The absorption of light is shown with a black arrow pointing upwards (A→A*) and the emission of light with the one pointing downwards (A*→A). The * indicate the excited state, R the radiative process and NR is the non-radiative process	10
Figure 2.3: (a-d) Basic principle of up-conversion mechanisms or processes in Ln ³⁺ doped up-conversion nanomaterials.....	13
Figure 2.4: (a-d) Schematic diagram for rare-earth ions down-conversion mechanisms	15
Figure 2.5: Dieke diagram showing energy level structure of rare-earths ions	16
Figure 2.6: Schematic diagram illustrating the ET mechanism	18
Figure 2.7: Schematic diagram of the spectral overlap of a donor emission and acceptor absorption	19
Figure 2.8: Schematic illustration of the energy transfer mechanisms, namely: (a) radiative energy transfer, (b) non-radiative energy transfer, and (c) phonon-assisted non-radiative energy transfer	20
Figure 2.9: Experimental set-up of the PLD system	21
Figure 3.1: Schematic diagram of Bragg reflection from a set of parallel planes	28
Figure 3.2: The configuration of X-ray diffraction system: Rigaku SmartLab 9 kW XRD...28	
Figure 3.3: Schematic diagram presenting FE-SEM operation mechanism	29
Figure 3.4: The illustration of several signals generated by the interaction of the electrons with specimen	30
Figure 3. 5: Schematic diagram of the optical layout of UV-Vis-NIR spectrophotometer. The abbreviations in this figure mean: deuterium lamp (DL), halogen lamp (HL), mirrors (M), filter-wheel (FW), slit assembly (SA), grating table (G), common beam mask (CBM), optional depolarizing filter (DP), chopper assembly (C), reference beam (R), sample beam (S), photomultiplier tube (PMT) detector and lead sulfide (PbS) detector	31
Figure 3.6: Illustration of a double beam UV-Vis instrument.....	32
Figure 3.7: Horiba Fluorolog [®] -3 Spectrofluorometer setup schematic	33

Figure 3.8: Schematic presentation of the ToF-Sims	34
Figure 4.1: X-ray Diffraction patterns of (a) $\text{ZnTiO}_3\text{-Zn}_2\text{TiO}_4$ and $\text{ZnTiO}_3\text{-Zn}_2\text{TiO}_4\text{:Er}^{3+}$ and (b) FE-SEM micrograph of $\text{ZnTiO}_3\text{-Zn}_2\text{TiO}_4\text{:Er}^{3+}$ phosphors annealed at 1100°C	40
Figure 4.2: Reflectance spectra of $\text{ZnTiO}_3\text{-Zn}_2\text{TiO}_4$ and $\text{ZnTiO}_3\text{-Zn}_2\text{TiO}_4\text{:Er}^{3+}$ phosphors. .	41
Figure 4.3: (a) PL Spectrum and (b) the CIE coordinate plot of $\text{ZnTiO}_3\text{-Zn}_2\text{TiO}_4\text{:Er}^{3+}$ phosphor.....	42
Figure 4.4: Luminescence decay curve of $\text{ZnTiO}_3\text{-Zn}_2\text{TiO}_4\text{:Er}^{3+}$ phosphor.	43
Figure 5.1: X-ray Diffraction patterns of $\text{ZnTiO}_3\text{-Zn}_2\text{TiO}_4$ and $\text{ZnTiO}_3\text{-Zn}_2\text{TiO}_4\text{:Er}^{3+}$ annealed at 1100°C	49
Figure 5.2: FE-SEM micrographs of (a) $\text{ZnTiO}_3\text{-Zn}_2\text{TiO}_4$ and (b) $\text{ZnTiO}_3\text{-Zn}_2\text{TiO}_4\text{:Er}^{3+}$ composites.....	50
Figure 5.3: (a) The diffuse reflectance spectra and (b) Kubelka Munk's plots of $\text{ZnTiO}_3\text{-Zn}_2\text{TiO}_4\text{:xmol}\%\text{Er}^{3+}$ ($0.0 \geq x \leq 1.0$ mol%).	51
Figure 5.4: (a) Up-conversion emission spectra and (b) CIE coordinate plot of $\text{ZnTiO}_3\text{-Zn}_2\text{TiO}_4\text{:Er}^{3+}$ composite phosphor.	53
Figure 5.5: (a) Energy level diagram of Er^{3+} ions and (b) power dependence of PL intensity curves.	55
Figure 5.6: Decay curve of $\text{ZnTiO}_3\text{-Zn}_2\text{TiO}_4\text{:Er}^{3+}$ composite phosphor.	56
Figure 6.1: X-ray Diffraction patterns of ZnTiO_3 and $\text{ZnTiO}_3\text{:Er}^{3+}$ annealed at 800°C	62
Figure 6.2: FE-SEM images of ZnTiO_3 and $\text{ZnTiO}_3\text{:}0.8\text{mol}\%\text{Er}^{3+}$ powders.	62
Figure 6.3: The diffuse reflectance spectra (a) and Kubelka Munk's plots (b) of ZnTiO_3 and $\text{ZnTiO}_3\text{:xmol}\%\text{Er}^{3+}$ phosphor.	63
Figure 6.4: Up-conversion emission spectra of (a) $\text{ZnTiO}_3\text{:xmol}\%\text{Er}^{3+}$ phosphor under 980 nm excitation wavelength and (b) comparison of integrated intensities of green and red emissions for the phosphors.....	65
Figure 6.5: The CIE colour chromaticity diagram of $\text{ZnTiO}_3\text{:xmol}\%\text{Er}^{3+}$ phosphors.	66
Figure 6.6: (a) Up-conversion emission spectra of $\text{ZnTiO}_3\text{:}0.8\text{mol}\%\text{Er}^{3+}$ phosphor under 980 nm excitation wavelength within a laser power range of 0 mW to 2563 mW and (b) logarithmic dependence of UC emission intensity as a function of logarithm of power of $\text{ZnTiO}_3\text{:}0.8\text{mol}\%\text{Er}^{3+}$ phosphor.	68
Figure 6.7: Schematic energy level diagram of Er^{3+} showing the possible energy transfer mechanism involved in UC process under an excitation of 980 nm.....	69

Figure 6.8: (a) Luminescence decay curves of the $^4S_{3/2} \rightarrow ^4I_{15/2}$ transition in $ZnTiO_3:Er^{3+}$ phosphor and (b) the mean lifetime as a function of Er^{3+} concentrations.	70
Figure 7.1: X-ray diffraction patterns of $ZnTiO_3:Er^{3+}, Yb^{3+}$ phosphors.....	77
Figure 7.2: FE-SEM micrographs of (a) $ZnTiO_3$, (b) $ZnTiO_3:0.8Er^{3+}, 0.7Yb^{3+}$ and (c) EDS spectra of $ZnTiO_3:0.8Er^{3+}, 0.7Yb^{3+}$ phosphors.....	77
Figure 7.3: (a) The diffuse reflectance spectra and (b) Kubelka Munk's plots of $ZnTiO_3$, $ZnTiO_3: Er^{3+}$ and $ZnTiO_3: Er^{3+}, Yb^{3+}$ phosphors.	79
Figure 7.4: Up-conversion emission spectra of (a) $ZnTiO_3:0.8mol\%Er^{3+}$ and (b) $ZnTiO_3:0.8mol\%Er^{3+}, xmol\%Yb^{3+}(y = 0.1 - 0.8 mol\%)$ phosphors under 980 nm excitation wavelength. (c) Comparison of integrated intensities of green and red emission emissions of $ZnTiO_3:0.8 mol\%Er^{3+}, xmol\%Yb^{3+}$ phosphors.	81
Figure 7.5: The CIE colour chromaticity diagram of $ZnTiO_3:0.8mol\%Er^{3+}, xmol\%Yb^{3+}$ phosphors.	81
Figure 7.6: (a) Power dependence of up-conversion emission spectra of $ZnTiO_3:0.8mol\%Er^{3+}, 0.7mol\%Yb^{3+}$ under 980 nm excitation wavelength within a laser power range of 96 to 1500 mW, together with (b) logarithmic dependence of intensity versus power of these samples, respectively.	83
Figure 7.7: Schematic energy level diagram of Er^{3+}/Yb^{3+} showing the possible energy transfer mechanism involved in UC process under an excitation of 980 nm.....	85
Figure 7.8: Decay curves of the $^4F_{9/2} \rightarrow ^4I_{15/2}$ transition in $ZnTiO_3:Er^{3+}, Yb^{3+}$ phosphor.....	86
Figure 8.1: (a) X-ray Diffraction patterns and (b) peak intensities of the $ZnTiO_3: Er^{3+}, Yb^{3+}$ thin film deposited on the silicon (100) and heated at different temperatures.....	95
Figure 8.2: FE-SEM image of $ZnTiO_3: Er^{3+}, Yb^{3+}$ thin film deposited at 500 °C	96
Figure 8.3: A TOF-SIMS maps of the ions on the surface of the 0.8 mol% Er^{3+} and 0.7 mol% Yb^{3+} co-doped $ZnTiO_3$ thin film fabricated at temperature of 500 °C.	97
Figure 8.4: 3D overlay chemical composition of $ZnTiO_3: Er^{3+}, Yb^{3+}$ thin film fabricated at (a) 100 °C, (b) 200 °C, (c) 300 °C, (d) 400 °C, (e) 500 °C and (f) 600 °C.	98
Figure 8.5: TOF-SIMS depth profiles of the $ZnTiO_3: Er^{3+}, Yb^{3+}$ thin film deposited at different substrate temperatures as indicated.	99
Figure 8.6: The optical reflectance spectra of $ZnTiO_3: Er^{3+}, Yb^{3+}$ thin films grown in different substrate temperatures.	100
Figure 8.7: (a) PL spectra of $ZnTiO_3:Er^{3+}, Yb^{3+}$ thin film at different temperatures and (b) CIE chromaticity coordinates of $ZnTiO_3:Er^{3+}, Yb^{3+}$ thin film fabricated at 500 °C.....	101

Figure 8.8: (a) Up-conversion emission spectra measured at different laser power and (b) logarithmic dependence of intensity versus power of ZnTiO ₃ :Er ³⁺ ,Yb ³⁺ thin film fabricated at 500 °C.	102
Figure 8.9: Energy transfer mechanism showing the radiative transitions for up-conversion process in ZnTiO ₃ :Er ³⁺ ,Yb ³⁺ films under an excitation of 980 nm.	103
Figure 8.10: Photoluminescence decay curves of ZnTiO ₃ :Er ³⁺ ,Yb ³⁺ thin films at the emission centred at 547 nm.....	104
Figure 9.1: FE-SEM image of (a) ZnTiO ₃ and (b) ZnTiO ₃ :Eu ³⁺ ,Al ³⁺ ; (c) XRD patterns of undoped, Eu ³⁺ doped and Eu ³⁺ /Al ³⁺ co-doped ZnTiO ₃ annealed at 800 °C and (d) close inspection of the XRD patterns.....	110
Figure 9.2: PL emission spectra of (a) ZnTiO ₃ :xmol%Eu ³⁺ and (b) ZnTiO ₃ :2.0mol%Eu ³⁺ , xmol%Al ³⁺	112
Figure 9.3: The diffuse reflectance spectra of ZnTiO ₃ : Eu ³⁺ ,Al ³⁺	114
Figure 9.4: The Commission Internationale de l'Éclairage (CIE) diagram showing chromaticity points of ZnTiO ₃ :2mol%Eu ³⁺ and ZnTiO ₃ :2mol%Eu ³⁺ ,0.3mol%Al ³⁺	114
Figure 9.5: Decay curves of the ⁵ D ₀ → ⁷ F ₂ transition in (a) ZnTiO ₃ :Eu ³⁺ sample and (b) ZnTiO ₃ :Eu ³⁺ ,Al ³⁺ samples excited at 395 nm.....	116
Figure 9.6: Schematic energy level diagram of ZnTiO ₃ :Eu ³⁺ ,Al ³⁺ which is not drawn to scale.	118

List of Tables

Table 2.1: Electronic configuration of trivalent RE ³⁺ ions	17
Table 6.1: Representation of the concentration and calculated Commission Internationale de l'Eclairage (CIE) coordinates of ZnTiO ₃ : xmol%Er ³⁺	66
Table 7.1: Representation of the concentration and calculated Commission Internationale de l'Eclairage (CIE) coordinates of ZnTiO ₃ :0.8mol%Er ³⁺ , xmol% Yb ³⁺ phosphors.	82
Table 7.2: Photoluminescence decay lifetimes of ZnTiO ₃ :Er ³⁺ , Yb ³⁺ phosphor	87
Table 8.1: Luminescence lifetimes of ZnTiO ₃ :Er ³⁺ , Yb ³⁺ thin films fabricated at different temperatures	105
Table 9.1: Photoluminescence lifetimes of ZnTiO ₃ :2.0mol%Eu ³⁺ and ZnTiO ₃ :2.0mol%Eu ³⁺ , xmol%Al ³⁺ samples.	117

Chapter 1: Introduction

1.1. Renewable energy

Energy holds a central role for various industries, households needs, commercial trade and supporting and businesses [1, 2]. However, the energy consumption has increased in rural areas and urban areas as well as developing countries because the economic has grown drastically in the past decades [3-5]. As is the case with all energy sources, the use of renewable energy is recently used for electricity and heat productions because they are cost effective, clean and safe alternative modes of energy relative to others. Renewable energy is defined as the energy source that continuously replenishes by nature which comes directly and indirectly from the sun and from the other natural movements and mechanisms of the environments. The list of renewable energies includes solar thermal concentrators, biomass fuels, photovoltaic cells, hydrothermal energy, geothermal heat pumps and tidal energy [6, 7]. Since the research and technology is a hot focus in energy demand, the renewable energy sector will make up a great proportion of energy supplies for the future growth of energy sector [6].

Photovoltaic cells (PVs) are becoming the most abundant and used renewable energy sources globally. The basic science of photovoltaic devices was first discovered in 1839 by a French physicist, Edmond Becquerel. Various techniques have been employed to improve the quality of PVs from the first-generation systems until now. The first-generation systems of PVs are commercial systems based on crystalline silicon technology and the second-generation systems are based on the photovoltaic thin films cells. The third-generation systems are organic PVs which are still under the developmental phase. A photovoltaic cell generates the electricity by absorbing the incoming solar radiation and convert them into electron-hole pairs. In the modern times after the second generation of PVs, dye-sensitized solar cells (DSSCs), organic photovoltaics (OPVs) and perovskite solar cells (PSCs) appear as next-generation PVs owing to their tremendous advantage such low cost, solution-processability, flexibility, lightweight

and high-throughput manufacturing processes [8 - 10]. The promising efficient PVs have been associated with down and up-converting phosphors. With down-conversion process, single high energy photon is converted into two or more lower energy and the up-conversion is a process in which the two or more lower energy photons are converted into one high energy in the form of emission. Particularly, up and down-conversion involves up-converting near-infrared and down-converting ultraviolet photons to visible photons by pairing rare-earths ions in the host. Because rare earth ions have rich energy level structure, energy transfer between them is also possible by up and down-convert absorbed infrared and ultraviolet light to visible light by means of photons of different energy. A recent study shows that the most efficient up-conversion materials have been achieved by pairing a sensitizer Yb^{3+} and a suitable activator Er^{3+} doped a suitable host material due to their strong visible luminescence [11, 12]. On the other hand, the efficient down-conversion materials include Eu^{3+} coupled with a charge compensator [13] and rare earth ions (Dy^{3+} , Ce^{3+} , Tb^{3+} etc.) [11-15].

1.2. Problem statement

The fossil fuel has introduced a threat across the globe, because the resulting carbon emissions have depleted the ozone layer, leading to global warming. This has resulted into rising sea levels which cause flooding, hurricanes and heat waves that threaten crop production and proper respiration of the living organisms including human beings. These make it necessary to find alternative forms of energy supply sources. Additionally, the nuclear energy is also not a recommended solution because it also threatens the human health [16, 17]. Dye-sensitized solar cells (DSSCs) have proven to be a better candidate based on non-toxicity and the related cost of production, within the photovoltaic solar cell category [18]. This makes them interesting for the laboratory-based research, even though their power conversion efficiency still needs great attention. The factors hindering their power conversion efficiency include; insufficient utilization of the solar radiation because their absorption of the electromagnetic waves from the sun is limited to a small range, limited photo-carrier for trapping and recombination, and inefficient electron injection from its excited state into the semiconductor surface, just to mention a few [19, 20]. The present research intends to address problem by enlarging the range of the electromagnetic waves that can be absorbed from the solar radiation by down and up-converting the spectrum into the region that is absorbable by the solar cells.

1.3. Research aim and objectives

1.3.1. Aim of the study

The aim of this research is to enhance the efficiency of the Dye-sensitized solar cells, by incorporating a down converting and an up-converting luminescent material. The luminescent material will convert the electromagnetic waves that are not absorbable by a Dye-sensitized solar cell, into wave ranges that can be absorbable by the cells.

1.3.2. Objectives of the study

Finding ways to improve the efficiency and increase energy conversion efficiency of the DSSCs by:

- ✓ Synthesize and optimization of ZnTiO_3 nanoparticles using the conventional solid-state chemical reaction method and exposing the host to different annealing temperatures.
- ✓ Find suitable down and up-converting lanthanides for ZnTiO_3 nanoparticles.
- ✓ Optimize the down and up-conversion processes by varying the concentration of the dopant in the prepared host.
- ✓ Enhance the up-conversion by introducing the sensitizer (Yb^{3+}), which will supply more energy to the activators in order to increase emission output.
- ✓ Deposit the $\text{ZnTiO}_3: \text{Er}^{3+}, \text{Yb}^{3+}$ on the silicon substrate to prepare the thin films.
- ✓ Enhance the down-conversion by introducing the charge compensator (Al^{3+}), which will balance the and enhance the emission output of the activators.
- ✓ Investigate the efficiency changes that are introduced by the phosphors.

1.4. Organization of the thesis

1.4.1. Supervision

This research was supervised by Professor Mokhotjwa S. Dhlamini from the University of South Africa, Science Campus and co-supervised by Doctor Luyanda L. Noto, Professor Bakang M. Mothudi, both from the University of South Africa and Professor Odireleng M. Ntwaeaborwa, from Witwatersrand University, South Africa.

1.4.2. Collaborations

The University of the Free State with the photoluminescence measurements, TOF-SIMS measurements and the use of Pulsed laser Deposition (PLD) technique.

1.5. Thesis layout

This thesis is divided into the following ten chapters:

Chapter 1 provided a general introduction about renewable energy, solar cells, up and down-conversion phosphors, problem statements and the aims of the study. **Chapter 2** provides the theoretical background on the fundamentals of luminescence processes and energy transfer in rare earth activated phosphors mainly for up-conversion applications in photovoltaic cells. It also provides the information on the synthesis method for the preparation of the $\text{ZnTiO}_3:\text{Er}^{3+}, \text{Yb}^{3+}$ and $\text{ZnTiO}_3:\text{Eu}^{3+}, \text{Al}^{3+}$ phosphors. **Chapter 3** gives a brief description of characterization techniques that were used to characterize the prepared phosphors. **Chapter 4** discusses the structural and optical evaluation of NIR up-converting Er^{3+} doped $\text{ZnTiO}_3\text{-Zn}_2\text{TiO}_4$ composite phosphor. In **Chapter 5** the structural and optical evaluation of NIR up-converting $x\text{mol}\%\text{Er}^{3+}$ doped $\text{ZnTiO}_3\text{-Zn}_2\text{TiO}_4$ composite phosphor is discussed. **Chapter 6** presents the up-converting luminescence properties of $\text{ZnTiO}_3:\text{Eu}^{3+}$ phosphor synthesized by conventional solid-state reaction method. Up-conversion luminescence and energy transfer mechanism of $\text{ZnTiO}_3:\text{Er}^{3+}, \text{Yb}^{3+}$ phosphor is presented in **Chapter 7**. **Chapter 8** discusses the up-conversion luminescence of $\text{Er}^{3+}\text{-Yb}^{3+}$ co-doped ZnTiO_3 thin films. In **Chapter 9**, Luminescence properties of $\text{ZnTiO}_3: \text{Eu}^{3+}, \text{Al}^{3+}$ phosphor synthesized by conventional solid-state reaction method. Finally, **Chapter 10** gives the summary of the thesis and suggestion of the future work.

1.6. References

- [1] A. Shrestha, L.B. Rana, A. Singh, S. Phuyal, A. Ghimire, R. Giri, R. Kattel, K. Karki and S.K. Jha. *Energy Procedia* **160** (2017) 76 – 83.
- [2] E. Nehrenheim. *Encyclopedia of the Anthropocene* **1** (2018) 504 – 406.
- [3] M.F. Hossain, S. Hossain and M.J. Uddin. *Renew. Sust. Energ. Rev.* **70** (2017) 44 – 49.
- [4] T.A. Hamed and L. Bressler. *Renew. Energ.* **135** (2019) 378 – 389.
- [5] H. Saastamoinen and S. Paiho. *Energy Procedia* **149** (2018) 307–316.
- [6] A. Inayata and M. Raza. *A review. Renew. Sust. Energ. Rev.* **107** (2019) 360 –373.
- [7] A.M. Bagher, M.M.A. Vahid, B.M. Reza, M. Mohsen and G. Mahshi. *Bull. J. Adv. Sci. Res.* **01 (04)** (2015) 129 – 131.
- [8] L. Hernández-Callejo, S. Gallardo-Saavedra and V. Alonso-Gómez. *Solar Energy* **188** (2019) 426 – 440.
- [9] E. Tatsi, G. Griffini. *Sol. Energy Mater. Sol. Cells* **196** (2019) 43 – 56.
- [10] S. Shittu, G. Li, Y.G. Akhlaghi, X. Ma, X. Zhao and E. Ayodele. *Renew. Sust. Energ. Rev.* **109** (2019) 24 –54.
- [11] W.J. Ho, C.Y. Wei, J.J. Liu, W.C. Lin and C.H. Ho. *Vacuum* **166** (2019) 1– 5.
- [12] W. Cai, Z. Zhang, Y. Jin, Y. Lv, L. Wang, K. Chen and X. Zhou. *Solar Energy* **188** (2019) 441– 449
- [13] Y. Wu, M. Chen, K. Qiu, W. Zhang and Q. Tang. *Opt. Laser Technol.* **118** (2019) 20 – 27.
- [14] Y. Chen, G. Chen, X. Liu, J. Xu, T. Yang, C. Yuan and C. Zhou. *J. Non-Cryst. Solids* **484** (2018) 111–117.
- [15] N. Yao, J. Huang, K. Fu, S. Liu, E. Dong, Y. Wang, X. Xu, M. Zhu and B. Cao. *J. Power Sources* **267** (2014) 405 – 410.
- [16] R. Ciriminna, F. Meneguzzo, M. Pecoriano and M. Pagliaro. *Renew. Sust. Energ. Rev.* **63** (2016) 13 –18.

- [17] P. Wegertseder, P. Lund, J. Mikkola and R.G. Alvarado. *Solar Energy* **135** (2016) 325 – 336.
- [18] L. Song, Y. Guan, P. Du, Y. Yang, F. Ko and J. Xiong. *Sol. Energy Mater. Sol. Cells* **147** (2016) 134 –143.
- [19] M. Rani and S.K. Tripathi. *Renew. Sust. Energ. Rev.* **61** (2016) 97–107.
- [20] D. Wanga, H. Hana, H. Gaob, Z. Yanga, Y. Xingb, H. Caoa, W. Hea, H. Wanga, J. Guc and H. Hud. *Synth. Met.* **220** (2016) 41– 47.

Chapter 2: Theoretical Background

2.1. Introduction

Energy demand remains one of the world's greatest challenges and has been affected by economic growth, shortage of fossil fuels and few sustainable renewable energy resources and increase in crude oil prices. Extensive research and the use of nanotechnology in renewable energy resources are a major priority in energy demand reduction [1, 2]. Renewable energy sources are classified as solar cells, wind power, hydroelectric energy, geothermal power etc, [3, 4]. In general, the use of renewable energy system has become a noticeable factor in energy demand reduction because it is distributed over a wide geographical area, ensuring that developing countries have access to energy supply at reasonable cost for the future global energy needs. In the family of existing renewable energy sources, solar cells are most widely used as they utilize incident solar radiation to generate useful electrical energy, and the latter convert solar energy into heat energy without any “green-house” gas emission [4, 5].

2.2. Solar cells

Solar cells can either be photovoltaic cells or solar concentrators, where the earlier is a semiconductor device that utilizes incident solar energy to generate useful electrical energy. When sunlight strikes on any semiconductor solar cell, some of the light is absorbed by the semiconductor material and therefore generate an electron-hole pair. In this case, the electrical power is generated when the structures of the device separate the electrons (to the negative terminal) and holes (to the positive terminal) [6]. Among existing solar cells, dye-sensitized solar cells (DSSCs) are considered as potential candidates for next-generations concerning the technological advance in harvesting sunlight and transforming it into electrical energy due to their relatively low production cost, working in low-light conditions, large-scale feasibility, and higher efficiencies at higher temperatures [7-9].

2.3. Dye-sensitized solar cells

Dye-sensitizer also called photosensitizer is the best material employed for fabrication of the dye-sensitized solar cells. It is an important material because of its significant charge separation, device stability, light-harvesting and high influence on power conversion efficiency [10, 11]. These first dye-sensitized solar cells (DSSCs) were first fabricated in 1991 by Michael Grätzel and O'Regan. Although the literature revealed correspondingly that the highest efficiency for DSSCs is about 14% and it has been reported that it can reach a remarkable conversion efficiency of approximately 32% [12-14]. In general, a DSSC consists of a titanium (TiO_2) semiconductor coated transparent conducting oxide, glass substrate, electrolyte containing iodide/triiodide (I^-/I_3^-) redox couples, a dye sensitizer and a platinized counter electrode (Pt CE) as shown in Fig. 2.1. The anode of a DSSC is soaked with a dye solution which bond the TiO_2 semiconductor while the cathode consists of a glass plate with a thin Pt film which serves as a catalyst.

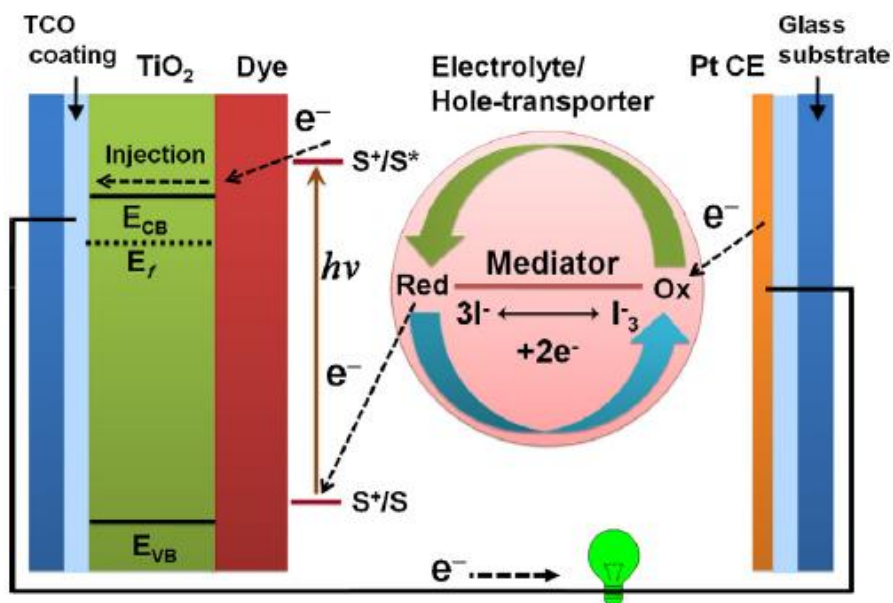


Figure 2.1: Schematic diagram of a DSSCs. S and S^* represents a ground and excited states of dye sensitizer molecule and S^+ represents a dye sensitizer hole (the oxidized dye molecules) [15].

In the operating principle of DSSCs, a dye is used to absorb photons which generate charge carriers and results in electron injection from the ground state to an excited state of the TiO_2 semiconductor. The conducting substrate absorbs the injected electrons and transports them to

the external circuit in order to reach the platinized counter electrode. Subsequently, the oxidized dye sensitizer is reduced back to the ground state by electron transfer through the electrochemical redox reaction, and it receives the electrons from the external circuit to complete the whole photoelectric chemical reaction cycle [16, 17, 18]. It was reported that the sun provides energy approximately 10 000 times more than the global demand (3×10^{24} J/year) [19]. But some of this energy from the sun is not absorbed due to smaller energy photons that are transparent to the semiconductors and excess of higher energy photons of semiconductor is lost to lattice thermalization. According to literature, this energy losses can add up to more than 50% of the utilizable solar energy for solar cells [20]. Introducing phosphors for up and down-conversion of the photon energy (abbreviated UC and DC) in DSSCs is a recent research focus into reducing the energy loss.

Up and down-conversions are one of the promising methods to overcome problems of transparency and thermalization. In general, up-conversion is the absorption of lower energy radiation by a phosphor, which transfers it to higher energy radiation, which may correspond to the visible band, ultraviolet band, etc. Down-conversion is the absorption of higher energy radiation, which is re-emitted as lower energy radiation. Most importantly, during the process of UC, two or more low-energy near-infrared photons are converted into a single high-energy output, whereas DC is capable of converting one high-energy ultraviolet photon into two or more low-energy output photons. These two photon radiation methods have the advantage of enhancing the efficiency of solar cells at low costs [21]. The use of luminescence converter layer to avoid transmittance and thermalization inside the solar cell should be applied on the rear surface of solar cell. In order to avoid the loss of usable luminescence, a suitable reflector is needed inside solar cells during up-conversion process and a bifacial solar cell is needed inside solar cells during the down-conversion process [22, 23].

2.4. Fundamentals of luminescence

Luminescence is a phenomenon in which a substance emits light when exposed to various radiations such as X-rays, ultraviolet-infrared radiation, electron bombardment, or another source of excitation. After the absorption of the radiation by phosphor, an electron is promoted from the ground state into an excited state, then the electron gives back the energy in the form of light by falling back to its ground state level. The luminescence process can be illustrated in Fig. 2.2. The figure shows two processes taking place when the electron returns to the ground

state, namely: radiative (R) process and non-radiative (NR) process. In this case, the luminescence process occurs from radiative process. Through the process of non-radiative process, phonons are converted into lattice vibrations that transport energy in the form of heat and there is no emission of light produced [24 - 27].

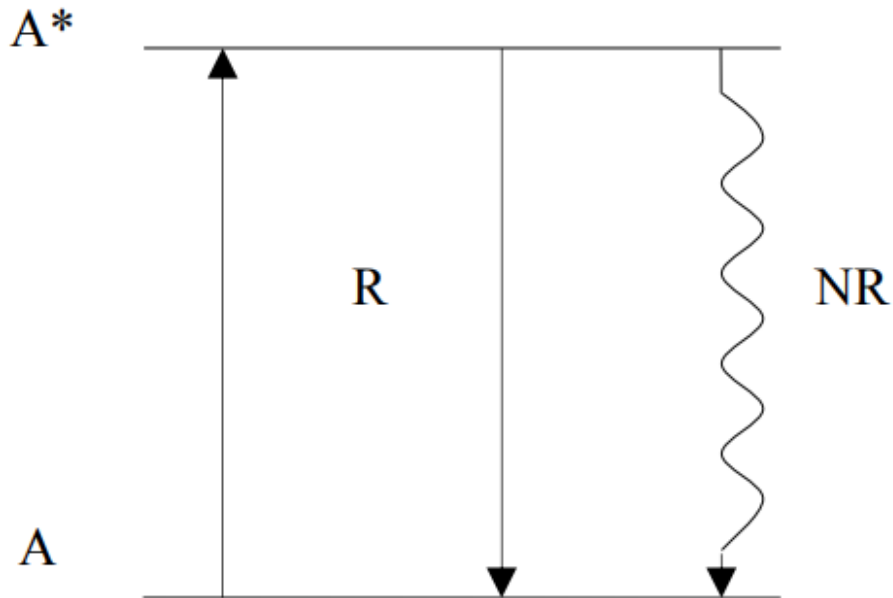


Figure 2.2: Jablonski schematic diagram showing the electronic states responsible for luminescence emission of ion A. The absorption of light is shown with a black arrow pointing upwards ($A \rightarrow A^*$) and the emission of light with the one pointing downwards ($A^* \rightarrow A$). The * indicate the excited state, R the radiative process and NR is the non-radiative process [24].

In general, the characteristics duration of the emission of light is classified as fluorescence with a lifetime of 10^{-8} s to 10^{-5} s, phosphorescence with a lifetime of 10^{-8} s up to 10 seconds, and thermoluminescence with a lifetime of minutes to 4.6×10^9 years. Fluorescence, which is independent of temperature is defined as the emission of light taking place from an excited singlet state while the phosphorescence, which is strong temperature dependence is the emission that occur from the triplet state [24]. The luminescence in the materials is classified as photoluminescence (PL), thermoluminescence (TL), electroluminescence (EL), chemiluminescence (CL) and radioluminescence (RL), cathodoluminescence (CL) respectively [24, 25]. Most of the substances or materials that gives light are called phosphors which consist of a host lattice and a luminescent centre often called an activator [25 - 27]. This research is focusing more on photoluminescence because it has a wide application in varying fields. Photoluminescence is defined as the re-emission of light from any form of matter after

the excitation source of electromagnetic radiation or photons. This phenomenon can be grouped into two categories, namely: intrinsic and extrinsic luminescence.

2.4.1. Intrinsic luminescence

Intrinsic luminescence is the direct luminescence from the pure crystal or material after the excitation source and can be classified as band-to-band luminescence, cross-luminescence and exciton luminescence. Band-to-band luminescence is the phenomenon by which light is produced by pure material at relatively high temperature through the recombination of an electron with the hole creating band-to-band transition. On the other hand, cross-luminescence is produced by the recombination of an electron in the valence band with the hole created in the outermost core band. Therefore, this phenomenon is observable in alkali, alkaline-earth halides and double halides, respectively. However, exciton exist when the excited electron and a hole interact with one another. During this process, the exciton moves in a crystal conveying some energy and the recombination of the electron and a hole gives luminescence. The exciton is thus divided into two classes which is Frenkel and Wannier exciton. Frenkel exciton occurs primarily in the case where the distance between the electron and hole wavefunction is smaller than the lattice constant and the Wannier exciton exist mainly in semiconductors when the electron in the conduction band and a hole in the valence band interact through Coulomb interaction [24].

2.4.2. Extrinsic luminescence

This type of luminescence occurs due to the incorporation of the foreign atoms or defects in the host materials. The foreign atoms can serve as an impurity and they are normally called activators. In some of the cases, an activator in the material shows weak luminescence or does not absorb the excitation sources. In this case, the host lattice can act as a sensitizer by absorbing the incident photons and transferring the excitation energy to the activator. In most of today's luminescence materials, the absorption of photons which results in the emission of light take place in rare earth doped oxide host lattice for various applications in lighting devices [24, 27].

2.5. ZnTiO₃ nanoparticles

The research on enhancing the efficiency of DSSCs is typically conducted using metal oxide-

based semiconductors such as ZnO, Nb₂O₅, TiO₂, SnO₂ and SrTiO₃ [28]. Among them, zinc oxide (ZnO) nanoparticles have received significant attention because of its potential applications in solar energy conversion, light-emitting materials and photon catalysis. This is due to its wide bandgap (3.37 eV) and large exciton binding energy (60MeV) [28, 29]. According to Nazeri et al [29], in order to improve the efficiency of the performance of TiO₂ in DSSCs, different approaches have been utilized such as coupling TiO₂ with another metal oxide such as ZnO, to form composites. These materials tend to be paired and used in solar cells because they have similarly positioned valence and conduction band, but they have different properties that are advantageous for different applications and examples are, ZnO have higher conductivity compared to TiO₂ while TiO₂ have higher chemical stability and reactivity, much higher dielectric constant and fewer defects states. ZnO can be easily nanostructured [30-32]. In addition, the combination of these metal oxides has been found to be a promising material for DSSCs cell because it provides better surface area, transport, surface morphology and photo-electrochemical properties (e.g. photo-catalysis and photo-induced super-hydrophilicity) [33, 34].

It was reported that there are three crystallophic phases (Zinc titanate) existing in ZnO-TiO₂ system such as Zn₂Ti₃O₈ and Zn₂TiO₄ both with a cubic spinel structures, and ZnTiO₃ with a hexagonal and cubic structures. Zinc titanate phases has been synthesized from ZnO and TiO₂ through solid-state reaction method, and the first phase to be formed is Zn₂Ti₃O₈ at low-temperature synthesis, then ZnTiO₃ appears at annealing temperatures $T < 900$ °C which decomposes into Zn₂TiO₄ at annealing temperatures $T > 900$ °C. The unique properties of ZnTiO₃ semiconductor lend themselves to a wide application which include paint pigments, microwave dielectric ceramics, catalytic sorbent for desulfurization of hot coal gases and gas sensors for the detection of Nitric Oxide, Carbon Monoxide [35, 36]. Moreover, it has been reported that ZnTiO₃ can be considered as a promising host luminescent material and it was first reported by Wang et al. in 2003 [37, 38]. Nevertheless, considering tremendous luminescent properties of zinc titanate, the use of up and down-conversion trivalent rare-earth ion (RE³⁺) gives the opportunity to tune the properties of metal oxide semiconductors in a controlled manner in order to enhance the performance of the solar cells [30, 31]. In addition to RE³⁺ co-doping, cations with small ionic radius can be introduced easily into lattice interstitially or substitutionally to tailor the local crystal symmetry. This can be achieved by tri-doping the host matrix with activator, sensitizer and cations [39].

In this study, ZnTiO₃ material and ZnTiO₃-Zn₂TiO₄ composite co-doped with up and down-conversion RE³⁺ ions were investigated. In addition, the energy transfer through up and down-conversion process was investigated.

2.6. Up-conversion mechanism

As mentioned above, UC radiation is the conversion of low energy radiations into high energy radiation. This mechanism can be achieved through multi-photon absorption process in either lanthanides, triplet-sensitized process or by transition metal-based materials incorporated in different types of hosts. The reason this UC process is needed is because there are different parameters involved in the UC mechanism such as photo-physical properties (lifetime, efficiency and colour), activators, host matrix, excitation, lanthanides concentration, excitation, size and sensitizers. Knowing that these parameters can play an important role in UC process, one might form a hypothesis that optimizing properties, such as the brightness and photon frequency range of the phosphor might enhance the efficiency of photovoltaic cells, when a UC phosphor is incorporated. However, it has been reported that UC based lanthanides materials can be divided into three main classes, namely; excited-state absorption (ESA), energy-transfer up-conversion (ETU), and lastly two-photon absorption (TPA) (sometimes called photon avalanche) [13, 39, 40]. Fig. 2.3 (a)-(d) depicts representative up-conversion mechanisms in rare-earth (RE³⁺) doped up-conversion materials. An excited-state absorption process involves a single emitting ion with energy levels absorbing two (2) or more energy photons whereby it is promoted to higher excited state.

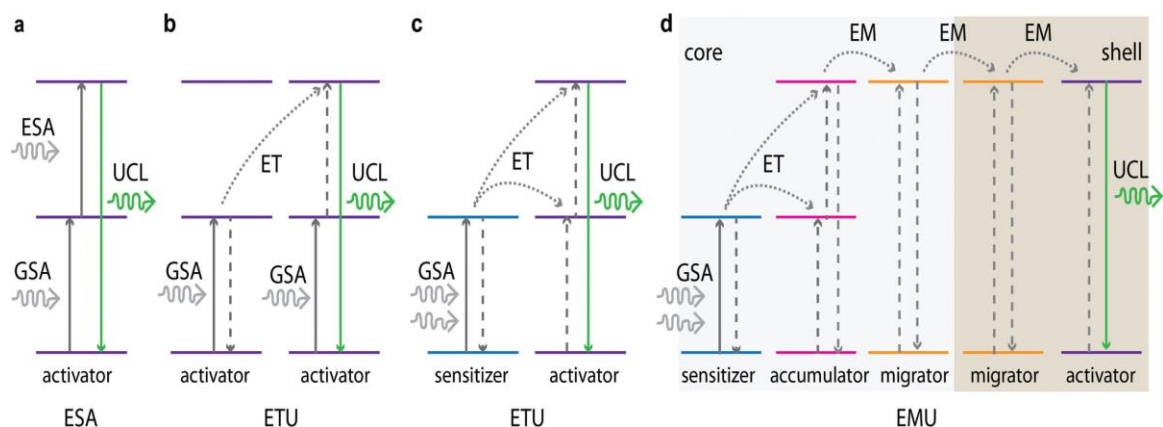


Figure 2.3: (a-d) Basic principle of up-conversion mechanisms or processes in Ln³⁺ doped up-conversion nanomaterials [41].

The main mechanisms for UCL involve activator (GSA/ESA), activator-activator (GSA/ETU), sensitizer-activator (GSA/ETU) and energy migration up-conversion (EMU). As shown in Fig. 2.3 (a) GSA/ESA is a simple three-level system whereby two energy photons are absorbed by ground-state absorption (GSA) and populate the excited metastable level (lower energy level of ESA). Subsequently, the photon energy in excited metastable level is promoted to higher energy level in ESA and relaxes to the ground state in the form of up-conversion luminescence. However, GSA/ETU is quite different from GSA/ESA since GSA/ETU mechanism involves two identical neighbouring ions (an activator-activator pair) as illustrated in Fig. 2.3 (b) and two different neighbouring ions (the sensitizer-activator pair), see Fig. 2.3 (c). In identical neighbouring ion mechanism, each activator ion absorbs photon energy of the same energy to higher energy level. During this process, one of the activator ions is promoted to higher excited state via non-radiative energy transfer and relaxes to the ground state in the form of up-conversion luminescence while the other one relaxes back to the ground state. In the case of sensitizer-activator mechanism, the sensitizer ions absorb two-photon energy by GSA and subsequently transfer it to activator which promotes photon energy to its intermediate state, followed by up-conversion luminescence. Lastly, the up-conversion of EMU mechanism (Fig. 2.3 (d)) involves four types of ions mechanism in Fig. 2.3, which result in the combination of GSA, ET, and EM steps [39, 40].

2.7. Down-conversion mechanism

The process of down-conversion including quantum cutting (QC) and down-shift (DS) modes involve the co-operative energy transfer (CET) and it is very efficient for paired rare-earth ions co-activated suitable host material. In this case, there is an absorption of photons with energy as twice or more times the band gap of a host materials. The DC mechanism is frequently used to modify the incident spectrum, which could provide a promising way for the improvement of solar cell efficiency [42, 43]. Fig. 2.4 illustrates the DC mechanisms in RE^{3+} (labelled I and II) ions doped host lattice for DC application. In the case of a single RE^{3+} ions as shown in Fig. 2.4 (a), the absorption of a single photon involves a two-photon visible emission and this process is called quantum cutting. As a result, the use of two or more RE^{3+} ions as shown in Fig. 2.4 (b)-(c) involves energy transfer during DC process. In this case, the excited photon from “ RE^{3+} I” relax from the highest energy level into the lower energy levels and transfer energy into “ RE^{3+} II” through path 2 which one or both ions subsequently emit visible photons.

On the other hand, the energy transfer through path 1 shows that some of the excitation energy is transferred from one RE^{3+} to another one by a process called cross relaxation whereby a single photon is emitted in the visible region of electromagnetic spectrum [45, 46].

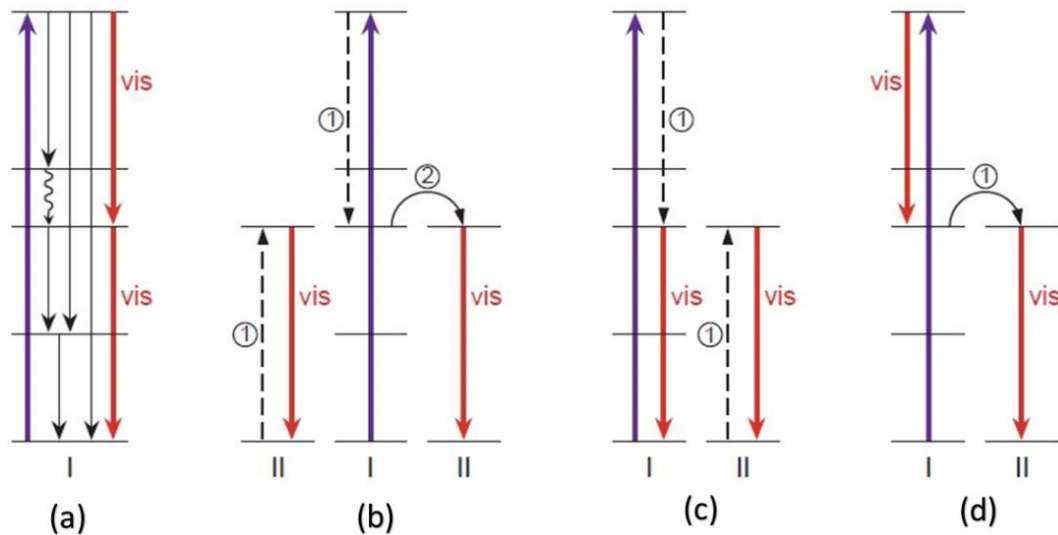


Figure 2.4: (a-d) Schematic diagram for rare-earth ions down-conversion mechanisms [44].

2.8. Rare earth ions

The trivalent rare-earth (RE^{3+}) ions, known as lighting elements, can serve as an impurity in certain host matrix or nanocrystals to achieve a wealthy luminescent characteristic by acting as wavelength converting system. This process can be either down-conversion (DC) or up-conversion (UC) [46]. RE^{3+} ions refer to a series of 15 consecutive elements (atomic number $Z = 57$ to 71) of the third transition series at the bottom of periodic table ranging from lanthanum to lutetium. The RE^{3+} elements were discovered in 1787 as a heavy piece of black rock called Yttria. The first element observed from the black rock was Yttrium, with atomic number 36, and further analysis of the rock revealed a whole range of RE^{3+} elements (atomic number $Z = 57$ to 71) [47]. Fig. 2.5 present the Dieke diagram of the observed rare-earth ions with their energy levels structure of the $4f^n$ configurations as a function of energy. The general electronic configuration of trivalent RE^{3+} ions is given as follows: $[\text{Xe}]4f^n 5d^{0-1} 6s^2$. The $4f^n$ electrons shell structure of all RE^{3+} ions are filled gradually from $n = 0$ to 14 electrons, which gives rise to a rich quantity of excited electronic levels. Table 2.1 present the electronic configuration of trivalent rare-earth ions giving more details about the $4f^n$ configuration.

The $4f^n$ electrons shell structure is also efficiently shielded by the filled $5s^2$ and $5p^6$ electrons shells so that the $4f$ electrons are less influenced by the environment of the lanthanide ions even in solid materials. A characteristic feature of RE^{3+} ions through intra- $4f$ or $4f-5d$ transitions is their sharp emission in ultraviolet, visible or near infrared spectral regions which results in high purity of the colour of emissions [48, 49].

Table 2.1: Electronic configuration of trivalent RE^{3+} ions [50].

Element	Symbol	Z	Electronic configuration
Lanthanum	La	57	$[Xe]4f^05d^16s^2$
Cerium	Ce	58	$[Xe]4f^26s^2$
Praseodymium	Pr	59	$[Xe]4f^36s^2$
Neodymium	Nd	60	$[Xe]4f^46s^2$
Promethium	Pm	61	$[Xe]4f^56s^2$
Samarium	Sm	62	$[Xe]4f^66s^2$
Europium	Eu	63	$[Xe]4f^76s^2$
Gadolinium	Gd	64	$[Xe]4f^75d^16s^2$
Terbium	Tb	65	$[Xe]4f^96s^2$
Dysprosium	Dy	66	$[Xe]4f^{10}6s^2$
Holmium	Ho	67	$[Xe]4f^{11}6s^2$
Erbium	Er	68	$[Xe]4f^{12}6s^2$
Thulium	Tm	69	$[Xe]4f^{13}6s^2$
Ytterbium	Yb	70	$[Xe]4f^{14}6s^2$
Lutetium	Lu	71	$[Xe]4f^{14}5d^16s^2$

The well-known candidates of up-converting trivalent RE^{3+} ions from the infrared band to the visible band include Er^{3+} , Tm^{3+} , Ho^{3+} , Pr^{3+} , Nd^{3+} and Yb^{3+} . RE^{3+} ions such as Er^{3+} , Tm^{3+} , Ho^{3+} , Pr^{3+} and Nd^{3+} are mostly used as activators which generate up-conversion luminescence for 980 nm radiations. An interesting ion is Yb^{3+} , because it has proven to be an effective sensitizer in generating efficient up-conversion luminescence when co-doped with UC activators [39, 40, 46, 48]. On the other hand, experimental work based on DC in RE^{3+} ions doped materials suggested the Yb^{3+} as an interesting emitter (activator) when co-doped with Nd^{3+} , Pr^{3+} , Tb^{3+} , Tm^{3+} and Er^{3+} sensitizers. In this case, a wealthy DC luminescence is achieved via cooperative energy transfer from sensitizers to two Yb^{3+} ions [45].

2.9. Energy transfer mechanism

The theory of energy transfer (ET) mechanism was predicted by Foster and Dexter. This mechanism is a process that occurs normally in a system in which the excited state transitions of the sensitizer (donor) partially overlaps the ground state transition absorption of the activator (acceptor) ions. In phosphor, the ET mechanism can occur either between various host lattices and the single activator ion or between different RE^{3+} in the host lattice [51, 52]. In general, an energy transfer between the sensitizer ion (S) and an activator ion (A) can be written as a chemical reaction



where the asterisk indicates the excited state transition. The Jablonki diagram presented in Fig. 2.6 illustrates the energy transfer mechanism involved between the donor and the acceptor.

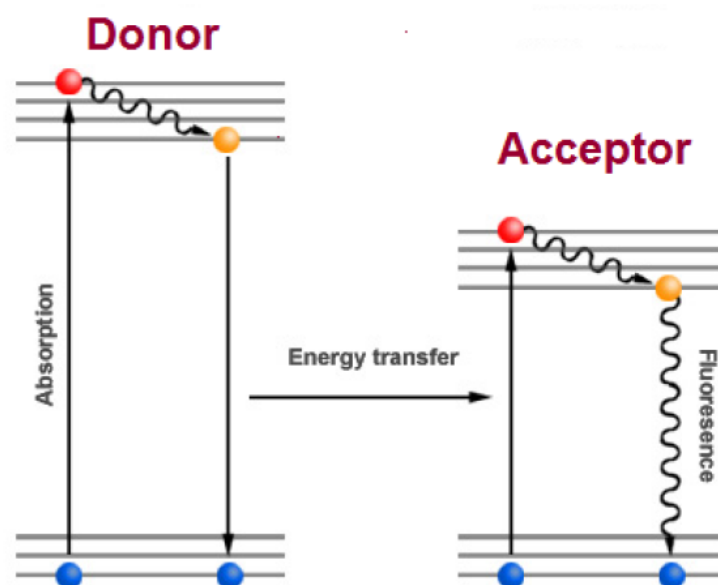


Figure 2.6: Schematic diagram illustrating the ET mechanism [53].

The mechanism of energy transfer requires the physical interaction between the sensitizer and the activator. However, during the physical interaction, this energy transfer can be able to find its origin in electrostatic or exchange interaction. Therefore, spectral overlap between absorption spectrum of the activator and emission spectrum of the sensitizer have to be observed, respectively, targeting energy conversion [54].

The dominant mechanism of the energy transfer is usually dipole-dipole interaction whereby the ions get spatially closer to one another with the increase in dopant concentration and there are some few criteria that lead to action of energy transfer in materials. This kind of process must be proportional to R^{-6} where R is the distance between the two centres. Additionally, the rate at which energy is transferred must also be proportional to the spectral overlap between emission spectrum of sensitizer and the absorption spectrum of the activator. During the process of energy transfer, the transfer rate is faster from the broad band sensitizer to broad band activator compared to transfer rate from broad band sensitizer to a narrow line acceptor. This whole process is due to anticipated larger spectral overlap in band to band process. In addition, energy transfer is believed to take place when the transition between the sensitizer and the activator are parallel to each other (i.e. ground state and excited state of sensitizer and activator are in resonance condition or equal) [55, 56]. Fig. 2.7 shows the spectral overlap that must be satisfied in order for the process of energy transfer to take place. The spectral overlap is shown by brown coloured region, restively.

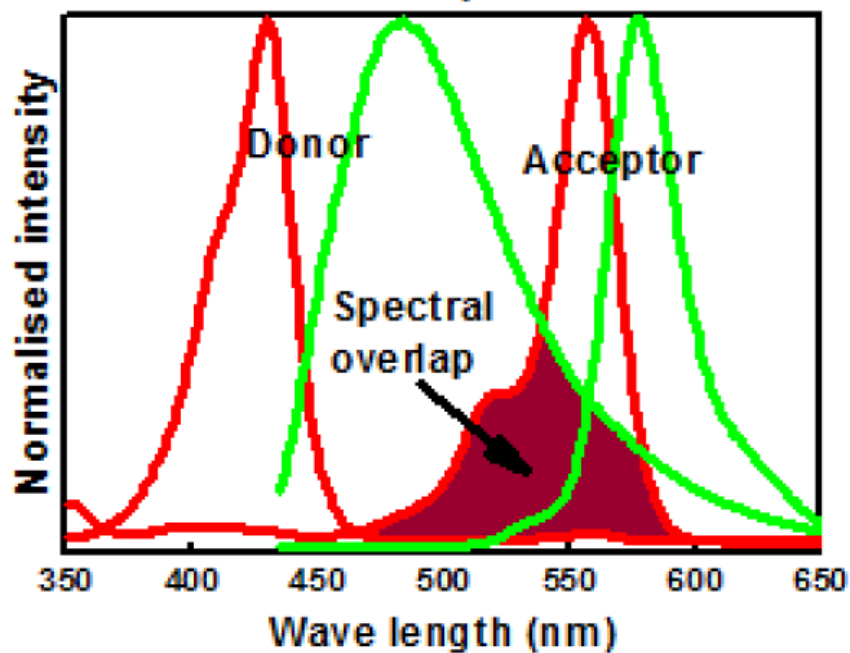


Figure 2.7: Schematic diagram of the spectral overlap of a donor emission and acceptor absorption [55].

Energy transfer mechanism in sensitizer-activator pair can occur by different processes such as radiative or non-radiative energy transfer [51, 57]. Upon absorption of the photon energy by a sensitizer, the transferring of the excitation energy from the excited electronic state of the

sensitizer to a nearby intermediate or ground states of the activator centres is taking place through radiative or non-radiative energy transfer mechanism. This process can also take place through resonant or non-resonant energy transfer because non-radiative energy transfer can be resonant. In addition, non-resonant energy transfer in sensitizer-activator system require a long-range dipole-dipole interaction and is possible through a phonon-assisted mechanism, accretive or cooperative mechanism. On the other hand, the radiative resonant energy transfer process involves the emission and the reabsorption of the photon energies [57, 58]. Fig. 2.8 shows the emission of photons from ion pairs (*S* and *A*) through various ET mechanisms.

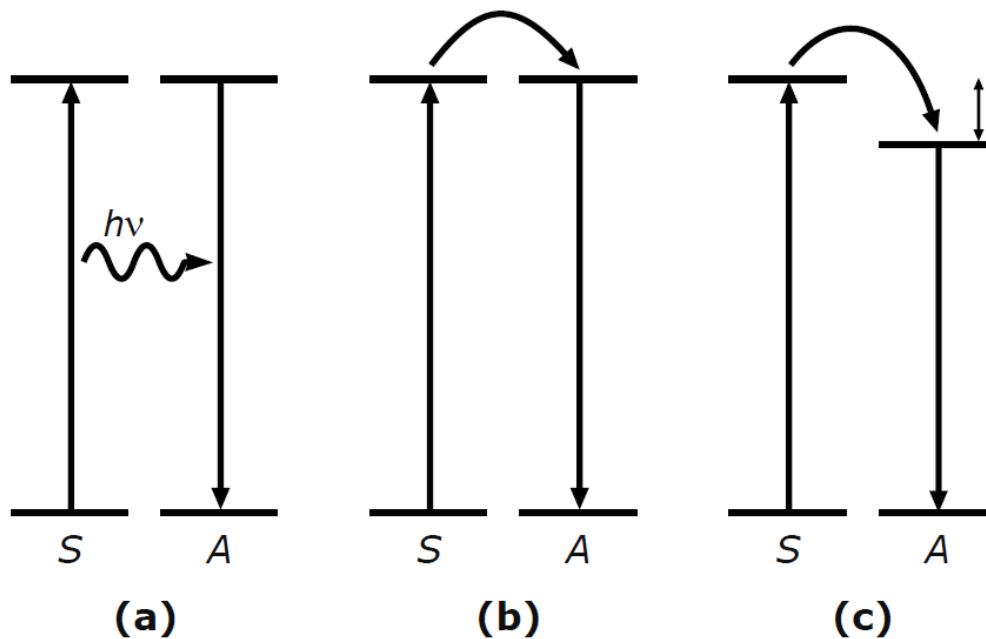


Figure 2.8: Schematic illustration of the energy transfer mechanisms, namely: (a) radiative energy transfer, (b) non-radiative energy transfer, and (c) phonon-assisted non-radiative energy transfer [58].

2.10. Synthesis and film fabrication

In this section, a brief description of the method used to synthesize nanomaterials is presented. Since the solids do not react with each other, the easiest way to make many solid materials is direct reaction of their components at high temperatures. This process can be achieved through solid state reaction. Solid state reaction, also known as mechanical milling, is a common top-down approach to fabricate nanoparticles at very high temperatures. The solid-state reaction has the ability for particle size reduction, improving the surface morphology of the crystal,

mixing or blending hard metals, oxide powders, composites, ceramics, intermetallic. The major advantage of solid-state reaction method is the final products in solid form with small crystallites or high surface area on the final sintering temperatures. In addition, this method is economically friendly and unwanted waste or non-toxic products are not produced when the chemical reaction is complete. This kind of synthesis method involves the following steps: Firstly, metal oxides are normally used in this method where the stoichiometric amounts of appropriate high purity materials or fine grain powders are thoroughly mixed together using ball miller or mortar and pestle at room temperature. Secondly, the resulting solid powder mixture is exposed to high temperature and normally using muffle furnace [59].

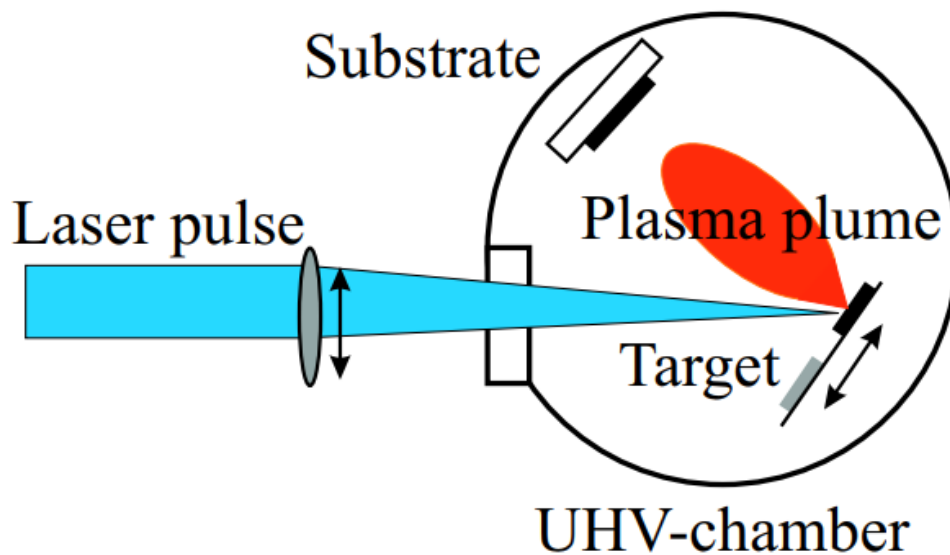


Figure 2.9: Experimental set-up of the PLD system [60].

In addition, pulsed laser deposition (PLD) is the most commonly used method to synthesize metal oxide thin films with accurate stoichiometry and high crystallinity. The basic set-up (Fig. 2.9) of the PLD consist of the laser pulse which is located outside the ultrahigh vacuum (UHV) chamber, a target holder and the substrate holder. The synthesis process in PLD system is divided into four stages. In the first stage, a high-power pulsed laser beam is focused by set of optical components inside the chamber and interact with the surface of the target material. In this case, the target material to be deposited is ablated out, in the form of plasma plume from the target. However, the interaction mechanisms involve rapid physical phenomena which include thermal and electronic excitation, collisional, hydrodynamics and exfoliation. The high-energy plasma plume is then impinged onto the surface substrate that is parallel to the

surface of the target and grow a film [60, 61]. There are several advantages of the PLD system such as the fast response, congruent evaporation, energetic evaporates and flexibility of the ablation of the pulse laser beam. In addition, the quality of the film growth during the deposition can be influenced by the preparations conditions which include substrate temperature, target-to-substrate distance, pressure and background gas composition [61].

References

- [1] M. Shahbaz, G. Gozgor and S. Hammoudeh. *Energ. Econ.* **78** (2019) 335 – 349.
- [2] T.A. Napp, S. Few, A. Sood, D. Bernie, A. Hawkes and A. Gambhir. *Appl. Energ.* **238** (2019) 351 – 367.
- [3] K. Mavroyeoryos, I. Engonopoulos, H. Tyrallis, P. Dimitriadisa and D. Koutsoyiannis. *Energ. Proced.* **125** (2017) 435 – 442.
- [4] N.K. M. A. Alrikabi. *J. Clean. Energ. Technol.* **2(1)** (2014) 61 – 64.
- [5] T. Markvart and L. Castaner. *Mater. Manuf. Oper.* (2013) 3 – 25.
- [6]. R. Ciriminna, F. Meneguzzo, M. Pecoraino and M. Pagliaro. *Renew. Sust. Energ. Rev.* **63** (2016) 13 – 18.
- [7] G.Y. Chen, M.W. Lee, and G.J. Wang. *Int. J. Photoenergy* **2010** (2010) 1– 7.
- [8]. P. Wegertseder, P. Lund, J. Mikkola and R.G. Alvarado. *Sol. Energy* **135** (2016) 325 – 336.
- [9] S. Rajkumara, M. Nirmal Kumar, K. Suguna, S. Muthulakshmi, R. Ashok Kumar. *Optik* **178** (2019) 224 – 230.
- [10] S. Yuna, J.N. Freitas, A.F. Nogueira, Y. Wang, S. Ahmade, Z.S. Wang. *Prog. Polym. Sci.* **59** (2016) 1– 40.
- [11] M. Chen and L.L. Shao. *Chem. Eng. J.* **304** (2016) 629 – 645.
- [12] G. Richhariya, A. Kumara, P. Tekasakul, and B. Gupta. *Renew. Sust. Energ. Rev.* **69** (2017) 705 – 718.
- [13] Tanvi, A. Mahajan, R.K. Bedi, S. Kumar, V. Saxena and D.K. Aswal. *Chem. Phys. Lett.* **658** (2016) 276 – 281.
- [14] H. Zheng, S.K. Shah, M. Abbas, I. Ly, T. Rivera, R.M. Almeida, L. Hirsch, T. Toupance, and S. Ravaine. *Photonics Nanostruct.* **21** (2016) 13 – 18.
- [15] J.S. Luo, Z.Q. Wan and C.Y. Jia. *Chem. Lett.* **37(8)** (2016) 1304 – 1318.

- [16] S. Yuna, J.N. Freitas, A.F. Nogueira, Y. Wang, S. Ahmade, Z.S. Wang. *Prog. Polym. Sci.* **59** (2016) 1– 40.
- [17] M. Chen and L.L. Shao. *Chem. Eng. J.* **304** (2016) 629 – 645.
- [18] D. Wanga, H. Hana, H. Gaob, Z. Yanga, Y. Xingb, H. Caoa, W. Hea, H. Wanga, J. Guc and H. Hud. *Synth. Met.* **220** (2016) 41– 47.
- [19] T. Markvarta and L. Castanerb. Principles of Solar Cell Operation (**2013**) *Materials, Manufacture and Operation*, 3rd Edition, 3 – 25.
- [20] Z.R. Abrams, Avi Niv and X. Zhang. *J. Appl. Phys.* **109** (2011) 1149051 – 1149059.
- [21] Y. Xu, J. Xiang, H. Zhao, H. Liang, J. Huang, Y. Li, J. Pan, H. Zhou, X. Zhang, J.H. Wang, Z. Liu and J. Wang. *Biomate.* **100** (2016) 91–100.
- [22] B.M. van der Ende, L. Aartsa and A. Meijerink. *PCCP* **11** (2009) 11081 – 11095.
- [23] T. Trupke, M. A. Green and P. Würfel. *J. Appl. Phys.* **92** (3) (2002) 1668 – 1674.
- [24] K.V.R. Murthy and H.S. Virk. *Defect and Diffus. Forum* **347** (2014) 1 – 34.
- [25] R. Chena and D.J. Lockwood. *J. Electrochem. Soc.* **149** (9) (2002) S69 – S78.
- [26] A. Kitai. (2008) *Luminescent Materials and Applications*. Chapman and Hall, London: John Wiley & Sons, Ltd.
- [27] B. R. Verma and R.N. Baghel. *Int. J. Mater. Sci.* (**12**)(3) (2017) 483 – 489.
- [28] M.Z.H. Khan, M.R. Al-Mamun, P.K. Halder, and M.A. Aziz. *Renew. Sust. Energ. Rev.* **71** (2017) 602 – 617.
- [29] G. Rani and P.D. Sahare. *J. Mater. Sci. Technolo.* **29** (2013) 1035 – 1039.
- [30] L. Wang, X. Fu, Y. Han, E. Chang, H. Wu, H. Wu, H. Wang, K. Li and X. Qi. *J. Nanomater.* **2013** (2013) – 6.
- [31] R.L.Z. Hoyer, K.P. Musselman and J.L. MacManus-Driscoll. *Appl. Materials* **1** (2013) 060701 (1 – 10).
- [32]. G. Khurana, S. Sahoo, S.K. Barik and R.S. Katiyar. *J. Alloys Compd.* **578** (2013) 257 – 260.

- [33] K. Prabakaran, S. Mohantyn and S.K. Nayak. *Ceram. Int.* **4** (2015) 11824 – 11835.
- [34] Y. Yanga , J. Zhao, C. Cui, Y. Zhanga , H. Hub, L. Xu , J. Pan, C. Li and W. Tang. *Electrochim. Acta* **196** (2016) 348 – 356.
- [35] S. Perween and A. Ranjan. *Sol. Energy Mater Sol. Cells* **163** (2017) 148 – 156.
- [36] Y.J. Acosta-Silva, R. Castanedo-Perez, G. Torres-Delgado, A. Mendez-Lopez and O. Zelaya-Angel. *Superlattices Microstruct.* **100** (2016) 148 – 157.
- [37] S.F. Wang, M.K. Lu, F. Gu, C.F. Song, D. Xu, D.R. Yuan, G.J. Zhou, Y.X. Qi. *Inorg. Chem. Commun.* **6(2)** (2003) 185 – 188.
- [38] S.F. Wang F. Gu, M.K. Lu, C.F. Song, D. Xu, D.R. Yuan, S.W. Liu. *Chem. Phys. Lett.* **373** (2003) 223 – 227.
- [39] P. Ramasamy, P. Manivasakan and J. Kim. *Chem. Sci.* **4** (2014) 34873 – 34895.
- [40] A. Nadort, J. Zhao and E.M. Goldys. *Nanoscale* **8** (2016) 13083 – 13524.
- [41] E.M. Chan. *Chem. Sci.* **44** (2015) 1653 – 1679.
- [42] M. Hanioka, S. Arimoto and H. Samata. *Optik* **154** (2018) 226 – 233.
- [43] Y. Zhydachevskyy, V. Tsiumra, M. Baran, L. Lipinska, P. Sybilski and A. Suchocki. *J. Lumin.* **196** (2018) 169 –173.
- [44] M.B. de la Mora, O. Amelines-Sarria, B.M. Monroy, C.D. Hernandez-Perez, J.E. Lugo. *Sol. Energ. Mater. Sol. Cells* **165** (2017) 59 – 71.
- [45] M.J.Y. Tayebjee and T.W. Schmidt. *Comprehensive Renewable Energy* **1** (2012) 549 – 560.
- [46] M.V. DaCosta, S. Doughan, Y. Han and U.J. Krull. *Anal. Chim. Acta* **832** (2014) 1 – 3.
- [47] Y. Dwivedi and S. C. Zilio. *J. Nanosci. Nanotechnol.* **14** (2014) 1– 20.
- [48] X. Chen, Y. Liu and D. Tu. (2014). *Lanthanide-Doped Luminescent Nanomaterials*. New York: Springer Heidelberg New York Dordrecht London.

- [49] J. Chen and J.X. Zhao. *Sensors* **12** (2012) 2414 – 2435.
- [50] Electronic configuration, [online]. Available from <http://www.studypage.in/images/chem/inorganic/electronic-config-lanthanides.png> [accessed 31 January 2019].
- [51] B.M.M. Faustino, P.J.S. Foot, and R.A. Kresinski. *J. Lumin.* **206** (2019) 205 – 210.
- [52] J. Ganem and S.R. Bowman. *Nanoscale Res. Lett.* **8** (2013) 455 (1– 11).
- [53] S.A. Hussain. *An Introduction to Fluorescence Resonance Energy Transfer (FRET)*. Cornell University (2009), eprint arXiv:0908.1815.
- [54] C.R. Ronda. *Luminescence: From Theory to Applications (2008)*, WILEY-VCH Verlag GmbH & Co. KGaA, Weinheim, ISBN: 978-3-527-31402-7.
- [55] L. Agazzi. *Spectroscopic Excitation and Quenching Processes in Rare-Earth-Ion-Doped Al₂O₃ and their Impact on Amplifier and Laser Performance*. The Netherlands (2012), Enschede.
- [56] P.P. Mokoena, H.C. Swart and O.M. Ntwaeaborwa. *Narrowband Ultraviolet B emission from gadolinium and praseodymium co-activated calcium phosphate phosphors for phototherapy lamps*. [Master's Thesis], University of the Free State, South Africa.
- [57] A. Nadort, J. Zhao and E.M. Goldys. *Nanoscale* **8** (2016) 13099 – 13130.
- [58] L. Aarts and A. Meijerink. *Downconversion for solar cells with lanthanides ion couples*. Universiteit Utrecht, Netherlands (2009) 1-18.
- [59] S.S. Su and I. Chang. *Review of Production Routes of Nanomaterials*. Springer International Publishing AG (2018). doi 10.1007/978-3-319-56979-6_2.
- [60] H.U. Krebs et al., Pulsed Laser Deposition (PLD) - A Versatile Thin Film Technique. *Advances in Solid State Physics* **43** (2003) 101 – 107.
- [61] T.K. Subramaniam. Pulsed laser deposition (PLD), (2015) Sri Sairam Engineering College.

Chapter 3: Experimental Techniques

3.1. Introduction

As mentioned in the previous chapter, the samples were prepared by conventional solid-state reaction. This chapter presents an overview and brief description of different research techniques used in this study to characterize the prepared samples. The techniques employed to probe structural and optical dynamics to achieve the goal of this research include x-ray diffractometer (XRD), scanning electron microscopy (SEM), photoluminescence (PL) spectroscopy, UV-Vis-NIR absorption spectroscopy, time of flight secondary ion mass spectroscopy (TOF-SIMS) and x-ray photo-electron Spectroscopy.

3.2. X-ray Diffractometer

X-ray diffractometer is an analytical and non-destructive tool used for the analysis of different kinds of matter such as powders, fluids and crystals [1]. XRD technique takes less time to extract wealth information on preferred crystal orientations, phases of materials and structural parameters, such as crystallinity, crystal defects, strain and average grain sizes of the materials. All this information is probed by constructive interference of a monochromatic beam of X-rays that are generated by cathode ray tube, and scatter at specific angle from each set of lattice planes in a target or compound that is mounted on the sample holder [2]. This is summarized in the diagram shown in Fig. 3.1. The interaction of rays respectively, takes place when the geometry satisfies the famous Bragg-Equation: $n\lambda = 2d\sin\theta$ where n is an integer that indicates the order of the reflection, λ is the wavelength of the incident light rays, d is the distance between lattice planes and θ is the angle of reflection [2, 3]. Fig. 3.2 depict the schematic diagram of the Rigaku SmartLab diffractometer system equipped with a high power 9kW rotating Cu anode generator. The X-ray diffractometers are equipped with an X-ray tube, a sample holder and a scintillation detector. In addition to these components, the SmartLab XRD employs the rotating anode X-ray generator (rotation via ω -angle), and the standard sample stage is manipulated through three circles: ϕ (in-plane rotation) and χ (swing axis) and the

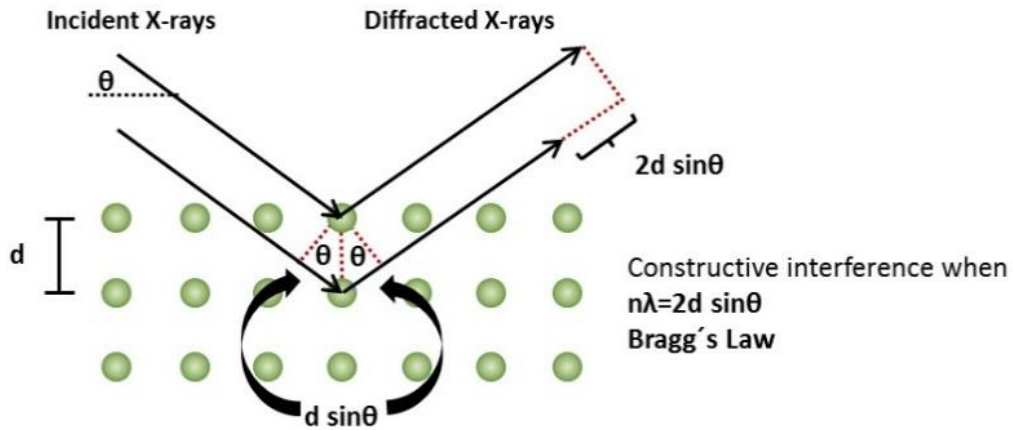


Figure 3. 1: Schematic diagram of Bragg reflection from a set of parallel planes [3].

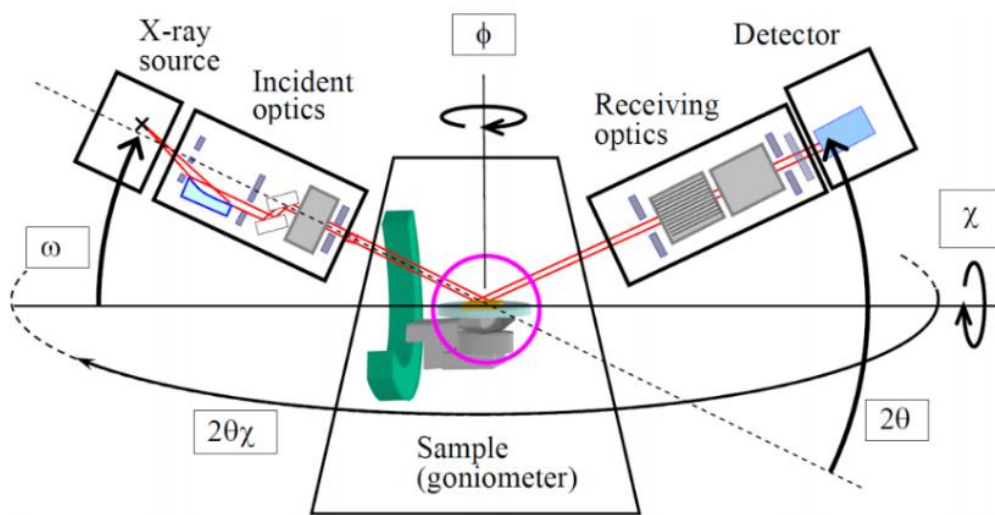


Figure 3.2: The configuration of X-ray diffraction system: Rigaku SmartLab 9 kW XRD [4].

detector moves with two circles (2θ and $2\theta \chi$) for in-plane measurements. As a result, the divergent X-rays are produced inside X-ray tube from X-ray source (Fig. 3.2). The X-ray tube contains a copper block and a metal attached to it (forms an anode) and a tungsten filament (which forms a cathode). The X-ray tube heat up the tungsten filament to generate electron and the applied voltage between the tungsten cathode and anode accelerate the produced electron towards the target materials. There are specific characteristics wavelengths for each component such as copper (Cu), iron (Fe), molybdenum (Mo), and chromium (Cr). Copper (Cu) is the most commonly used target material for single crystal and powder diffraction, with K_{β} and K_{α} Cu X-rays with 1.39 and 1.5406 Å wavelengths. However, Nickel filament is used to filter K_{β} radiation because it absorbs wavelength below 1.5 Å. Therefore, the K_{α} Cu X-rays with 1.54Å

wavelengths are the one used for the target characterization. The interaction of the electrons with target produce extreme reflected X-rays, and the rotating detector produce an electrical signal when exposed to reflected rays whereby the characteristic X-ray spectra is recorded [3, 4]. The X-ray diffractometer system which was used in this study is Rigaku Smartlab that was equipped with a monochromatic $\text{CuK}\alpha$ ($\lambda = 0.15405 \text{ nm}$) irradiation source that was operated at 200 mA current in a wide range of Bragg angle 2θ .

3.3. Field Emission Scanning Electron Microscopy

A field emission scanning electron microscope (abbreviated FE-SEM) is an analytical tool that works with a beam of electrons to observe topographic details by raster scanning over surface, entire or fractioned nanoscale objects. Information provided by this technique is based on the high-energy beam of electrons that are generated by a tungsten (W) or Lanthanum hexaboride (LaB_6) filament within the electron source and the specimen mounted on the sample holder. However, the high voltage is applied between the filament, which forms the cathode, and the anode plate (it can be primary or secondary anode) lead to an electrostatic field through from which the generated electrons are accelerated. These accelerated electrons are focused into a small beam and passes through condenser, specimen and objective lenses (Fig. 3.3), which emit secondary electrons from the surface of the specimen [5, 6].

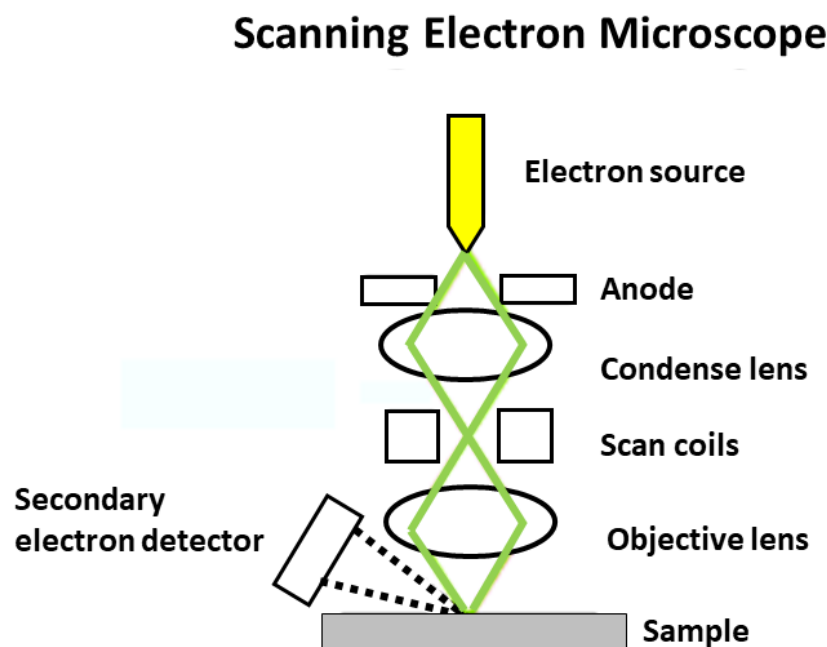


Figure 3. 3: Schematic diagram presenting FE-SEM operation mechanism [7].

There are several other signals that are generated during the interaction of the electrons and the specimen including emission of characteristic x-rays, cathodoluminescence and Auger electrons. Fig. 3.4 shows different signals that are detected. The emitted secondary electrons are recorded, converted into electrical signal and converted into morphological or compositional image. The field emission scanning electron microscope is coupled with energy x-ray dispersive spectroscopy which is used for elemental composition. EDS techniques use emitted X-rays from the interaction of primary electrons and the specimen and give the information about the characteristic of the elements from which it was emitted [5, 6]. The particle surface morphology and elemental composition in this research were studied by Jeol JSM-7800 field emission scanning electron microscope (FE-SEM) coupled with Oxford Aztec 350 X-Max80 Energy x-ray Dispersive Spectroscopy (EDS).

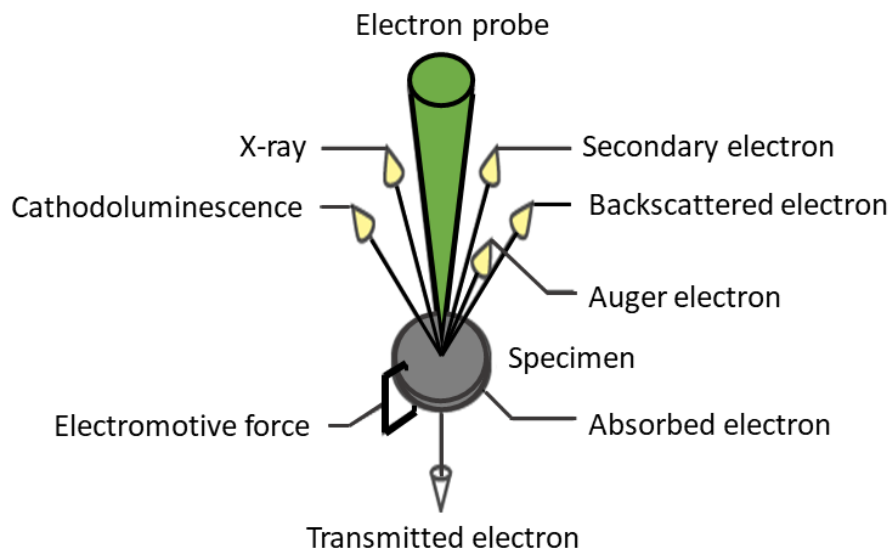


Figure 3.4: The illustration of several signals generated by the interaction of the electrons with specimen [8].

3.4. UV-Vis-NIR absorption Spectroscopy

Optical spectroscopy involves the study of the interaction of the electromagnetic radiation of various wavelengths with the unknown substances, solutions or solid materials. When the electromagnetic radiation in a certain wavelength illuminate solutions or solid materials, the light waves can be reflected, absorbed or transmitted. The reflectance, absorbance or transmittance characteristics of materials is measured with optical spectroscopy. One of the most useful optical spectroscopies for light absorption is UV-Vis absorption spectroscopy [9].

In this study, the reflectance studies of the samples were evaluated with Perkin Elmer Lambda 1050 UV-Vis-NIR absorption spectrometer. This instrument consists of a lamp compartment, double holographic grating monochromator, dual sampling compartment and three detector module which covers a spectral range of 175 – 3300 nm (Fig. 3.5).

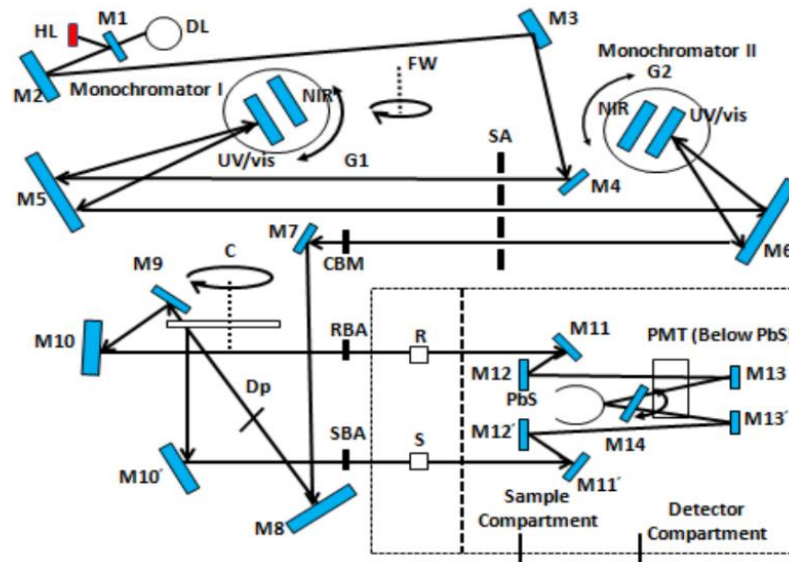


Figure 3. 5: Schematic diagram of the optical layout of UV-Vis-NIR spectrophotometer. The abbreviations in this figure mean: deuterium lamp (DL), halogen lamp (HL), mirrors (M), filter-wheel (FW), slit assembly (SA), grating table (G), common beam mask (CBM), optional depolarizing filter (DP), chopper assembly (C), reference beam (R), sample beam (S), photomultiplier tube (PMT) detector and lead sulfide (PbS) detector [11].

The lamp compartment is generally equipped with the deuterium lamp and tungsten-halogen lamp which utilizes a source doubling mirror for UV/Vis/NIR range. A beam splitting system inside a double monochromator is responsible for selecting a specific single wavelength from primary electromagnetic radiation with a wide range of wavelengths. During this process, one beam is directed to the dual sampling compartment and the other is sent to the detector module as a reference. The beam splitting of Perkin Elmer Lambda 1050 UV-Vis-NIR absorption spectrometer comprises a combination of filters, lenses, mirrors, diffraction gratings and slits, respectively. Fig. 3.6 shows a typical diagram of the splitting of a beam. Inside the dual sampling compartment, the sample is positioned inside an integrated sphere which is responsible for collecting the diffusely scattered light during the interaction of an incident beam and the sample [10, 11]. The collected light (I) by the sample and reference beam (I_0) is

reflected by series of mirrors of the optics onto the appropriate detector in the detector compartment connected to an integrating sphere. The detector records the ratio (I/I_0) of the two beams and determine the amount of a beam that has been absorbed (A), reflected ($\%R$) or transmitted ($\%T$). The most popular detectors used in this instrument are PMT detector, which is positioned at the base of the compartment, InGaAs detector and PbS detector positioned at the top of the optics compartment [10, 11].

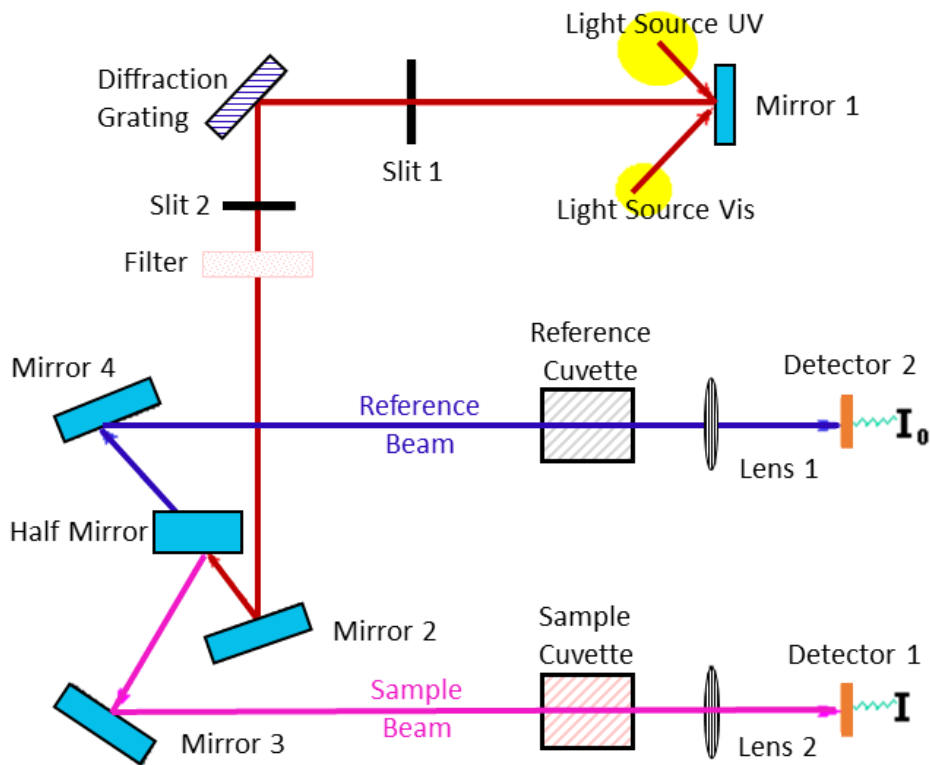


Figure 3.6: Illustration of a double beam UV-Vis instrument [12].

3.5. Photoluminescence Spectroscopy

Photoluminescence Spectroscopy is a popular and useful instrument to study the optical response (e.g. luminescence) from a material following the absorption of electromagnetic waves. Luminescence is generally referred to as an optical transition of the material upon the absorption of the electromagnetic waves of sufficient energy to excite electrons from the ground state to upper electronic state. The excited electrons from the upper electronic state de-excite radiatively to the ground states to recombine with the holes in the form of light (photoluminescence). There are several parameters measured from the materials using photoluminescence spectroscopy such as excitation spectrum, emission spectrum, anisotropy

or polarization, quantum yield as well as luminescence lifetimes (decay curves) [13]. The instrument achieves these parameters using excitation sources, excitation and emission monochromators, sample compartment and the detector, respectively. Amongst the photoluminescence spectroscopy techniques, the Fluorolog[®]-3 spectrofluorometer (Fig. 3.7) is the most popular system that has a unique modular system setup which is equipped with 450W xenon lamp, a few pulsed laser diodes and various detectors (Hamamatsu R928P photomultiplier for UV-visible range, Hamamatsu R2658P photomultiplier for UV-Vis-NIR range, and PbS solid-state detector for NIR-IR range) [14].

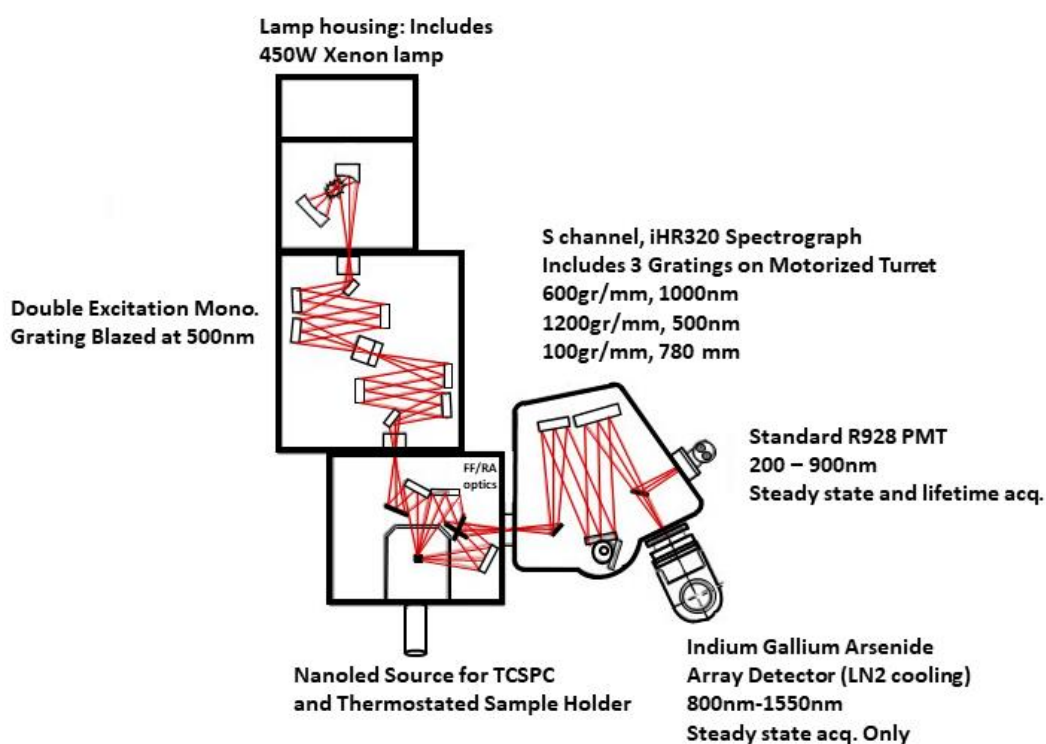


Figure 3.7: Horiba Fluorolog[®]-3 Spectrofluorometer setup schematic [15].

As mentioned above, the incident light sources in this system include a broadband 450 W Xenon lamp and a tunable laser covers the excitation and emission spectra ranging from ultra-violet (UV) to near-IR (NIR). The excitation source is channeled through diffraction gratings and focusing optics inside the monochromator and focused towards the material. The emitted light by the material is then channeled via focusing optics in monochromator to the detector compartment that is 90° to avoid any interference with the transmitted light from source. Finally, the emission spectrum is recorded by the detector and displayed as luminescence intensity as a function emitted light wavelength at room temperature [16].

The spectrofluorometer is also capable for low temperature measurements using the Janis cryostat [14]. In this research, down-conversion measurements were studied using Horiba Fluorolog[®]-3 spectrofluorometer while up-conversion luminescence was recorded by a Hamamatsu R928P photomultiplier tube, which was operated in photon counting mode after passing through a double emission monochromator.

3.6. Time-of-Flight Secondary Ion Mass Spectrometry

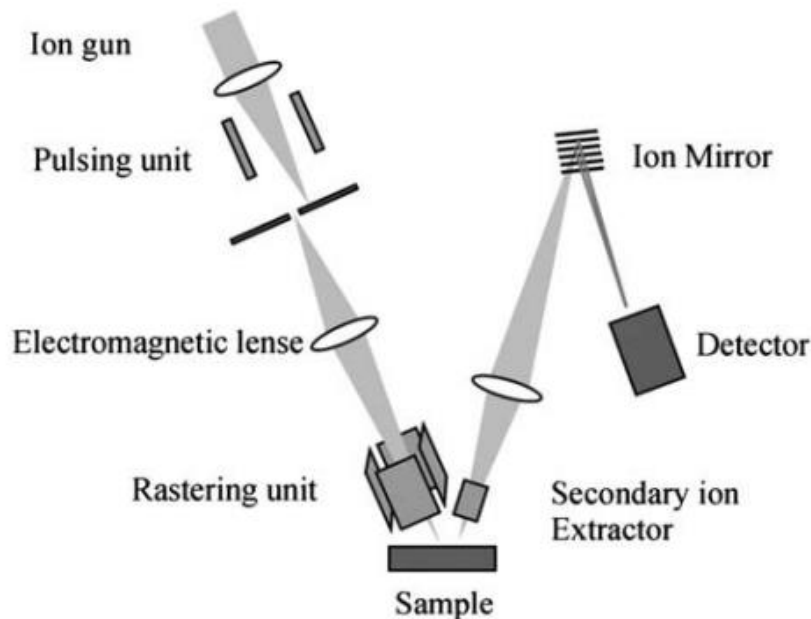


Figure 3.8: Schematic presentation of the ToF-Sims [19].

The Time-of-Flight Secondary Ion Mass Spectrometry (TOF – SIMS) is an analytical technique used for surface analysis that is used to provide information of the surface distribution of species, imaging for mapping, chemical composition, and depth profiling. Fig. 3.8 shows the schematic diagram of the TOF-SIMS. During the analysis, the primary pulsed ion beam used to probe the surface of the target is Bi^+ from an ion gun where it dissociates the surface. The resulting ejected secondary ion species at the surface are accelerated into a column where they fly through the drift path to reach the detector. In this case, the time (time-of-flight) that secondary ions take to get to the detector is measured and the mass of these secondary ions can be determined. Since ions of different elements have different masses, they travel with different velocity and their time-of-flight is also different. Ions with light masses fly faster and they reach the detector before the heavy ions. The difference in the time-of-flight allows to the

detector allows the determination of elements that present over a selected surface area of the target. Upon the arrival of the secondary ions to the detector, the detector performs the time-to-mass conversion and generate the mass spectrum [17, 18]. The ToF-SIMS operates with three modes, namely surface imaging, surface spectroscopy and depth profiling. The surface imaging mode involves the rostering ion beam over the surface of the target whereby chemical maps is obtained. The surface spectroscopy probe elemental and molecular information from the outer monolayers. The depth profiling employs the use of two ion beam for analysis. One ion beam is used for sputtering a crater while the other one is used for analysis of the crater bottom [19, 18]. ToF-SIMS data was collected by iontof Time-of-Flight Secondary Ion Mass Spectrometry (TOF SIMS) at the University of the Free State.

3.7. References

- [1] X-ray diffraction (XRD) instruments, [online] <https://www.rigaku.com/en/products/xrd> [accessed 07 February 2019].
- [2] A.A. Bunaciu, E.G. Udristioiu and H.Y. Aboul-Enein. *Crit. Rev. Anal. Chem.* **45** (2015) 289 – 299.
- [3] X-ray diffraction (XRD) instruments, [online] <https://wiki.anton-paar.com/en/x-ray-diffraction-xrd/> [accessed 07 February 2019].
- [4] K. Inaba, S. Kobayashi, K. Uehara, A. Okada, S.L. Reddy and T. Endo. *Advances in Materials Physics and Chemistry* **3** (2013) 72 – 89.
- [5] H. Yao and K. Kimura. Field Emission Scanning Electron Microscopy for Structural Characterization of 3D Gold Nanoparticle Superlattices. *Modern Research and Educational Topics in Microscopy* (2007).
- [6] A. Kaech. An Introduction to Electron Microscopy Instrumentation, Imaging and Preparation, (2013) 2 – 26.
- [7] Phenom Desktop Electron Microscopy, [online] <http://blog.phenom-world.com/what-is-sem> [accessed 07 February 2019].
- [8] Scanning Electron Microscopes, [online] <https://www.jeol.co.jp/en/science/sem.html> [accessed 07 February 2019].
- [9] C.A. De Caro and C. Haller. UV/VIS Spectrophotometry - Fundamentals and Applications (2015) Mettler-Toledo Publication No. ME-30256131.
- [10] C. Tams and N. Enjalbert. Application note: UV/Vis/NIR Spectroscopy. PerkinElmer, Inc.
- [11] Experimental Techniques, [online] http://shodhganga.inflibnet.ac.in/bitstream/10603/42071/14/8_chapter-2.pdf [accessed 10 February 2019].
- [12] UV vis double beam spectrophotometer, [online] <http://www.fotoimage.org/uv-vis-double-beam-spectrophotometer/> [accessed 10 February 2019].

- [13] Y. Povrozin and B. Barbieri. Fluorescence Spectroscopy (2016) John Wiley & Sons: Handbook of Measurement in Science and Engineering.
- [14] Photoluminescence measurements, [online] <http://www.eagle-regpot.eu/EfI/index.php?pid=52&l=en> [accessed 10 February 2019].
- [15] Fluorescence spectroscopy, [online] <http://fluorescence.ttk.pte.hu/devices.php> [accessed 10 February 2019].
- [16] An introduction to Fluorescence Spectroscopy, [online] <https://www.azooptics.com/Article.aspx?ArticleID=1327> [accessed 10 February 2019].
- [17] Time-of-Flight Secondary Ion Mass Spectrometry (ToF – SIMS), [online] https://serc.carleton.edu/research_education/geochemsheets/techniques/ToFSIMS.html [accessed 13 February 2019].
- [18] Time-of-Flight Secondary Ion Mass Spectrometry (ToF – SIMS), [online] <https://www.iontof.com/tof-sims-secondary-ion-mass-spectrometry.html> [accessed 13 February 2019].
- [19] D. Gode and D.A. Volmer. R. Soc. Chem. **138** (2013) 1289 – 13

Chapter 4: Structural and optical evaluation of NIR up-converting Er³⁺ doped ZnTiO₃-Zn₂TiO₄ composite phosphor

4.1. Introduction

Phosphor nanomaterials based up-conversion (UC) luminescence has attracted great attention for a wide variety of applications in both medical and industrial applications, which include lighting technologies [1], high density optical data readers and storage sensors [2]. The process is anti-Stokes, and occurs by converting two or more photons with low energy, typically that of near infrared excitation, into a single photon with a higher energy [1]. The UC process is normally achieved from trivalent rare earth ions (RE³⁺) incorporated in a suitable host matrix, through these mechanisms; excited-state absorption, energy-transfer up-conversion, and two-photon absorption, which also referred to as photon avalanche [3-5]. The well-known RE³⁺ ions that adhere to the anti-Stokes emission process, and display emission in the visible range of the electromagnetic spectrum, are Tm³⁺, Er³⁺, Ho³⁺, Nd³⁺, Pr³⁺ and Yb³⁺.

Among these ions, Er³⁺ is considered the most efficient in the up-conversion process, due to its versatile energy levels originating from the two thermally coupled manifolds, the ²H_{11/2} and ⁴S_{3/2} states. Er³⁺ up-conversion mechanism is achieved through a combination of ground state absorption and excited state absorption. An excited-state absorption process involves a single emitting ion with energy levels absorbing, where two or more photons excite electrons to successively higher energy excited states. An equivalent energy will excite the same electrons to the next state above, until the highest achievable state. Eventually, the electrons will de-excite from the highest state to the lowest state, and yield photons with higher energies [6-8]. There are several strategies that have been employed to improve the structural and optical properties of dual phase phosphors [9]. Some of the strategies include the fabrication of composites and doping with RE³⁺. Consequently, some of the composite phosphors have been reported including Pr³⁺ doped SrSnO₃-SnO₂ composite phosphor [9], CdTe-SrSO₄ composite phosphors [10], Al₂O₃:Ce-YAG:Gd composite ceramic phosphors [11] and Tm³⁺;Yb³⁺ co-

doped ZnO-TiO₂ composite phosphor [12] for luminescence applications. They found that by varying the molar ratios and the dopants concentrations, the morphologies of the composites can be changed and exhibit high luminous efficiency. In this chapter, we present the structural and optical properties of optimized ZnTiO₃-Zn₂TiO₄:Er³⁺ phosphor synthesized by conventional solid-state reaction. Our interest was to investigate the crystal structure and optical properties of the phosphor for photovoltaics applications. We demonstrated the effects of composite features on crystal.

4.2. Experimental procedure

The ZnTiO₃-Zn₂TiO₄: 2 mol% Er³⁺ phosphor was synthesized using the solid-state chemical reaction method [13]. The starting materials were 1.00 g of ZnO (99.9%), 0.98 g of TiO₂ (99.7%) and 0.14 g of Erbium (III) acetate hydrate (99.9%), and their stoichiometric amounts were first mixed in 50 ml of ethanol inside a glass beaker to prepare the slurry. The slurry was stirred for 1 hour at room temperature for homogeneity and dried inside an oven at 120 °C for 2 hours. The resulting white ZnTiO₃-Zn₂TiO₄:Er³⁺ phosphor was annealed at 1100 °C for 4 hours in air, inside a furnace and ground gently using a pestle and mortar. The phase formation of the crystal structure was probed using an X-ray diffractometer (Rigaku Smartlab) that was equipped with a monochromatic CuK α ($\lambda = 0.015405$ nm) irradiation source that was operated at 200 mA current. A Jeol JSM-7800 field emission scanning electron microscope (FE-SEM) was used to study particle morphology. In addition, the diffuse reflectance of the phosphor was evaluated using UV-Vis-NIR absorption spectroscopy (Perkin Elmer Lambda 1050). The photoluminescence (PL) measurements were conducted using a PL spectrometer from Edinburgh Instruments FLS980 consisting of a 980 nm (2W) diode laser as the excitation source. After passing through a double emission monochromator, the up-conversion luminescence was recorded by a Hamamatsu R928P photomultiplier tube, which was operated in photon counting mode. The photoluminescence measurements were carried out at room temperature.

4.3. Results and discussion

4.3.1. Structural and morphological analysis

The XRD patterns presented in Fig. 4.1(a) correspond to the undoped and Er³⁺ doped ZnTiO₃-Zn₂TiO₄ phosphors, in the range of 10 – 90 ° (2θ). The patterns of the undoped and the Er³⁺

doped $\text{ZnTiO}_3\text{-Zn}_2\text{TiO}_4$ samples show diffraction peaks corresponding to the crystal planes of hexagonal ZnTiO_3 phase (JCPDS card no. 26-1500) with space group R3 and cubic spinel Zn_2TiO_4 phase (JCPDS card no. 13-0536 and 13-1493) with space group Fd3m, respectively. The presence of the different phases indicates that we have formed a composite phosphor. Some peaks corresponding to impurities originating from TiO_2 according to the JCPDS standard file with card number 75-1753, were also observed on the patterns. The formation of

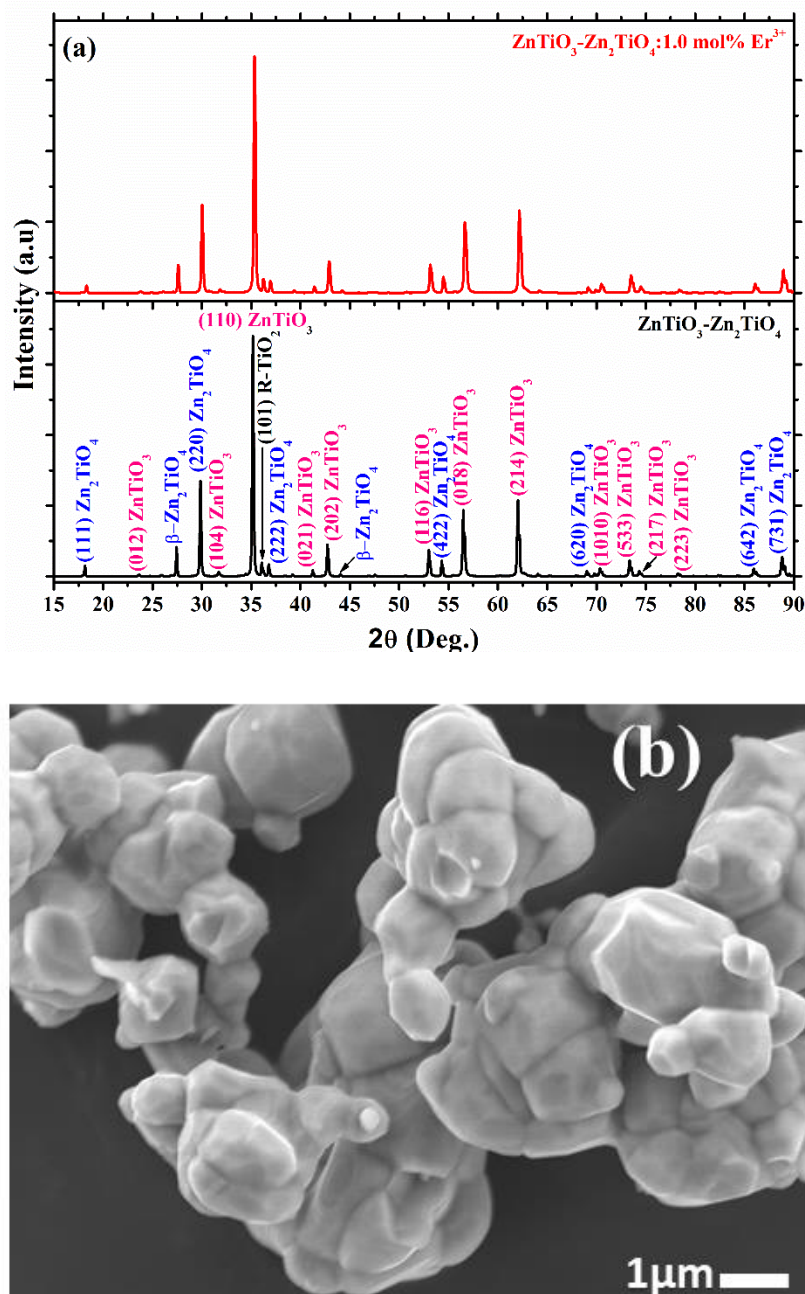


Figure 4.1: X-ray Diffraction patterns of (a) $\text{ZnTiO}_3\text{-Zn}_2\text{TiO}_4$ and $\text{ZnTiO}_3\text{-Zn}_2\text{TiO}_4:\text{Er}^{3+}$ and (b) FE-SEM micrograph of $\text{ZnTiO}_3\text{-Zn}_2\text{TiO}_4:\text{Er}^{3+}$ phosphors annealed at 1100°C .

rutile-TiO₂ (R-TiO₂) is due to the decomposition of ZnTiO₃ when the prepared samples were annealed at high temperature [14]. Fig. 4.1 (b) shows the FE-SEM micrograph of Er³⁺ doped ZnTiO₃-Zn₂TiO₄ composite. The morphology of the prepared sample consists of agglomeration of faceted spheres and hexagons. The agglomerated morphology is due to annealing the samples at high temperatures [15]. Consistent with XRD data, the SEM image have shown that doping with Er³⁺ did not change the crystal morphology since the XRD patterns of the two materials are the same.

4.3.2. UV-Vis-NIR analysis

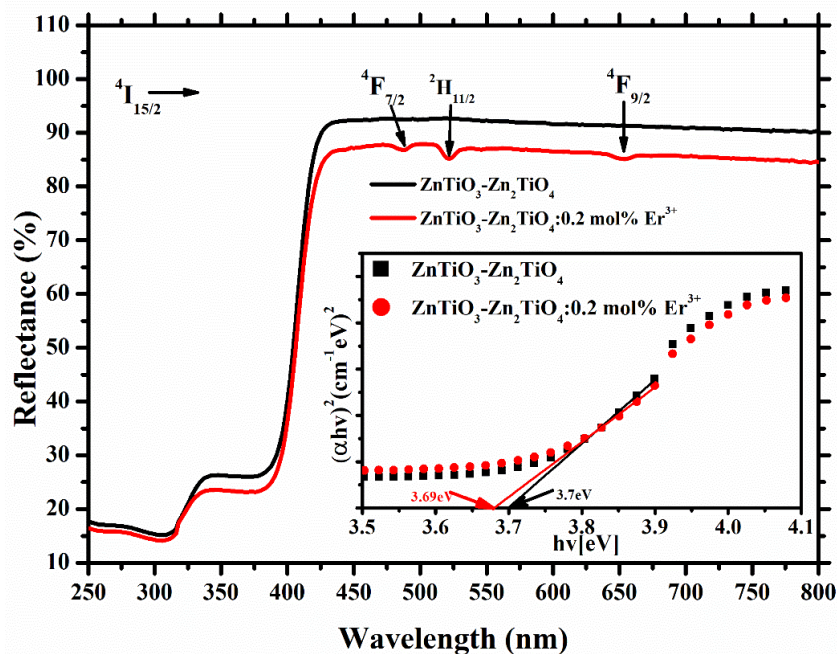


Figure 4.2: Reflectance spectra of ZnTiO₃-Zn₂TiO₄ and ZnTiO₃-Zn₂TiO₄:Er³⁺ phosphors.

The absorption properties of the un-doped and Er³⁺-doped ZnTiO₃-Zn₂TiO₄ phosphors are displayed in the diffuse reflectance spectrum shown in Fig. 4.2. The spectra show an intense UV absorption band below 400 nm, due to band to band absorption [16] and a charge transfer state that exists within the band gap of the material. The charge transfer state in CaTiO₃ compounds originates from an intervalence charge transfer state [17], and the one observed in Fig. 4.2 is likely to originate from it. In addition, absorption bands centred at 488, 520 and 653 nm in the visible and NIR spectral region were detected. These bands correspond to ⁴I_{15/2} state to higher ⁴F_{7/2}, ²H_{11/2} and ⁴F_{9/2} transitions of Er³⁺ ions [16, 18]. The inset in Fig. 4.2 shows the estimated bandgap from the Tau's relation [19] (calculations not shown) for the two samples.

4.3.3. Up-conversion analysis

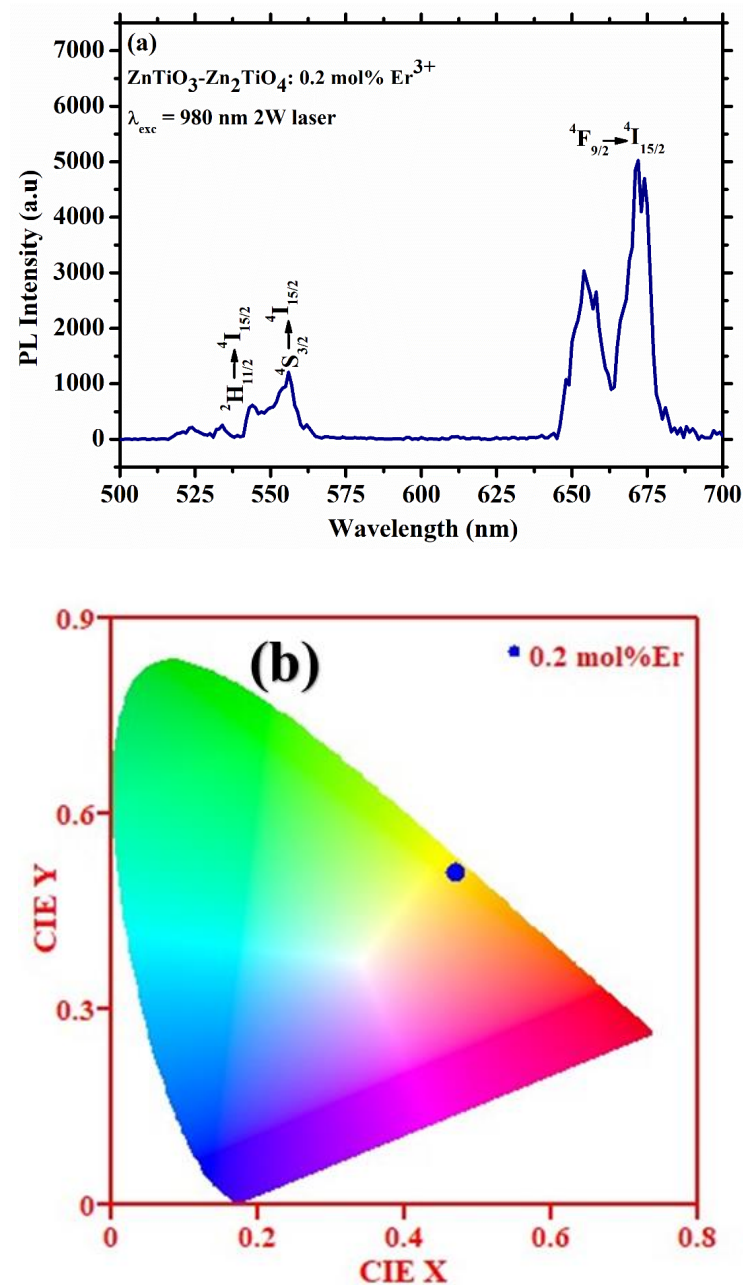


Figure 4.3: (a) PL Spectrum and (b) the CIE coordinate plot of $\text{ZnTiO}_3\text{-Zn}_2\text{TiO}_4: \text{Er}^{3+}$ phosphor.

The up-conversion emission spectrum of $\text{ZnTiO}_3\text{-Zn}_2\text{TiO}_4:\text{Er}^{3+}$ phosphor was measured using a 980 nm diode laser with a pumping power of 2W. Fig. 4.3(a) shows the resulting emission spectrum with peaks in the visible range of the electromagnetic spectrum, indicating successful up-conversion of the NIR photon energies. The displayed green and red emission lines,

positioned at 514 – 574 nm and 640 – 690 nm, correspond to $^2H_{11/2} \rightarrow ^4I_{15/2}$, $^4S_{3/2} \rightarrow ^4I_{15/2}$ and $^4F_{9/2} \rightarrow ^4I_{15/2}$ transitions of Er^{3+} ions, respectively [20 - 24]. The Commission Internationale de l’Eclairage (CIE) chromaticity coordinate plot (Fig. 4.3b), suggests that observed emission resembles a greenish-yellow colour with an index ($X= 0.38$, $Y= 0.61$).

Fig. 4.4 shows the luminescence decay curve of $ZnTiO_3-Zn_2TiO_4:Er^{3+}$, which was recorded by monitoring emission peak at 657 nm, after exciting the phosphor with a 980 nm diode laser pumped with 2W power for a period of 2 ms. The decay curve was fitted using the second-order exponential decay function [15], respectively:

$$I(t) = I_o + Ae^{(-t/\tau I)} \quad [4.1]$$

where I is the luminescence intensity at certain time t , I_o is the background intensity, t is the time, A and B are the constants and τ_I is the luminescent decay time. The measured luminescent decay time τ_I was estimated to 0.267 ms.

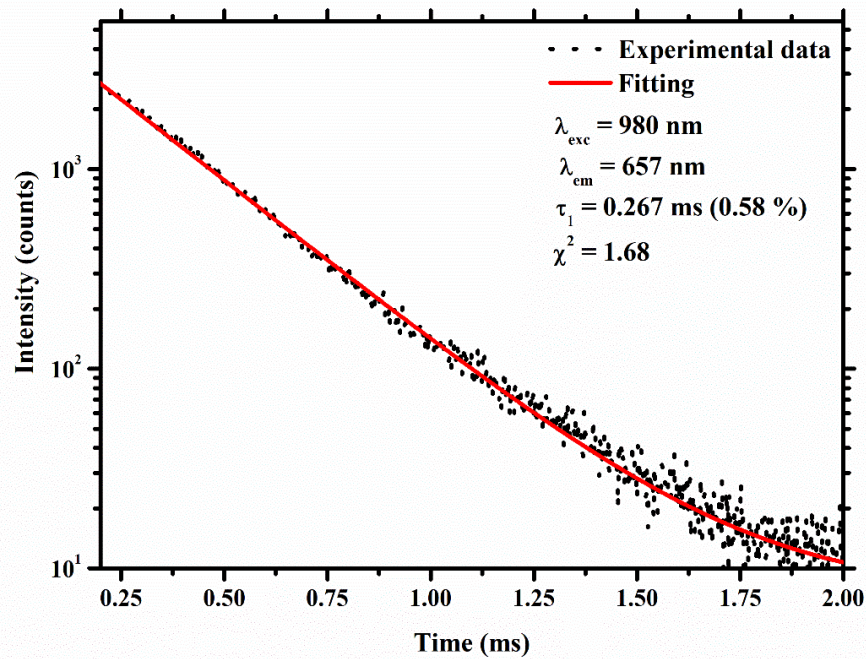


Figure 4.4: Luminescence decay curve of $ZnTiO_3-Zn_2TiO_4: Er^{3+}$ phosphor.

4.4. Conclusion

We successfully prepared an Er^{3+} doped $ZnTiO_3-Zn_2TiO_4$ composite phosphor using solid state chemical reaction at 1100 °C, as proven by the diffuse reflectance and PL data. The morphology of the composites showed faceted and hexagon particle shapes. The photons with

energies corresponding to the NIR emission range, where successfully up-converted to photon energies corresponding to the visible emission range, using Er^{3+} as a dopant ion. The CIE coordinate plot proved that the displayed emission resembled a reddish-yellow colour with an index ($X= 0.47$, $Y= 0.51$) and the obtained lifetime values corresponding to Er^{3+} ions was calculated. These results suggest that this phosphor is a possible candidate that can be used to enhance the power conversion efficiency of different types of solar cells.

4.5. References

- [1] Z. He, X.Y. Sun and X. Gu. *Ceram. Int.* **43(9)** (2017) 7378 – 7382.
- [2] X. Li, Y. Yu and Z. Zheng. *Ceram. Int.* **42(1)** (2016) 490 – 494.
- [3] R.K. Tamrakar, D.P. Bisen, K. Upadhyay and I.P. Sahu. *J. Phys. Chem. C.* **119 (36)** (2015) 21072 – 21086.
- [4] C. Zenghui, G. Yongyi, T. Congbing and L. Yunxin. *J. Rare Earths* **33(7)** (2015) 679 – 685.
- [5] M.R. Dousti and R.J. Amjad. *Measurement.* **105** (2017) 114 – 119.
- [6] P. Ramasamy, P. Manivasakan and J. Kim. *RSC Adv.* **4** (2014) 34873 – 34895.
- [7] Tanvi, A. Mahajan, S. Kumar, V. Saxena and D.K. Aswal. *Chem. Phys. Lett.* **658** (2016) 276 – 281.
- [8] A. Nadort, J. Zhao and E.M. Goldys. *Nanoscale* **8** (2016) 13099 – 13130.
- [9] X. Tian, F. Zhou, X. Liu, H. Zhong, J. Wen, S. Lian, C. Ji, Z. Huang, Z. Chen, H. Peng, J. Li, J. Hu and Y. Peng. *J. Solid State Chem.* **280** (2019) 120997 – 121009.
- [10] D.W. Zhang, W. Zhou, Z.G. Xi, Z. Zhan and X.T. Li. *Mater. Res.* **121** (2020) 110639 – 110644.
- [11] X. Liu, X. Qian, Z. Hu, X. Chen, Y. Shi, J. Zou and J. Li. *J. Eur. Ceram. Soc.* **20** (2019) 2149 – 2154.
- [12] K. Kobwittaya, Y. Oishi, T. Torikai, M. Yada, T. Watari and H.N. Luitel. *Vacuum* **148** (2018) 286 – 295.
- [13] S. Ayed, H. Abdelkefi, H. Khemakhem and A. Matoussi. *J. Alloys Compd.* **677** (2016) 185 – 189.
- [14] L. Mengting and J. Baoxiang. *J. Rare Earths.* **33(3)** (2015) 231 – 238.
- [15] S.W. Oh, H.J. Bang, Y.C. Bae and Y.K. Sun. *J. Power Sources* **173** (2007) 502 – 509.
- [16] S.J. Mofokeng, V. Kumar, R.E. Kroon and O.M. Ntwaeaborwa. *J. Alloy. Compd.* **711** (2017) 121 – 131.
- [17] L.L. Noto, S.S. Pitale, M.A. Gusowki, J.J. Terblans, O.M. Ntwaeaborwa and H.C. Swart. *Powder Technol.* **237(141)** (2013) 141 – 146.

- [18] Y. Li, C. Ni, C.C. Lin, F. Pan, R.S. Liu and J. Wang. *Opt. Mater.* **36(11)** (2014) 1871–1873.
- [19] O.M. Ntwaeaborwa, S.J. Mofokeng, V. Kumar and R.E. Kroon. *Spectrochim. Acta A Mol. Biomol. Spectrosc.* **82** (2017) 1 42 – 49.
- [20] J. Janek, J. Lisiecki, W. Ryba-Romanowski, J. Pisarska and W.A. Pisarski. *Opt. Mater.* **74** (2017) 105 – 108.
- [21] L. Strizik, J. Zhang, T. Wagner, J. Oswald, T. Kohoutek, B.M. Walsh, J. Prikryl, R. Svoboda, C. Liu, B. Frumarova, M. Frumar, M. Pavlista, W.J. Park and J. Heo. *J. Lumin.* **147** (2014) 209 – 215.
- [22] X. Li, Y. Yu and Z. Zheng. *Ceram. Int.* **42** (2016) 490 – 494.
- [23] Z. He, X.Y. Sun and X. Gu. *Ceram. Int.* **43(9)** (2017) 7378 – 7382.
- [24] S.I. Rivera, F.J. Carrillo, A. Garcia and J. Oliva. *Mater. Lett.* **187** (2017) 83 – 85.

Chapter 5: Structural and optical evaluation of NIR up-converting $x\text{mol}\%\text{Er}^{3+}$ doped $\text{ZnTiO}_3\text{-Zn}_2\text{TiO}_4$ composite phosphor

5.1. Introduction

Rare earth (RE^{3+}) ions incorporated in a suitable host matrix are valued for efficient up-conversion (UC) processes in the field of luminescence. The UC luminescence properties of RE^{3+} activated optical materials have attracted great attention for a wide variety of application, which include, biomedical imaging, optical sensors, lighting technologies, optical amplifiers, storage sensors, etc. [1-3]. The UC process is an anti-Stokes type of an emission, and it occurs by converting two or more photons with low energy, typically that of near infrared (NIR) excitation, into a single photon with a higher energy [2]. Erbium (Er^{3+}) adheres to anti-Stokes emission because it consists of two thermally coupled manifolds, namely the $^2\text{H}_{11/2}$ and $^4\text{S}_{3/2}$ states, which support the up-conversion mechanism. When a host lattice doped with Er^{3+} ions, is excited with an infrared beam of light, the electrons are excited from the lowest Er^{3+} state to the next state above, until the highest achievable state through a combination of GSA-ESA processes. During this process, the electrons de-excite from the highest metastable state to lower states radiatively, resulting in green and red emissions [4-6].

Nanocomposites are materials that are made up of several constituent materials embedded in continuous phases, where at least one or all phases have an average particle size less than 100 nm. Nanocomposites offer a great advantage over individual nanomaterials because they produce multifunctional phases with exceptionally enhanced properties as well as different physical and mechanical properties [7, 8]. The semiconductor nanocomposites have found to be beneficial in many fields like light emitting diode, photodetectors, field effect transistors and for the production of high performance photovoltaic (PV) devices. An important finding from the semiconductors nanocomposites is the superior enhancement in optical and electronic

properties compared to pure conjugated semiconductors nanomaterials or conventional composites [9]. In addition, the semiconductor nanocomposites can be easily tuned by doping since the incorporation of RE^{3+} relaxes the f-f transition of semiconductors thereby enhancing their absorption cross-section [10]. In this study, $ZnTiO_3$ - Zn_2TiO_4 : Er^{3+} nanocomposite phosphor was successfully synthesized by conventional solid-state reaction method. The crystal structure, surface morphology and optical properties of the nanocomposite material were probed, in order to investigate its effect on photoluminescence emission properties of Er^{3+} .

5.2. Experimental procedure

Er^{3+} ions doped $ZnTiO_3$ - Zn_2TiO_4 nanocomposite phosphor was synthesized by solid-state chemical reaction method, using ethanol to prepare the slurry. The starting materials were 1.00 g of ZnO (99.9%), 0.98 g of TiO_2 (99.7%) and different amount of Erbium (III) acetate hydrate (99.9%), which were mixed in stoichiometric amounts in 50 ml of ethanol. The slurry was dried inside an oven at 120 °C for 2 hours, then fired at 1100 °C for 4 hours in air. The resulting white phosphor compound was ground gently using a pestle and mortar until a uniform white powder. The phase identification of the crystal structure and the particle morphology was probed using an X-ray diffractometer (Rigaku Smartlab) and Jeol JSM-7800 field emission scanning electron microscope (FE-SEM). The diffuse reflectance spectrum was recorded using a Perkin Elmer Lambda 1050 UV-Vis-NIR absorption spectrometer. The photoluminescence emissions (PL) and lifetime measurements were conducted using a PL spectroscopy from Edinburgh Instruments FLS980 consisting of a 980 nm (2W) diode laser as an excitation source for up-conversion luminescence. Up-conversion luminescence was recorded by a Hamamatsu R928P photomultiplier tube, which was operated in photon counting mode after passing through a double emission monochromator.

5.3. Results and discussion

5.3.1. Structural analysis

The X-ray Diffraction patterns of undoped and Er^{3+} doped $ZnTiO_3$ - Zn_2TiO_4 nanocomposite phosphor annealed at 1100°C for 4 hours are shown in Fig. 5.1. The patterns show the diffraction peaks of different phases, which correspond to the crystal planes of the hexagonal

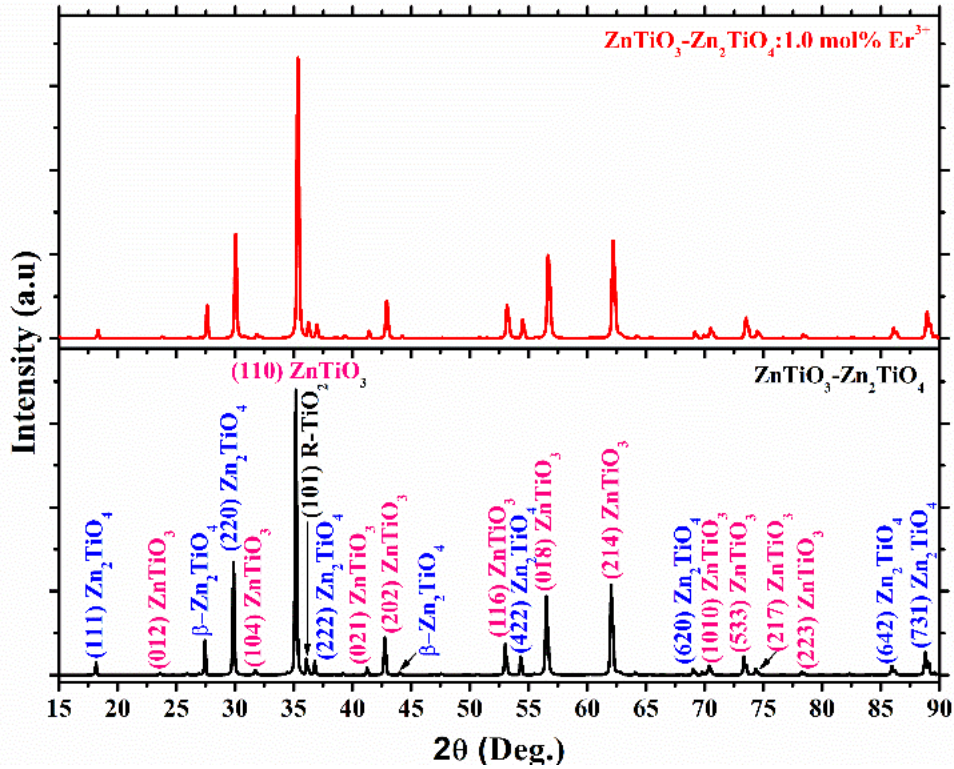


Figure 5.1: X-ray Diffraction patterns of $\text{ZnTiO}_3\text{-Zn}_2\text{TiO}_4$ and $\text{ZnTiO}_3\text{-Zn}_2\text{TiO}_4\text{:Er}^{3+}$ annealed at 1100°C .

ZnTiO_3 phase (JCPDS card no. 26-1500) with space group $R-3$, the cubic spinel Zn_2TiO_4 phase (JCPDS card no. 13-0536) with space group $Fd3m$, and the $\beta\text{-Zn}_2\text{TiO}_4$ phase (JCPDS card no. 13-1493) suggesting the crystallization of mixed phases (composite). The sharp diffraction peaks confirm high crystallinity of the structure of $\text{ZnTiO}_3\text{-Zn}_2\text{TiO}_4$ composite phosphor. The most prominent diffraction peaks observed in the $\text{ZnTiO}_3\text{-Zn}_2\text{TiO}_4$ nanocomposite phosphors are for hexagonal ZnTiO_3 . The diffraction peak at 36° , corresponds to an additional secondary phase, which matches with the $r\text{-TiO}_2$ standard, according to the JCPDS file with card number 75-1753. The formation of this secondary phase is due to the decomposition of hexagonal ZnTiO_3 phase into Zn_2TiO_4 and $r\text{-TiO}_2$ when the prepared composites were annealed at 1100°C [11, 12]. The relative phases of ZnTiO_3 and Zn_2TiO_4 were extracted from the ratio of intensities ($I_{\text{phase}}/I_{\text{total}}$) of the (110) reflection of ZnTiO_3 , (110) reflection of Zn_2TiO_4 , and (110) reflections of $R\text{-TiO}_2$ and $\beta\text{-Zn}_2\text{TiO}_4$. The percentages of ZnTiO_3 and Zn_2TiO_4 phases in

the composite were calculated using the relation [13]:

$$\text{Relative phase content} = I_{(\text{phase})}/I_{(\text{total})} \quad (1)$$

where $I(\text{phase})$ is the intensity of selected peak from the peak position that consists of only one phase and $I(\text{total})$ is the sum of intensity of all selected Xray diffraction peaks. The percentage of ZnTiO_3 and Zn_2TiO_4 phases were found to be $\sim 68.2\%$ and $\sim 27.0\%$, respectively. In addition, the XRD pattern of Er^{3+} doped $\text{ZnTiO}_3\text{-Zn}_2\text{TiO}_4$ nanocomposite phosphor did not show any peaks of Er_2O_3 , indicating that doping of Er^{3+} has no effect on the structure of $\text{ZnTiO}_3\text{-Zn}_2\text{TiO}_4$ nanocomposite phosphors. Since the ionic radius of Er^{3+} ions is bigger than that of both Zn^{2+} and Ti^{4+} ions, it is expected to occupy the position of the ion with the greater ionic radius between the two. The ionic radius of Zn^{2+} ions is bigger than that of Ti^{4+} ions and therefore Er^{3+} ions is expected to occupy Zn^{2+} ions [12, 14].

5.3.2. Morphological analysis

The SEM micrographs of the undoped and Er^{3+} doped $\text{ZnTiO}_3\text{-Zn}_2\text{TiO}_4$ composite phosphors are presented in Fig. 5.2 and shows the agglomerations of faceted spheres and hexagons. The agglomeration has been attributed to annealing the samples at high temperatures [15]. Consistent with the XRD results, the HR-SEM micrographs shown in Fig. 5.2(b) confirm that the incorporation of Er^{3+} ions did not influence the particle morphology of the $\text{ZnTiO}_3\text{-Zn}_2\text{TiO}_4$ composite.

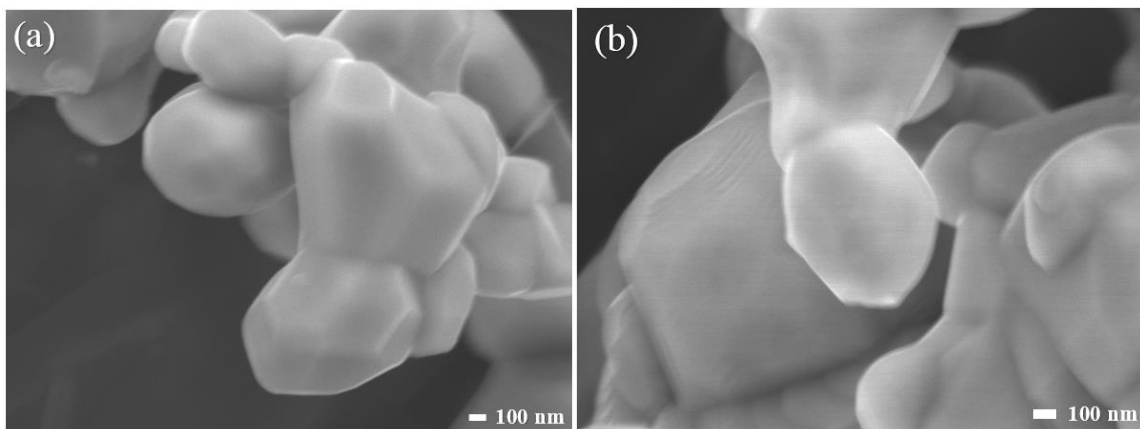


Figure 5.2: FE-SEM micrographs of (a) $\text{ZnTiO}_3\text{-Zn}_2\text{TiO}_4$ and (b) $\text{ZnTiO}_3\text{-Zn}_2\text{TiO}_4\text{:Er}^{3+}$ composites.

5.3.3. UV-Vis analysis

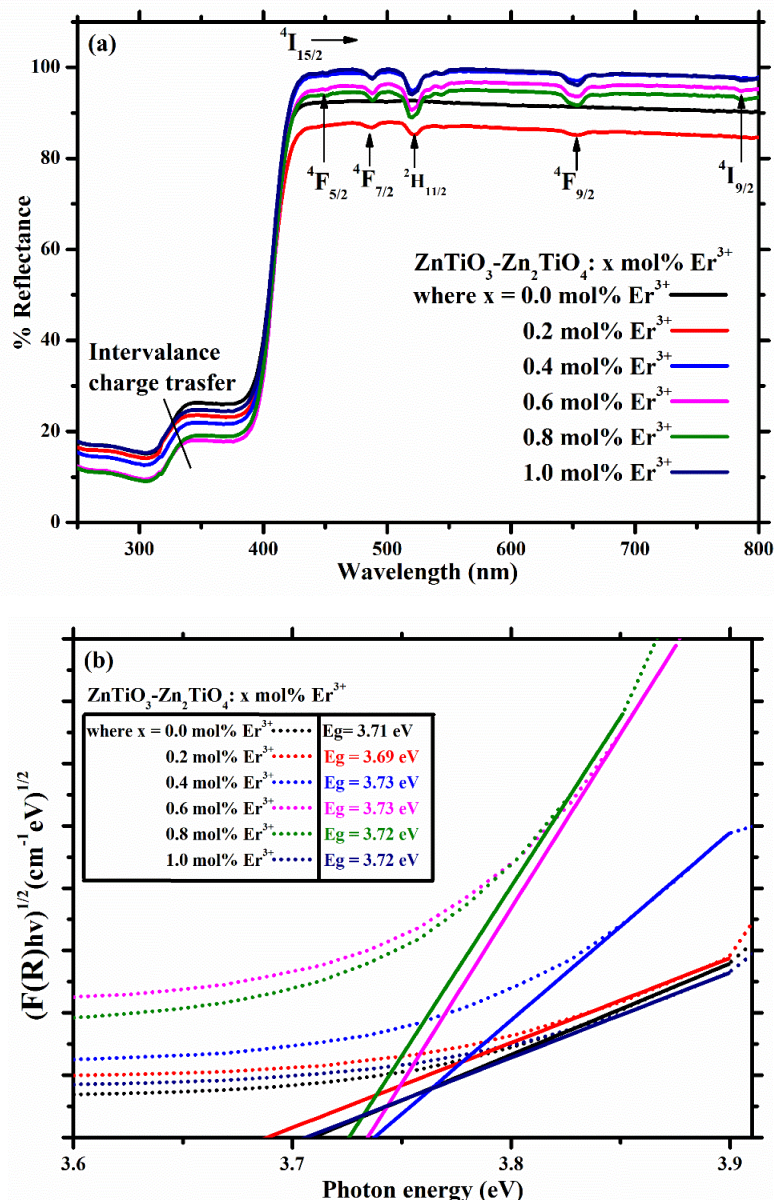


Figure 5.3: (a) The diffuse reflectance spectra and (b) Kubelka Munk's plots of ZnTiO₃-Zn₂TiO₄: x mol% Er³⁺ (0.0 ≤ x ≤ 1.0 mol%).

The absorption characteristics of the ZnTiO₃-Zn₂TiO₄:Er³⁺ composite phosphor is displayed in the diffuse reflectance spectra (Fig. 5.3a). The spectra shows major absorption below 400 nm which is due to band-band absorption [16] and five absorption bands above 400 nm, which are attributed to the electric dipole transitions from the ground state ⁴I_{15/2} of Er³⁺ ions to the different excited states: ⁴I_{15/2} → ⁴F_{5/2}, ⁴I_{15/2} → ⁴F_{7/2}, ⁴I_{15/2} → ⁴H_{11/2}, ⁴I_{15/2} → ⁴F_{9/2}, and ⁴I_{15/2} → ⁴I_{9/2} [17, 18]. The spectra also show the charge transfer state that overlaps the band gap below

400 nm. The charge transfer state was observed and explained in CaTiO₃ compounds to originate from an intervalence charge transfer state due to an electron that is shared between the Ti⁴⁺ state [19], and charge transfer state observed in Fig. 5.3 (a) is likely to originate from ZnTiO₃. The expression for Kubelka-Munk function $F(\mathbf{R})$, as a function of photon energy ($h\nu$) for indirect and direct allowed transitions for semiconductors, have been employed to evaluate the optical energy band gap (E_g), using the fundamental absorption edges from the reflectance and absorption spectra of the materials [20]. The Schuster-Kubelka-Munk relation can be express as:

$$F(\mathbf{R}) = \frac{(1-R_\infty)^2}{2R_\infty} = \frac{K}{S} \quad [5.1]$$

where R_∞ , K , S are the diffused reflectance, molar absorption coefficient and the scattering coefficient. Fig. 5. 3(b) shows the estimated bandgap energies from the Kubelka-Munk relation of $(F(\mathbf{R})h\nu)^n$ against photon energy ($h\nu$), with $n = 1/2$ for the prepared samples. It is known that perovskite ZnTiO₃ and spinel Zn₂TiO₄ are indirect ($n = 1/2$) and direct ($n = 2$) allowed transition in a semiconductor material [21]. We chose indirect allowed transition ($n = 1/2$) because XRD and SEM results showed that the perovskite zinc titanate is more dominant over the spinel zinc titanate in the prepared composite. The estimated fundamental energy bandgap of the host ZnTiO₃-Zn₂TiO₄ is 3.71 eV as shown in the inset from Fig. 5.3 (b). It can be seen that there is a slight fluctuation in energy bandgap for different dopant concentrations of Er³⁺ ions. This is attributed to the possible shift of the Fermi level and excess charge carries for different dopant concentrations, as described by Burstein-Moss effect [16, 22].

5.3.4. Up-conversion luminescence analysis

The photoluminescence up-conversion emission spectra of ZnTiO₃-Zn₂TiO₄:Er³⁺ composite phosphor (Fig. 5.4a) were measured using a 980 nm diode laser with a pumping power of 2W. The inset in the top right shows PL emission spectrum of the un-doped host ZnTiO₃-Zn₂TiO₄, confirming that there was no emission from the host lattice when excited at 980 nm. The emission spectra of ZnTiO₃-Zn₂TiO₄:Er³⁺ show green and red photoluminescence emissions, indicating successful up-conversion of the NIR photon energies. The green and red emissions centred at 541-574 nm and 640-690 nm, correspond to ²H_{11/2} → ⁴I_{15/2}, ⁴S_{3/2} → ⁴I_{15/2} and ⁴F_{9/2} → ⁴I_{15/2} intra 4f-4f electronic transitions of Er³⁺ ions, respectively [23-27]. The spectra show minor peaks (shoulders) in the vicinity of the green emission while the red emission is split

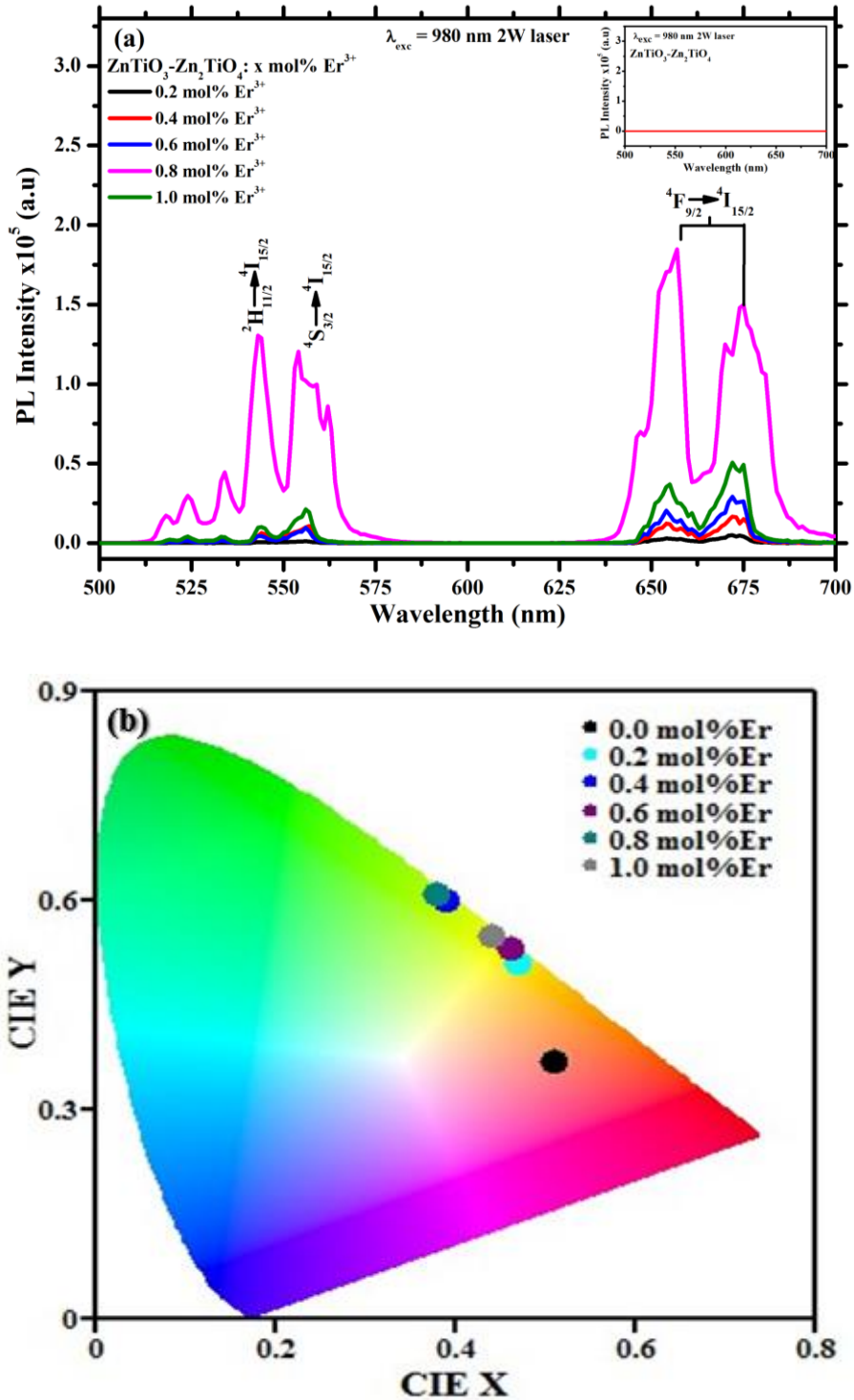


Figure 5.4: (a) Up-conversion emission spectra and (b) CIE coordinate plot of ZnTiO₃-Zn₂TiO₄:Er³⁺ composite phosphor.

into two strong peaks. This type of peaks emanates from Er³⁺ ion pairs and are attributed to the splitting sublevel manifolds of Er³⁺ 4f \rightarrow 4f transitions due to the Stark effect from the crystal field of the host composite [18, 28, 30]. The up-conversion emission intensity is enhanced with

an increase in Er^{3+} concentration. It is known that the PL intensity of lighting materials is affected by concentration quenching effect [28, 29, 31, 32], and it therefore necessitates a search for the concentration that yields the optimal luminescence intensity. The maximum PL intensity was observed from the composite phosphor that was doped with the Er^{3+} concentration of 0.8 mol%. The CIE chromaticity coordinate plot (Fig. 5.4b) suggests that the overall observed emission colour from the doped composite phosphors is yellowish green resulting from a combination of strong green and red emissions.

Energy level diagram of Er^{3+} ions doped $\text{ZnTiO}_3\text{-Zn}_2\text{TiO}_4$ showing the up-conversion PL mechanism under NIR excitation of 980 nm is shown in Fig. 5.5(a). Under the excitation of 980 nm, Er^{3+} ions at the ground state $^4\text{I}_{15/2}$ were initially excited to the $^4\text{I}_{11/2}$ state through ground state absorption (GSA) process. The Er^{3+} ions located at $^4\text{I}_{11/2}$ state are promoted to the $^4\text{F}_{7/2}$ intermediate state of Er^{3+} through excited-state absorption (ESA) as shown in (I) from Fig 5.5(a). two (2) or more energy photons whereby it is promoted to higher excited states. From (I) in Fig. 5.5(a), the non-radiative relaxation was observed from Er^{3+} ions situated at the $^4\text{I}_{11/2}$ state to different states ($^2\text{H}_{11/2}$, $^4\text{S}_{3/2}$ and $^4\text{F}_{9/2}$) followed by radiative relaxation decay corresponding to green ($^2\text{H}_{11/2}$, $^4\text{S}_{3/2} \rightarrow ^4\text{I}_{15/2}$) and red ($^4\text{F}_{9/2} \rightarrow ^4\text{I}_{15/2}$) emissions [31]. An excited-state absorption process is considered as one of the main up-conversion mechanisms in RE^{3+}

ions and it involves a single emitting ion with energy levels absorbing This mechanism also shows the splitting of radiative relaxation for red emission as shown in (II) from Fig. 5.5(a). According to Sardar et al [31], the inter-manifold transitions of Er^{3+} in host materials can be obtained using the following relation: $2n + 1$ in $^{2n+1}\text{L}_J$. The $^4\text{I}_{11/2}$ state of Er^{3+} , has $2(4) + 1 = 9$ multiplet manifolds, which are achievable, as shown in (II) from Fig. 5.5(a). The broad red PL emission observed in Fig. 5.4, is a result of electron transitions from the $^4\text{F}_{9/2}$ state to several multiplet manifolds of $^4\text{I}_{11/2}$ state. The number of photons involved in the mechanism of up-conversion under 980 nm excitation, can be determined from the double log plot of power dependence of the up-conversion luminescence intensity. This relationship can be expressed as [23]:

$$\log(I) = n \log(P) \quad [5.2]$$

where I , P and n are the UC luminescence intensity, pump power and the number of excitation photons absorbed for up-conversion process, respectively. The value of “ n ” is obtained from

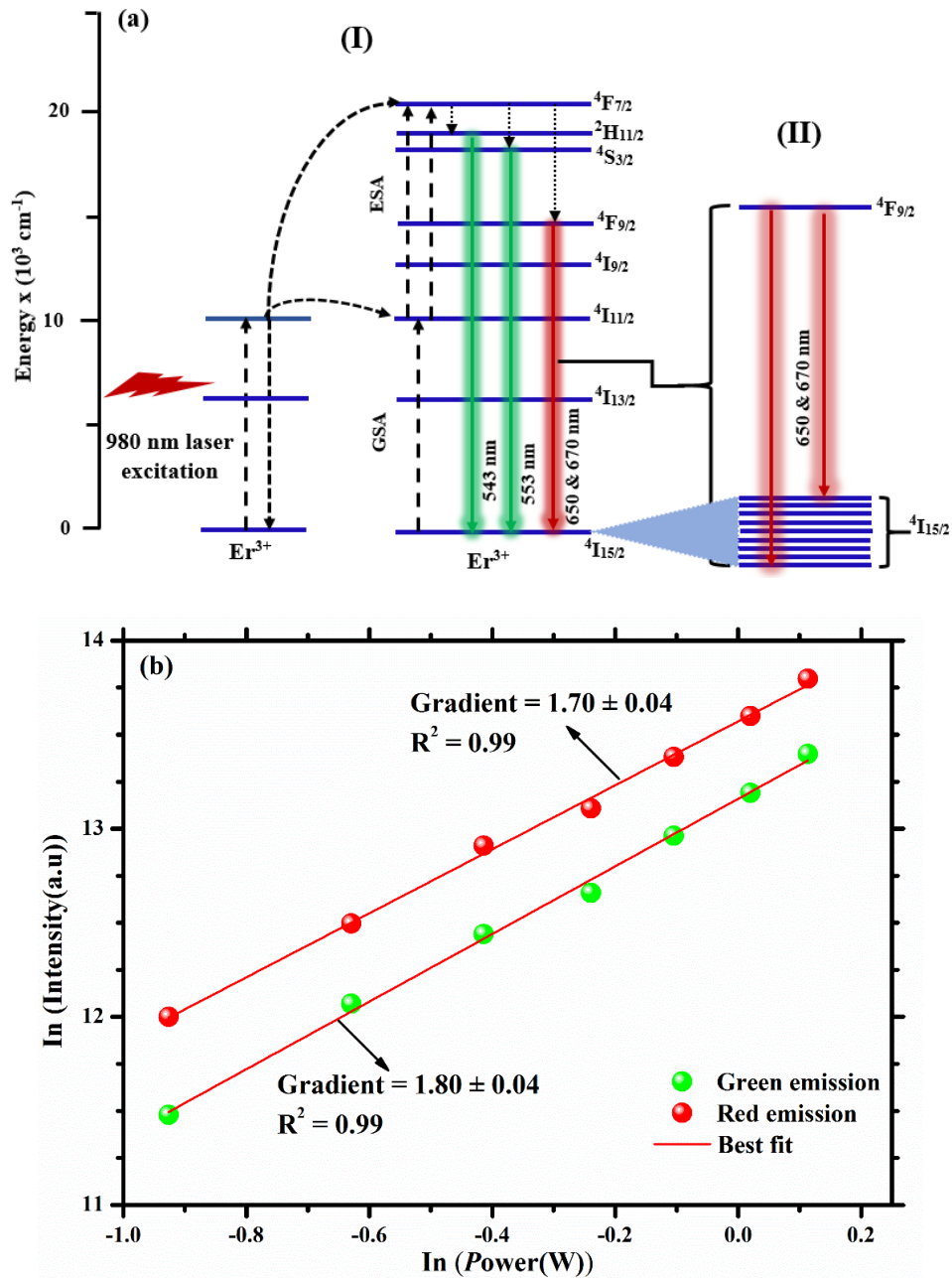


Figure 5.5: (a) Energy level diagram of Er^{3+} ions and (b) power dependence of PL intensity curves.

the slope of the linear fit of the double log plot as shown in equation (3). The double log plots of up-converted luminescence intensity versus pumping power under 980 nm excitation for $\text{ZnTiO}_3\text{-Zn}_2\text{TiO}_4\text{:}0.8 \text{ Er}^{3+}$ are presented in Fig. 5.5(b). The fitting results show linearity relationship between emission intensity related to $4\text{S}_{3/2} \rightarrow 4\text{I}_{15/2}$ and $4\text{F}_{9/2} \rightarrow 4\text{I}_{15/2}$ transitions of Er^{3+} and laser power output. The estimated n values from the plot are approximately 1.80 ± 0.04 and 1.70 ± 0.04 for green and red emissions, respectively. These excitation photons

indicate that a double photon mechanism was involved in the up-converted luminescence of Er^{3+} ions, respectively.

Fig. 5.6 shows the luminescence decay curve of $\text{ZnTiO}_3\text{-Zn}_2\text{TiO}_4\text{:Er}^{3+}$, which was recorded by monitoring emission peak at 657 nm, after exciting the phosphor with a 980 nm. From the decay profile only, a single component is observed, and therefore it was fitted using the first order exponential decay function [34]:

$$I(t) = I_o + Ae^{(-t/\tau_1)} \quad [5.3]$$

where I is the luminescence intensity at certain time t , I_o is the background intensity, t is the time, A is the constant and τ_1 is the luminescent decay time. The measured luminescent decay time (τ) was estimated to 0.267 ms.

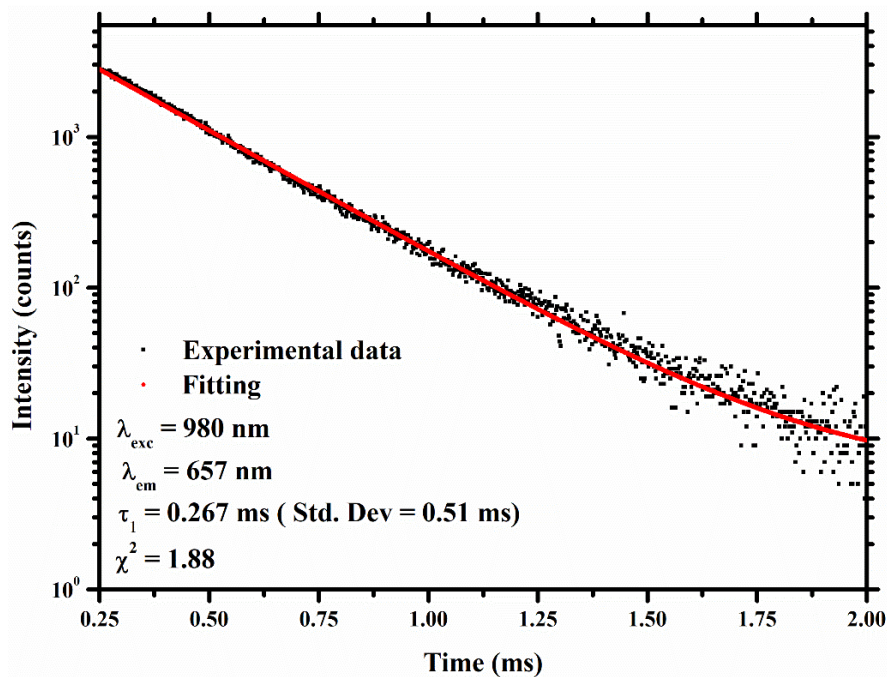


Figure 5.6: Decay curve of $\text{ZnTiO}_3\text{-Zn}_2\text{TiO}_4\text{:Er}^{3+}$ composite phosphor.

5.4. Conclusion

We successfully prepared an Er^{3+} doped $\text{ZnTiO}_3\text{-Zn}_2\text{TiO}_4$ composite phosphor using solid state chemical reaction at 1100 °C, as proven by the XRD patterns. The morphology of the composites showed faceted and hexagon particle shapes. The photons with energies corresponding to the NIR emission range were successfully up-converted to photon energies corresponding to the visible emission range, under the excitation of 980 nm laser diode. The possible mechanism of energy transfer was illustrated and discussed. The CIE coordinate plot indicate that the overall displayed emission

resembled a greenish-yellow. Log-log plots of the power dependence of luminescence intensity showed that two photons contributed to the displayed UC luminescence of $\text{ZnTiO}_3\text{-Zn}_2\text{TiO}_4\text{: Er}^{3+}$. These luminescence results suggested that the calculated luminescence lifetimes are similar to the one obtained in chapter 4.

5.5. References

- [1] N. Chanthima and J. Kaewkhao. *Proceedings* **4** (2017) 6099 – 6104.
- [2] Z. He, X.Y. Sun and X. Gu. *Ceram. Int.* **43** (2017) 7378 – 7382.
- [3] X. Li, Y. Yu and Z. Zheng. *Ceram. Int.* **42** (2016) 490 – 494.
- [4] P. Ramasamy, P. Manivasakan and J. Kim. *RSC Adv.* **4** (2014) 34873 – 34895.
- [5] T.A. Mahajan, R.K. Bedi, S. Kumar, V. Saxena and D.K. Aswal. *Chem. Phys. Lett.* **658** (2016) 276 – 281.
- [6] A. Nadort, J. Zhaob and E.M. Goldys. *Nanoscale* **8** (2016) 13099 – 13130.
- [7] T.P. Mokoena, E.C. Linganiso, V. Kumar, H.C. Swart, S.H. Cho and O.M. Ntwaeaborwa. *J. Colloid Interface Sci.* **496** (2017) 87 – 99.
- [8] W. Qi, X. Zhang and H. Wang. *Curr. Opin. Colloid Interface Sci.* **35** (2018) 36 – 41.
- [9] S.Y. Lin, C.Y. Chan, C.W. Tsai, and G.W. Hsieh. *Org. Electron.* **57** (2018) 269 – 276.
- [10] P.K. Baitha and J. Manam. *J. Rare Earths* **33(8)** (2015) 805 – 812.
- [11] L. Mengting and J. Baoxiang. *J. Rare Earths* **33(3)** (2015) 231 – 238.
- [12] M.V. Nikolic, N. Labus and M.M. Ristic. *Ceram. Int.* **35** (2009) 3217 – 3220.
- [13] K. Kobwittaya, Y. Oishi, T. Torikai, M. Yada, T. Watari, and H.N. Luitel, *Ceram. Int.* **43**, (2017) 13505– 13515.
- [14] M.R.D Khaki, M.S. Shafeeyan, A.A.Abdul Raman and W.M.A.W Daud. *J. Mol. Med.* **258** (2018) 354 – 365.
- [15] M. Maghsoodi and Z. Yari. *Iran J. Basic Med. Sci.* **7** (2014) 344 – 350.
- [16] S.J. Mofokeng, V. Kumar, R.E. Kroon and O.M. Ntwaeaborwa. *J. Alloys Compd.* **711** (2017) 121 – 131.
- [17] S. Hraiech, C. Bouzidi and M. Ferid. *Physica B* **522** (2017) 15 – 21.

- [18] B. Afefa, M.M. Alqahtanib, H.H. Hegazy, E. Yousef, K. Damaka, and R. Maaleja. *J. Lumin.* **194** (2018) 706 – 712.
- [19] L.L. Noto, S.S. Pitale, M.A. Gusowki, J.J. Terblans, O.M. Ntwaeaborwa, H.C. Swart. *Powder Technol.* **237** (2013) 141 – 146.
- [20] K.M. Girish, S.C. Prashantha, and H. Nagabhushana. *J. Sci.: Adv. Mater. Devices* **2** (2017) 360 – 370.
- [21] Z. Ali, S. Ali, I. Ahmad, I. Khan and H.A.R. Aliabad. *Physica B* **420** (2013) 54 – 57.
- [22] M. Najafi. *J. Fluoresc.* **26** (2016) 775 – 780.
- [23] Janek, R. Lisiecki, W. Ryba-Romanowski, J. Pisarska and W.A. Pisarski. *Opt. Mater.* **74** (2017) 105 – 108.
- [24] L. Strizik, J. Zhang, T. Wagner, J. Oswald, T. Kohoutek, B.M. Walsh, J. Prikryl, R. Svoboda, C. Liu, B. Frumarova, M. Frumar, M. Pavlista, W.J. Park and J. Heo. *J. Lumin.* **147** (2014) 209 – 215.
- [25] X. Lia, Y. Yua and Z. Zheng. *Ceram. Int.* **42** (2016) 490 – 494.
- [26] Z. He, X.Y. Sun and X. Gu. *Ceram. Int.* **43** (2017) 7378–7382.
- [27] S.I. Riveraa, F.J. Carrilloa, A. Garcíaa and J. Oliva. *Mater. Lett.* **187** (2017) 83 – 85.
- [28] Y.Y. Ge, Y.J. Zhao, X.Y. Yuan, S.Y. Sun, Y.Z. Zhao and H.P. Zhou. *J. Alloys Compd.* **699** (2017) 892 – 897.
- [29] L.V. Maneeshya, P.V. Thomas and K. Joy. *Proceedings* **2** (2015) 992 – 996.
- [30] H. Steinkemper, S. Fischer, M. Hermle and J.C. Goldschmidt. *New J. Phys.* **15** (2013) 1 – 13.
- [31] T.P. Mokoena, E.C. Liganiso, V. Kumar, H.C. *Ceram. Int.* **43** (2017) 174 – 18.
- [32] D.K. Sardar, D.M. Dee, K.L. Nash, R.M. Yow, J.B. Gruber and R. Debnath. *J. Appl. Phys.* **102** (2007) 083105 (1 – 6).
- [33] O.M. Ntwaeaborwa, S.J. Mofokeng, V. Kumar and R.E. Kroon. *Spectrochim. Acta A* **182** (2017) 42 – 49.

Chapter 6: Up-conversion luminescence properties of Er³⁺ doped ZnTiO₃ phosphor

6.1. Introduction

Rare earth ions activated semiconductors have been investigated most frequently due to their unique and stable photoluminescence properties for extending absorption of light range in several applications such as solar cells, volumetric display and bioimaging to mention the few [1, 2]. It has been reported that oxide materials are regarded as the most effective hosts for up-conversion (UC) rare earth ions. Among these oxide materials, ZnO and TiO₂ are one of the feasible UC host materials because they exhibit low phonon energies, low toxicity, better chemical and thermal stability and high melting point [3-6]. Currently, some researchers have been interested in studying the optical properties of UC RE³⁺ doped and co-doped ZnO-TiO₂ system [7, 8]. However, there are three phases originating from ZnO-TiO₂ system, namely: hexagonal ZnTiO₃, cubic Zn₂TiO₂ and Zn₂Ti₃O₈ [9]. ZnTiO₃ is classified as perovskite ABO₃ type semiconductor material and is considered as a high thermal stability host material due to its high energy band gap, electron mobility, low cost and environment friendliness [10, 11].

Erbium (Er³⁺) is an excellent luminescent ion which commonly depend on the host with a low phonon energy to convert the near infra-red region into wide ultraviolet (UV) region and the visible region with high emission intensity [12]. This ion is an interesting ion in the field of luminescence because it consists of several manifolds which give emission lines in blue, green and red regions when excited by a 980 nm diode laser. The intense green emission can be easily achieved in Er³⁺ when incorporated in the system containing ZnO because oxygen vacancies and Zn²⁺ ions simultaneously create the energy levels within the band gap results in intense green emission lines. This emission is induced by the recombination of the Zn²⁺, V_o and the Er³⁺ ions, respectively [13]. This chapter present the ZnTiO₃:Er³⁺ phosphor synthesized by a simple high temperature solid-state reaction technique. The effects of lanthanides molar

concentration on the UC luminescence properties of this phosphor material were investigated and discussed in detail.

6.2. Experimental procedure

ZnTiO₃ phosphor powders with and without up-conversion Er³⁺ ions were synthesized by conventional solid-state reaction method. This synthesis method has advantages such as minimum process time, quick, safe, simple, and uses high purity oxide materials as starting materials. The starting materials were commercial ZnO (99.9%), TiO₂ (99.7%) and Erbium (III) acetate hydrate (99.9%). In a typical preparation, stoichiometric amounts of 1.00 g of ZnO and 0.98 g of TiO₂ were first mixed and ground together in a ball mill for 1 hour at room temperature. The obtained powder and different masses of erbium acetate were mixed together using pestle and mortar. The resulting grey phosphor powders were preheated at 800 °C for 3 hours in air, inside a furnace. The X-ray diffraction (XRD) patterns were obtained using Rigaku Smartlab that was equipped with a monochromatic CuK α ($\lambda = 0.015405$ nm) irradiation source that was operated at 200 mA current. The particle surface morphology and elemental composition were studied by Jeol JSM-7800 field emission scanning electron microscope (FE-SEM) coupled with Oxford Aztec 350 X-Max80 Energy x-ray Dispersive Spectroscopy (EDS). The diffused reflectance studies of the powders were evaluated with Perkin Elmer Lambda 1050 UV-Vis-NIR absorption spectrometer. The photoluminescence (PL) measurements were conducted using an Edinburgh Instruments FLS980 system with a 980 nm (2 W) diode laser as an excitation source for up-conversion luminescence. Up-conversion luminescence was recorded by a Hamamatsu R928P photomultiplier tube, which was operated in photon counting mode after passing through a double emission monochromator. The color coordinates were calculated by Commission Internationale de L'Eclairage (CIE) software (GoCIE) to confirm the color tuning behavior of the emitted light.

6.3. Results and discussion

6.3.1. Structural analysis

The XRD patterns in Fig. 6.1 shows the phase formation of the prepared ZnTiO₃ and ZnTiO₃:xmol%Er³⁺ nanoparticles. The patterns are consistent with the ecandrewsite ZnTiO₃ with space group **R-3 (148)** referenced in the ICSD file number 01-085-0547. These results

suggest that the undoped ZnTiO_3 sample is crystallographically phase pure and does not consist of any impurity or other crystallographic phases. The XRD spectra of the Er^{3+} doped ZnTiO_3 nanoparticles shows the presence of the secondary phases (denoted by asterisks*) of Er_2O_3 (ICSD file no. 01-076-0159).

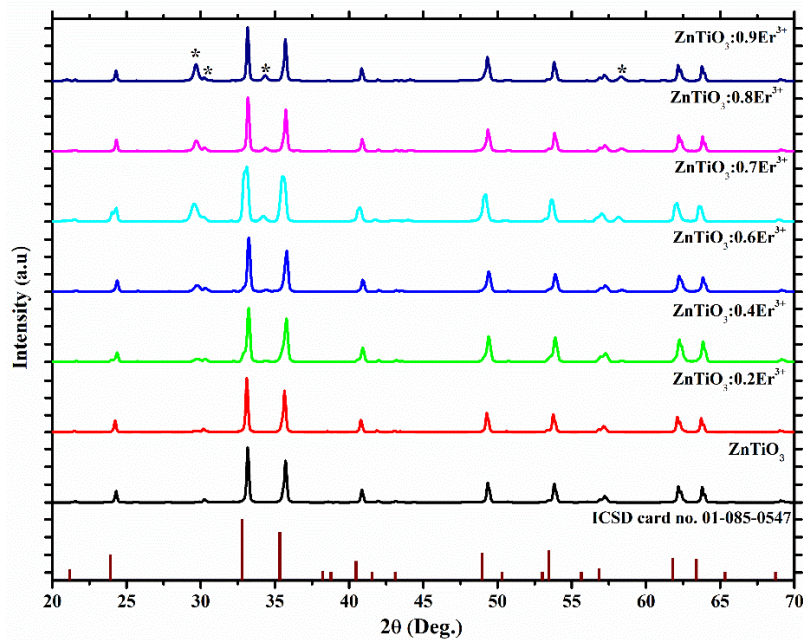


Figure 6.1: X-ray Diffraction patterns of ZnTiO_3 and $\text{ZnTiO}_3:\text{Er}^{3+}$ annealed at 800 °C.

6.3.2. Morphological analysis

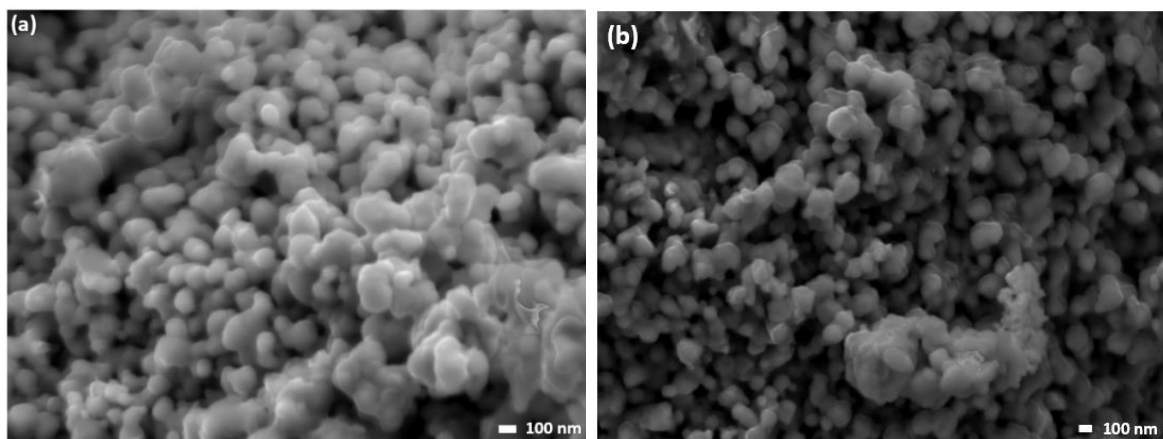


Figure 6.2: FE-SEM images of ZnTiO_3 and $\text{ZnTiO}_3:0.8\text{mol\%Er}^{3+}$ powders.

The morphologies of the synthesized ZnTiO_3 and $\text{ZnTiO}_3:\text{Er}^{3+}$ samples which are shown in Fig. 6.2 were investigated through scanning electron microscope (SEM). The images show that

the prepared samples consisted of agglomerated and uniform particle shapes. The observed agglomerated morphology is due to annealing of the samples at high temperature [14]. However, the SEM results shows that incorporation of Er^{3+} ions did not affect the surface morphology of ZnTiO_3 .

6.3.3. UV-Vis-NIR analysis

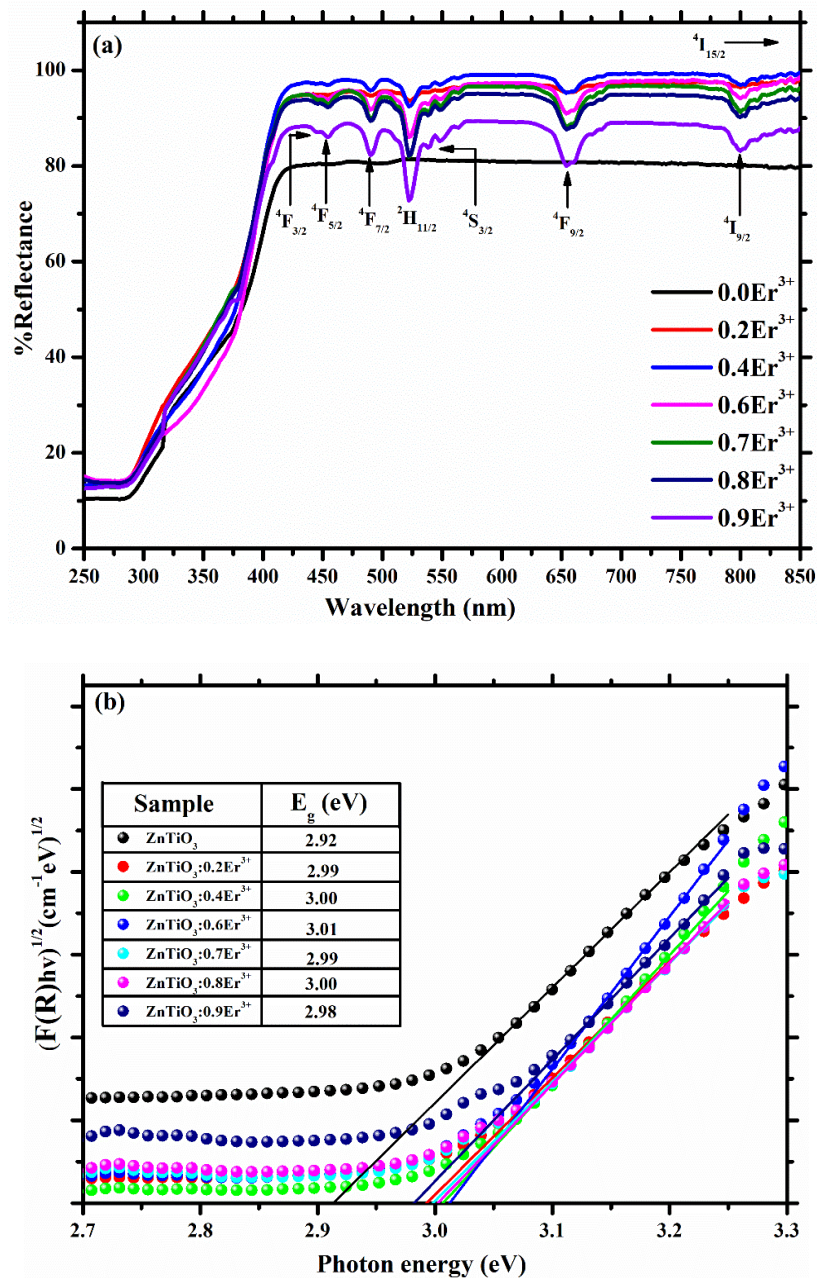


Figure 6.3: The diffuse reflectance spectra (a) and Kubelka Munk's plots (b) of ZnTiO_3 and $\text{ZnTiO}_3:\text{xmol}\%\text{Er}^{3+}$ phosphor.

To investigate the optical responses of the synthesized phosphors, the diffuse reflectance spectra of the ZnTiO_3 with different Er^{3+} content are shown in Fig. 6.3. The absorption band edge for the ZnTiO_3 phosphor is found at approximately below 420 nm, due to electronic transition between valence and conduction bands of the ZnTiO_3 [15, 16]. There are several absorption bands observed in the 430-850 nm spectral region that are assigned to characteristics of f-f transitions of Er^{3+} ions in ZnTiO_3 , respectively [17, 18]. Through the reflectance spectra shown in Fig. 6.3 (a), certain wavelength range of the incident light (< 420 nm) can be absorbed by ZnTiO_3 while $\text{ZnTiO}_3:\text{Er}^{3+}$ can absorb the incident light in spectral region 250 - 850 nm, respectively. Kubelka-Munk function was employed from the DRS to extract the band gap energy of ZnTiO_3 phosphor. Kubelka-Munk function is presented in the Fig. 6.3 (b) and shows the dependence of $(F(R) \times hv)^{1/2}$ vs hv (photon energy) where R is the diffused reflectance, $F(R)$ is the remission function defined as $F(R) = (1-R)^2/(2R)$, h is the Planck's constant and ν is the radiation frequency [19]. Extrapolation of the linear region or point of inflection gives the band gap value of the materials on the energy axis. The estimated optical band gap value for ZnTiO_3 is 2.92 eV, which increase progressively up to 3.01 eV for Er^{3+} doped samples. This could be the fact that the unoccupied lowest states in the conduction band of ZnTiO_3 are filled due to excessive doping thereby tuning the band gap energy [20, 21].

6.3.4. Up-conversion luminescence analysis

The UC spectra of $\text{ZnTiO}_3:\text{Er}^{3+}$ samples were measured under 980 nm, using a continuous laser diode. As shown in Fig. 6.4 (a), the UC emission spectra show green emission lines centred at ~527 nm, ~545 nm and red emission line centred at ~665 nm. The UC emissions lines correspond to the ${}^2\text{H}_{11/2} \rightarrow {}^4\text{I}_{15/2}$, ${}^4\text{S}_{3/2} \rightarrow {}^4\text{I}_{15/2}$ and ${}^4\text{F}_{9/2} \rightarrow {}^4\text{I}_{15/2}$ intrinsic electronic transitions of Er^{3+} ions, respectively [22 - 24]. The splitting observed from ${}^2\text{H}_{11/2}$ transition in green emission line is due to splitting sublevel manifolds induced by spin-orbit coupling and breakdown of the degeneracy of the electronic interaction [22]. The UC intensity was first increased and then decreased after reaching the maximum intensity due to the concentration quenching. The optimum concentration for Er^{3+} showing the strongest UC emission intensity were found to be 0.8 mol% as shown in Fig. 6.4 (a). Fig. 6.4(b) demonstrate the integrated green to red intensity ratios varied from 1.76 to 2.67 for the variation in Er^{3+} ions, respectively. However, the emission intensity ratio of green to red emission changed and doping concentration did not influence the position of the emission bands. The Commission

Internationale de l'Eclairage (CIE) colour coordinates of Er^{3+} emissions have been calculated by using the GoCIE software to study their photometric characteristics. Fig.6.5 shows the CIE diagrams of the emission of $\text{ZnTiO}_3: x\text{mol}\%\text{Er}^{3+}$ phosphors obtained under the 980 nm laser excitation. From the figure, it has been observed that the colour co-ordinate of phosphor manifest green colour. The calculated CIE coordinates are given in Table 6.1.

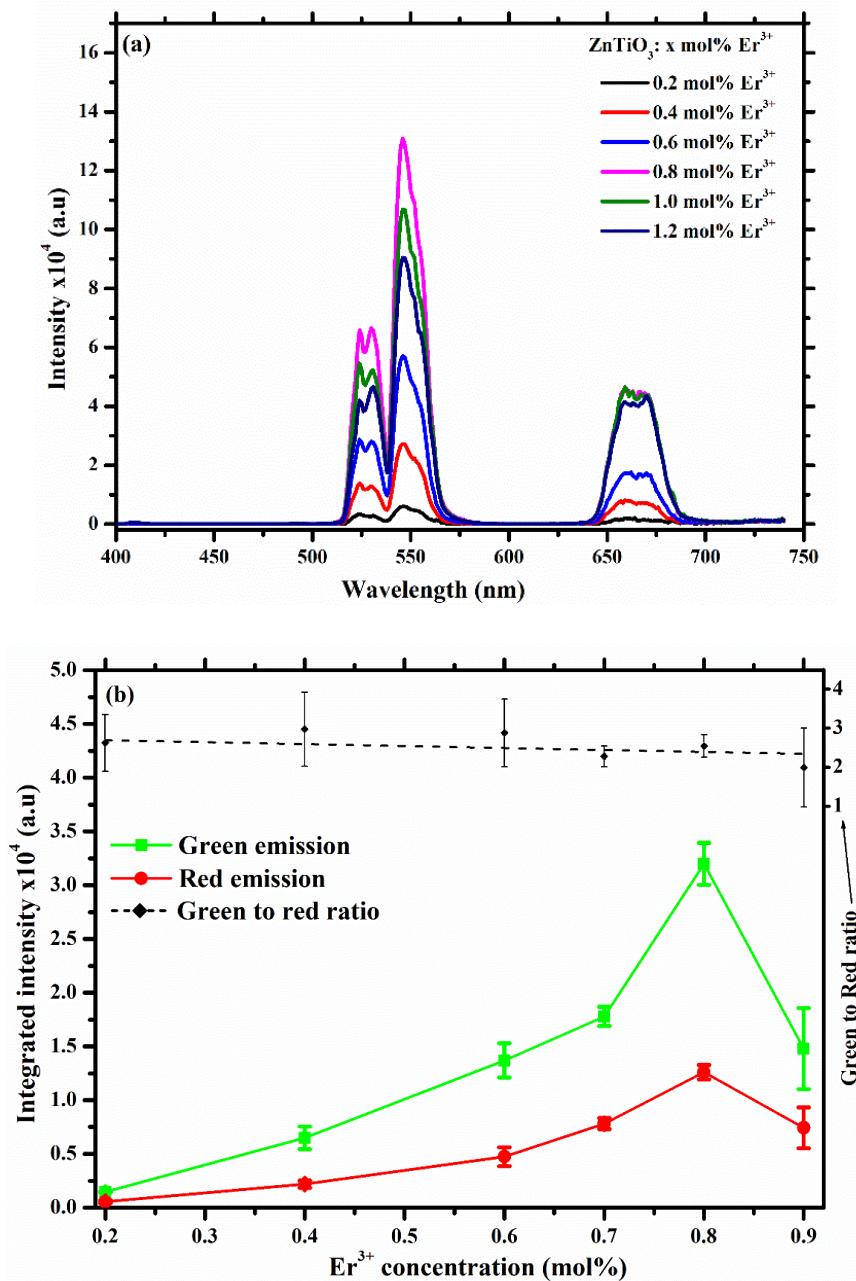


Figure 6.4: Up-conversion emission spectra of (a) $\text{ZnTiO}_3: x\text{mol}\%\text{Er}^{3+}$ phosphor under 980 nm excitation wavelength and (b) comparison of integrated intensities of green and red emissions for the phosphors.

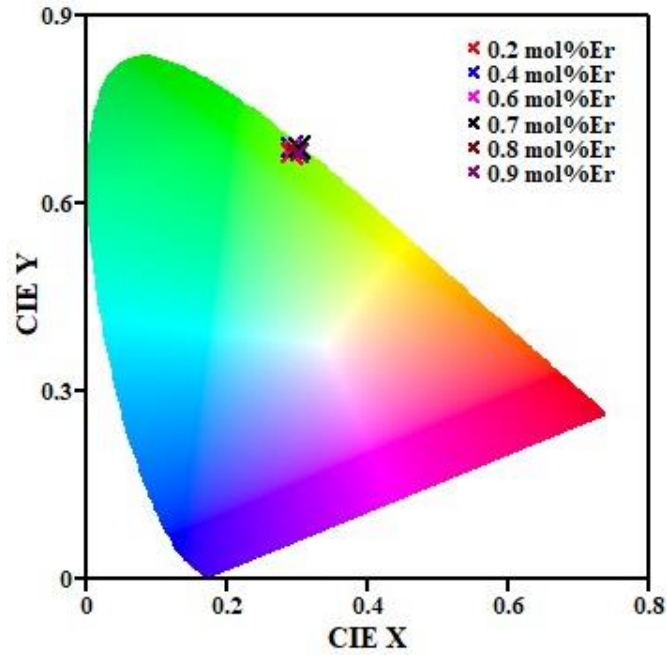


Figure 6.5: The CIE colour chromaticity diagram of $\text{ZnTiO}_3:\text{xmol\%Er}^{3+}$ phosphors.

Table 6.1: Representation of the concentration and calculated Commission Internationale de l'Eclairage (CIE) coordinates of $\text{ZnTiO}_3:\text{xmol\%Er}^{3+}$.

Er^{3+} concentration	X	Y
0.2	0.29	0.68
0.4	0.29	0.69
0.6	0.29	0.69
0.7	0.30	0.69
0.8	0.29	0.69
0.9	0.30	0.68

Fig. 6 (a) demonstrate the typical up-conversion emission spectra with variation of laser power for both green and red emission. The variation in laser power enhanced up-conversion emission bands but did not change their overall shape of emissions as shown in the figure, which suggests that the samples exhibit excellent stability under laser excitation energy [22]. The power dependent spectra to analyse the physical mechanism of the UC process involved in the Er^{3+} doped ZnTiO_3 phosphors under 980 nm laser excitation is presented in Fig. 6.6 (b). According to the relation $f(P) = AP^n$ where $f(P)$ is the UC emission intensity, A is a constant, P is the

excitation power, and n (slope of logarithm curve) is the number of pumping photons required for the transition from ground state to luminescence emitting excited state [25]. Generally, the intensity of UC emission varies with the excitation power. As demonstrated in the Fig. 6.6(b), the observed slope values of the linear fitting for green and red emissions are 1.75, 1.68 and 1.62. At least two-photon process is involved for both green and red UC luminescence in the prepared phosphor, suggesting considerable contribution for a two-photon process in the population of the green and red emitting states.

The process of up-conversion mechanism in $\text{ZnTiO}_3:\text{Er}^{3+}$ phosphor can be interpreted by the energy level diagram in Fig. 6.7 to better understand the possible up-conversion mechanisms of green and red emission lines in the prepared phosphor. The schematic diagram illustrates the probable excitation pathways populating different UC emission states through possible energy transfer processes. Ground state absorption (GSA) is the first transition of Er^{3+} ions whereby 980 nm excitation is absorbed by this GSA and populate the excited metastable level (lower energy level of ESA) [22, 26]. As shown in Fig. 6.7, Er^{3+} ions are excited from its fundamental $^4\text{I}_{15/2}$ energy level and populate $^4\text{I}_{11/2}$ energy level through GSA. The process of energy transition after GSA is the excited state absorption (ESA) of Er^{3+} ions by populating $^4\text{I}_{9/2}$ and $^2\text{F}_{7/2}$ energy levels. Due to lack of stability of ions populated the $^4\text{F}_{7/2}$ level of Er^{3+} , some of the ions depopulate to excited metastable $^2\text{H}_{11/2}$, $^4\text{S}_{3/2}$, and $^4\text{F}_{9/2}$ levels through non-radiative transition [28]. In addition, Er^{3+} ions in $^2\text{F}_{7/2}$ energy level are transferred non-radiatively to $^4\text{F}_{9/2}$ energy level through a process called cross-relaxation (CR) energy transfer given by $^4\text{F}_{7/2} \rightarrow ^4\text{F}_{9/2}$ and $^4\text{F}_{9/2} \leftarrow ^4\text{I}_{11/2}$ [26-28]. Finally, ions in the metastable levels of Er^{3+} relaxes to the ground state in the form of up-converted green and red luminescence due to $^4\text{S}_{3/2} \rightarrow ^4\text{I}_{15/2}$ and $\text{F}_{9/2} \rightarrow ^4\text{I}_{15/2}$ transitions at 545 and 665 nm.

On the other hand, there is a green emission raising due to $^2\text{H}_{11/2} \rightarrow ^4\text{I}_{15/2}$ transition at 527 nm as shown in (II) from Fig. 6.7. In this case, populating the $^2\text{H}_{11/2}$ energy level with ions is influenced by CR energy transfer process between Er^{3+} - Er^{3+} ions in the crystal field. The transitions taking place during CR energy transfer is given by $^4\text{I}_{11/2} + ^4\text{I}_{11/2} \rightarrow ^4\text{F}_{7/2} + ^4\text{I}_{15/2}$ [29]. Ions populated $^4\text{F}_{7/2}$ energy level through CR decay non-radiatively to $^2\text{H}_{11/2}$ energy level of Er^{3+} , following a radiative decay to $^4\text{I}_{15/2}$ ground level in the form of green UC emission. The two transitions, $^2\text{H}_{11/2}$ (I) and $^2\text{H}_{11/2}$ (II) of the UC green emission in this case shows the Stark splitting of the $^2\text{H}_{11/2}$ energy level of Er^{3+} ions in the crystal field.

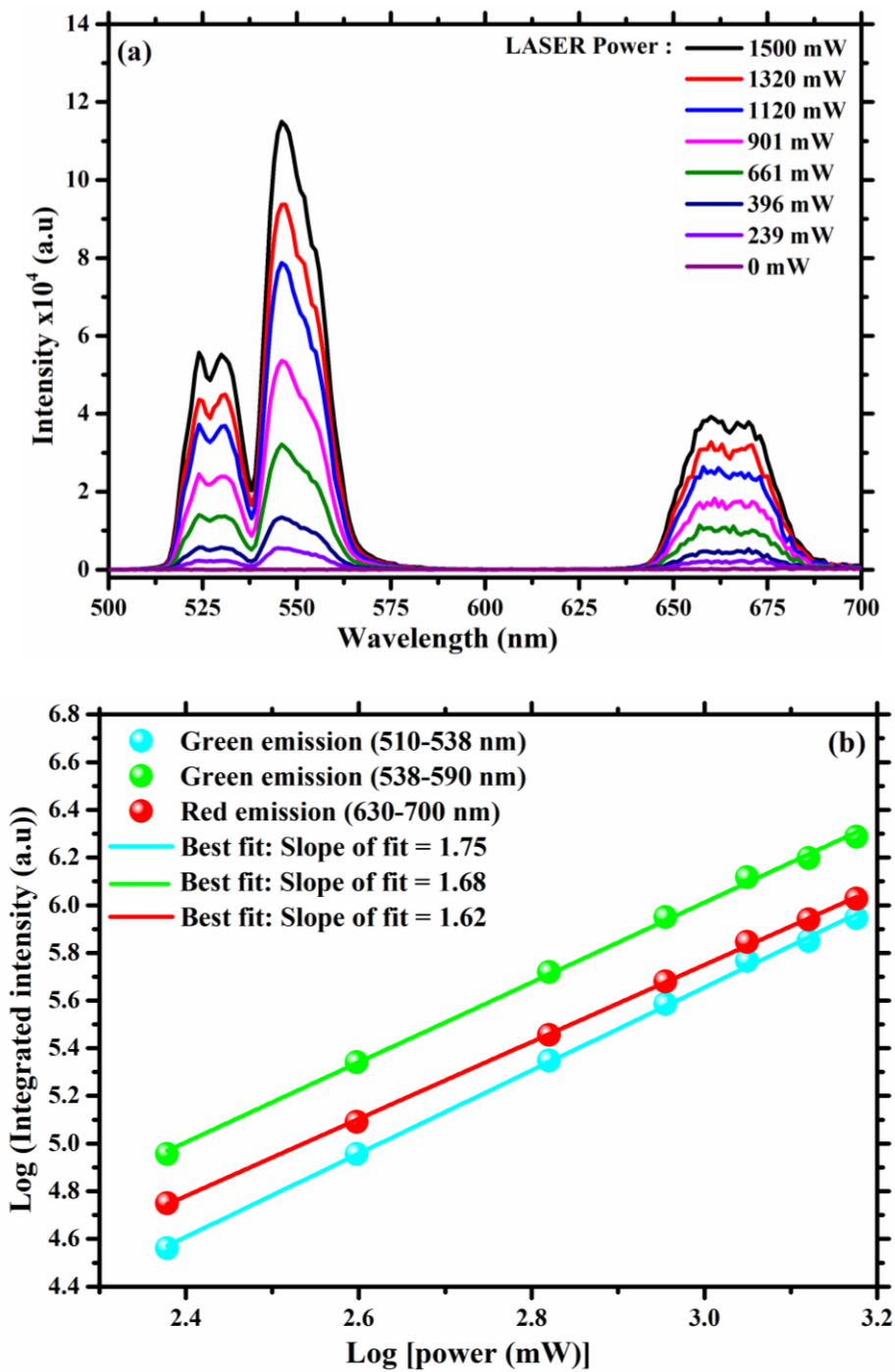


Figure 6.6: (a) Up-conversion emission spectra of ZnTiO₃:0.8mol%Er³⁺ phosphor under 980 nm excitation wavelength within a laser power range of 0 mW to 2563 mW and (b) logarithmic dependence of UC emission intensity as a function of logarithm of power of ZnTiO₃:0.8mol%Er³⁺ phosphor.

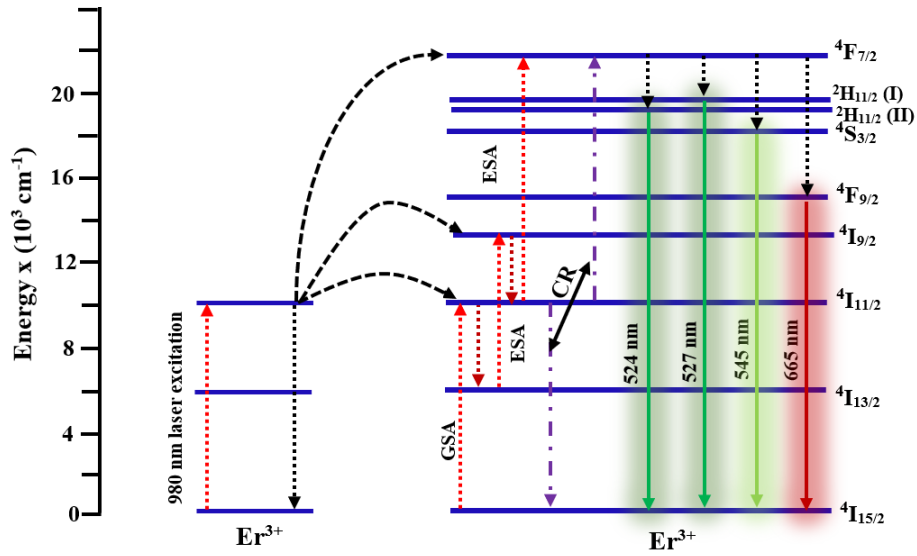


Figure 6.7: Schematic energy level diagram of Er^{3+} showing the possible energy transfer mechanism involved in UC process under an excitation of 980 nm.

The luminescence decay measurements were performed at 545 nm transition with variable Er^{3+} contents as shown in Fig. 6.8 (a). The decay curves were well fitted with the triple exponential function given by the following equation:

$$I(t) = I_0 + A_1 e^{-t/\tau_1} + A_2 e^{-t/\tau_2} + A_3 e^{-t/\tau_3} \quad [6.1]$$

where I and I_0 are the luminescence intensity at certain time t and 0 (from background), respectively, t is the time, A_1 , A_2 and A_3 are the fitting parameters, τ_1 , τ_2 and τ_3 are the slow and fast decay components (long and short lifetimes). The mean lifetimes (τ) was be calculated by the following equation:

$$\tau = \frac{A_1 \tau_1^2 + A_2 \tau_2^2 + A_3 \tau_3^2}{A_1 \tau_1 + A_2 \tau_2 + A_3 \tau_3} \quad [6.2]$$

The calculated mean lifetimes of the ${}^4\text{S}_{3/2} \rightarrow {}^4\text{I}_{15/2}$ transition as a function of Er^{3+} concertation are shown in table (see the inset) in Fig. 6.8 (b). The mean lifetimes decreased significantly with the increase of Er^{3+} concentration. According to Hraiech *et al.*, the decrease in mean lifetimes of Er^{3+} ions might be due to energy migration between the neighbourhood Er^{3+} ions and the energy transfer from Er^{3+} ions the defects of ZnTiO_3 [30].

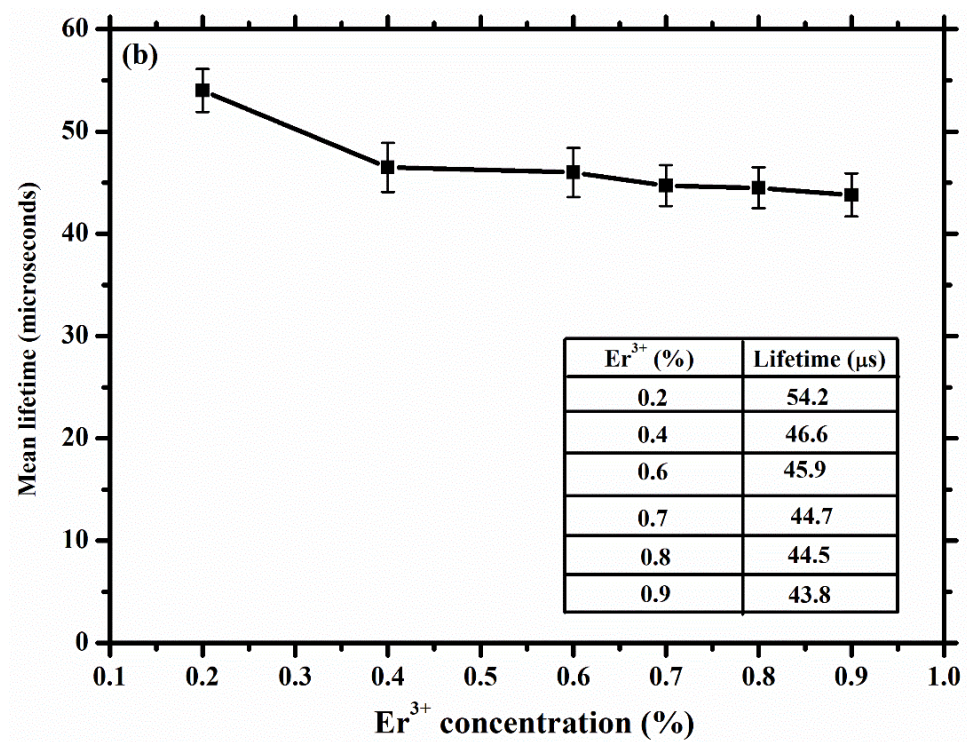
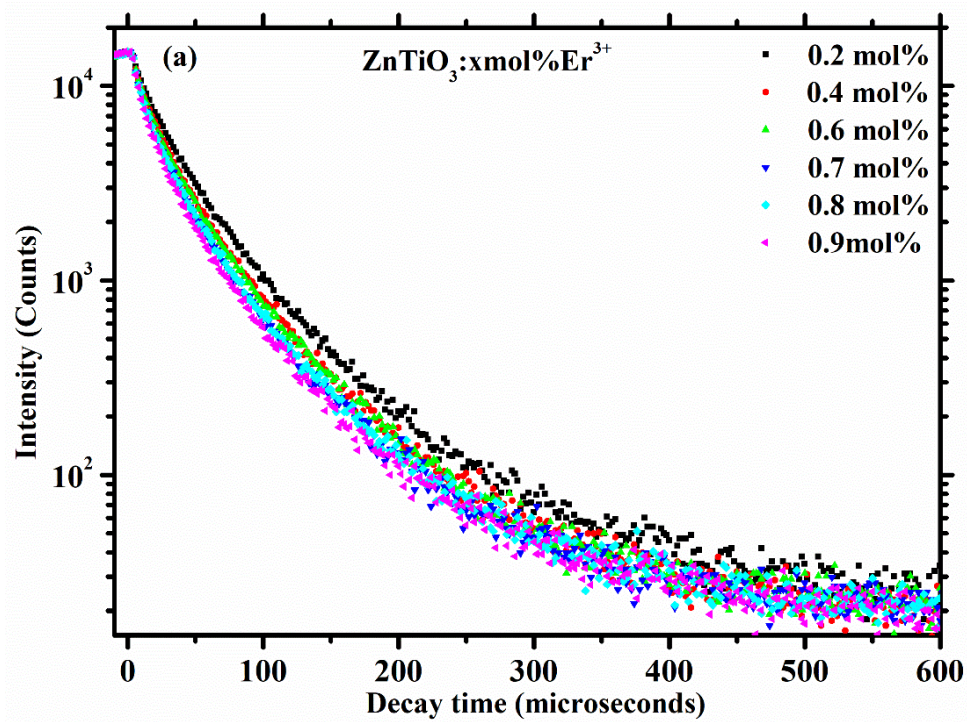


Figure 6.8: (a) Luminescence decay curves of the $^4S_{3/2} \rightarrow ^4I_{15/2}$ transition in $ZnTiO_3:Er^{3+}$ phosphor and (b) the mean lifetime as a function of Er^{3+} concentrations.

6.4. Conclusion

The eandrewsite $\text{ZnTiO}_3:\text{Er}^{3+}$ up-converting phosphors have been successfully synthesized through standard solid-state technique. XRD patterns confirm that the phosphor crystallized in the eandrewsite ZnTiO_3 with space group $R-3 (148)$. The morphology of the phosphors showed faceted and hexagon particle shapes. The sample containing 0.8% Er^{3+} exhibits the optimal UC luminescence intensity. The observed optical band gap energy of ZnTiO_3 calculated from the ultraviolet absorption edge was increased due to Er^{3+} ion doping concentration. The UC properties have been comprehensively investigated and the significant enhancement for UC emission intensity of Er^{3+} have been observed. The observation of the nature of the energy transfer mechanism suggested that the cross-relaxation process was the preferred energy transfer between Er^{3+} ions. The decrease in mean lifetimes with an increase in Er^{3+} concentration is a result of enhanced energy transfer between Er^{3+} ions. With these experimental properties, $\text{ZnTiO}_3:\text{Er}^{3+}$ appear as suitable phosphor in NIR to visible up-converter and offer prospects for power conversion efficiency solar cells applications.

6.5. References

- [1] H. Zhang, Q. Zhang, Y. Lv, C. Yang, H. Chen and X. Zhou. *Mater. Res. Bull.* **106** (2018) 346 – 352.
- [2] B.T. Huy, Z. Gerelkhuu, T.L. Phan, N. Tran and Y.I. Lee. *J. Rare Earths* **37** (2019) 345 – 349.
- [3] V. Kumar, A. Pandey, S.K. Swami, O.M. Ntwaeaborwa, H.C. Swart, and V. Dutta. *J. Alloys Compd.* **766** (2018) 429 – 435.
- [4] R. Das, P. Phadke, N. Khichar and S. Chawla. *Superlattices Microstruct.* **83** (2015) 642 – 650.
- [5] W. Liua, H. Zhang, H. Wang, M. Zhanga, M. Guo. *Appl. Surf. Sci.* **422** (2017) 304 – 315.
- [6] H.N. Luitel, K. Ikeue, R. Okuda, R. Chand, T. Torikai, M. Yada and T. Watari. *Opt. Mater.* **36** (2014) 591 – 595.
- [7] K. Kobwittaya, Y. Oishi, T. Torikai, M. Yada, T. Watari, and H.N. Luitel. *Vacuum* **148** (2018) 286 – 295.
- [8] K. Kobwittaya, Y. Oishia, T. Torikai, M. Yada, T. Wataria, and H.N. Luitel. *Ceram. Int.* **43** (2017) 13505 – 13515.
- [9] E. Li, P. Zhang, S. Duan, J. Wang, Y. Yuan, B. Tang. *J. Alloys Compd.* **647** (2015) 866 – 872.
- [10] J. Yu, D. Li, L. Zhu and X. Xu. *J. Alloys Compd.* **681** (2016) 88 – 95.
- [11] T. Surendar, S. Kumar and V. Shanker. *PCCP* **16** (2014) 728 – 735.
- [12] L. Zhang, Q. Zhu, Y. Jiang, Z. Wang, X. Yuan, H. Lib, H. Chang, Sujie Cui, Lin Wang and L. Zhang. *Ceram. Int.* **45** (2019) 4431– 4436.
- [13] P. Sudhakar, A.S.S. Reddy, Y. Zhydachevskyy, A. Suchocki, M.G. Brik, V.R. Kumar, M. Piaseckig and N. Veeraiah. *Opt. Mater.* **86** (2018) 87 – 94.
- [14] S.W. Oh, H.J. Bang, Y.C. Bae and Y.K. Sun. *J. Power Sources* **173** (2007) 502–509.
- [15] B. Ozturk and G.S.P. Soyulu. *Ceram. Int.* **42** (2016) 11184 – 11192.

- [16] R.S. Raveendra, P.A. Prashanth, R.H. Krishna, N.P. Bhagya, B.M. Nagabhushana, H.R. Naika, K. Lingaraju, H. Nagabhushana and B.D. Prasad. *J. Asian Ceram. Soc.* **2** (2014) 357 – 365.
- [17] F. Chen, T. Wei, X. Jing, Y. Tian, J. Zhang and S. Xu. *Sci. Rep.* **5** (2015) 10676 (1 – 3).
- [18] V. Singh, P. Haritha, V. Venkatramu and S.H. Kim. *Spectrochim. Acta, Part A* **126** (2014) 306 – 311.
- [19] K.M. Girish, S.C. Prashantha, and H. Nagabhushana. *J. Sci.: Adv. Mater. Devices* **2** (2017) 360 – 370.
- [20] H. Eskandarloo, A. Badiei, M.A. Behnajady, A. Tavakoli and G.M. Ziarani. *Ultrason. Sonochem.* **29** (2016) 258 – 269.
- [21] K. Joshi, M. Rawat, S.K. Gautam, R.G. Singh, R.C. Ramola and F. Singh. *J. Alloys Compd.* **680** (2016) 252 – 258.
- [22] B.P. Kore, A. Kumar, L. Erasmus, R.E. Kroon, J.J. Terblans, S.J. Dhoble and H.C. Swart. *Inorg. Chem.* **57** (2018) 288 – 299.
- [23] J. Janek, R. Lisiecki, W. Ryba-Romanowski, J. Pisarska and W.A. Pisarski. *Opt. Mater.* **74** (2017) 105 – 108.
- [24] I. Soltani, S. Hraiech, K. Horchani-Naifer and M. Ferid. *Opt. Mater.* **77** (2018) 161 – 169.
- [25] J. Grube and G. Krieke. *J. Lumin.* **203** (2018) 376 – 384.
- [26] S. Liu, S. Liu, M. Zhou, X. Ye, D. Hou and W. You. *RSC Adv.* **7** (2017) 36935 – 36948.
- [27] Y. Ma, G. Xiang, J. Zhang, Z. Liu, P. Zhou, W. Liu, X. Tang, S. Jiang, X. Zhou, L. Li, Y. Luo and Y. Jin. *J. Alloys Compd.* **769** (2018) 325 – 331.
- [28] X. Cheng, X. Ma, H. Zhang, Y. Ren, and K. Zhu. *Physica B* **521** (2017) 270 – 274.
- [29] D.H. Kim, J.H. Ryu, J.H. Chung, K.B. Shim, and S.Y. Cho. *J. Electrochem. Soc.* **158** (11) (2011) J345 – J348.
- [30] S. Hraiech, C. Bouzidi and M. Ferid. *Physica B* **522** (2017) 15 – 21.

Chapter 7: Up-conversion luminescence properties and energy transfer mechanism of $\text{ZnTiO}_3: \text{Er}^{3+}, \text{Yb}^{3+}$ phosphor.

7.1. Introduction

Rare earth (RE) ion doped semiconductors are operative materials for a diverse range of applications in various fields of research, photocatalytic treatment, environmental purification and development of technologies [1-3]. Importantly, up-converting (UC) RE doped semiconductor materials have attracted enormous attention as photocatalysts for numerous applications [3, 4]. Oxide materials are reported as the most effective hosts for UC RE ions. Among these, ZnO and TiO_2 are considered most suitable because they exhibit low phonon energies and better chemical and thermal stability [5-8]. Recent studies have demonstrated an interest in the optical properties of the UC RE ion doped and co-doped ZnO- TiO_3 system [9,10]. In the present work the effectiveness of the ZnTiO_3 ternary oxide host for RE dopant ions is evaluated for UC photoluminescence.

There are several different phases that can be prepared from the ZnO- TiO_2 system, that also consist of several different polymorphs. These phases include ZnTiO_3 , Zn_2TiO_2 and $\text{Zn}_2\text{Ti}_3\text{O}_8$, just to mention a few [11]. ZnTiO_3 resembles an ABO_3 perovskite structure and has high thermal and chemical stability. It has a wide energy band gap, high electron mobility as well as being cost-effective and environmentally friendly [12, 13]. The compound is mostly used as a photocatalyst, microwave dielectric resonator and gas sensors for the detection of carbon monoxide and nitric oxide. When doped with a suitable activator ion, its catalytic and electronic properties can be tuned to expand its possible applications [14, 15]. Incorporation of RE ions introduces metastates which display luminescence [16]. ZnTiO_3 materials have been synthesized using several approaches, which include the solid-state reaction method, the hydrothermal method, the sol-gel method and solution combustion synthesis, just to mention a few [17, 18]. In this study the solid-state reaction was used to prepare ZnTiO_3 due to its

advantages such as controllable crystal growth, energy efficiency, short firing time [19] and ease of incorporation rare-earths dopant ions.

Currently, electrification of remote areas in many developing countries is still a challenge [20]. To address this, alternative forms of energy such as renewable energy are being explored, which do not need to be integrated into the electric grids. Solar and wind energy are common alternatives, which are effective and efficient renewable energy sources [21]. The solar energy is the more explored of the two, because of cost-effectiveness. Even though power conversion efficiency of conventional crystalline silicon solar cells devices is still relatively low to compete with nuclear and fossil fuel sources of energy, they are currently in the commercial market. Their utilization of the solar radiation has limitations because they can only absorb within the narrow range of the electromagnetic wave spectrum of the sun. They also have limited photo-carrier for trapping and recombination and limited electron injection from the excited state into the semiconductor surface [22-24]. The limited absorption can be improved by incorporating materials with a wider absorption range that will absorb the solar energy and convert it to radiation that is absorbable by the photovoltaic cells. Such materials include down-converting (DC) and up-converting (UC) layers of phosphors [22].

The RE doped phosphors have been studied for use in various applications, which include the up-conversion of near-infrared (NIR) photons into ultraviolet or visible photons. This is due to their rich energy level structures, tuneable wavelengths, high photostability, sharp band widths, long emission lifetimes and relatively low toxicity [25]. Among the UC RE ions, erbium (Er^{3+}) ions are commonly used due to their rich energy level structures with several metastable energy levels and long lifetimes. Ytterbium (Yb^{3+}) ions are suitable UC sensitizers because they enhance the luminescence of UC activator ions, due to their large absorption cross section in the NIR region and their high efficiency in transferring energy to activators [25-28]. Co-doping of Er^{3+} ions with Yb^{3+} ions has been a hot topic of research in the past several decades to achieve the most efficient up-converted emission. The UC emission properties for $\text{Er}^{3+}/\text{Yb}^{3+}$ group can be achieved through effective energy transfer (ET), excitation modulation and cross relaxation energy transfer [29-31].

In the present research, we prepared $\text{ZnTiO}_3:\text{Er}^{3+},\text{Yb}^{3+}$ for the first time via a simple high temperature solid-state reaction technique. The effects of lanthanides molar concentration on the UC luminescence properties of this phosphor material were investigated and discussed in

detail. Most importantly, the prepared phosphor displays an efficient UC luminescence, which makes it potentially useful for photovoltaic solar cells.

7.2. Experimental procedure

The undoped ZnTiO₃ powders were synthesized by the conventional solid-state reaction method. The starting materials were commercial ZnO (99.9%), TiO₂ (99.7%), Erbium (III) acetate hydrate (99.9%) and Ytterbium (III) acetate hydrate (99.9%). In a typical preparation, stoichiometric amounts of ZnO (1.00 g) and TiO₂ (0.98 g) were first mixed and ground together in a ball mill for 1 hour at room temperature. Different masses of erbium acetate were incorporated into the ball milled powder and mixed using a pestle and mortar. The same procedure was followed for ytterbium co-doping using different masses. The resulting grey powders were annealed at 800 °C for 3 h in air. The crystalline structure of the prepared samples was examined using an X-ray diffractometer (Rigaku Smartlab) that was equipped with a monochromatic Cu K α ($\lambda = 0.15405$ nm) irradiation source that was operated at 200 mA current and 45 kV. The particle surface morphology and elemental composition were studied with a Jeol JSM-7800 field emission scanning electron microscope (FE-SEM) coupled with an Energy Dispersive Spectrometer (EDS). The diffuse reflectance spectra were recorded with the Perkin Elmer Lambda 1050 UV-Vis-NIR absorption spectrometer. The photoluminescence (PL) measurements were conducted using an Edinburgh Instruments FLS980 system with a 980 nm laser diode as excitation source for up-conversion luminescence.

7.3. Results and discussion

7.3.1. Structural analysis

The XRD patterns in Fig. 7.1 show the phase formation of the zinc titanate samples. These are the patterns of undoped ZnTiO₃, together with luminescence intensity optimized ZnTiO₃:0.8mol%Er³⁺ and ZnTiO₃:0.8mol%Er³⁺,0.7mol%Yb³⁺ phosphors. The XRD patterns of undoped ZnTiO₃ and ZnTiO₃:0.8mol%Er³⁺ were reported in detail in chapter 6. These results show that the undoped ZnTiO₃ sample is a single phase and does not contain any impurities or other crystallographic phases. The XRD patterns show that the optimized Er³⁺ doped ZnTiO₃ phosphor shows the presence of a secondary phase (peaks marked by an asterisk *) corresponding to Er₂O₃ (ICSD file no. 01-076-0159) and ZnTiO₃:0.8Er³⁺,0.7Yb³⁺ also revealed

the presence of Yb_2O_3 (ICSD file no. 01-075-6635). It is known that the ionic radius of Zn^{2+} (0.74\AA) is bigger than Ti^{4+} (0.66\AA). However, the formation of erbium oxide, ytterbium oxide and ytterbium zinc due to doping can be explained by Er^{3+} and Yb^{3+} ions occupying the Zn^{2+} sites, and this may probably limit the crystallite growth [2, 29].

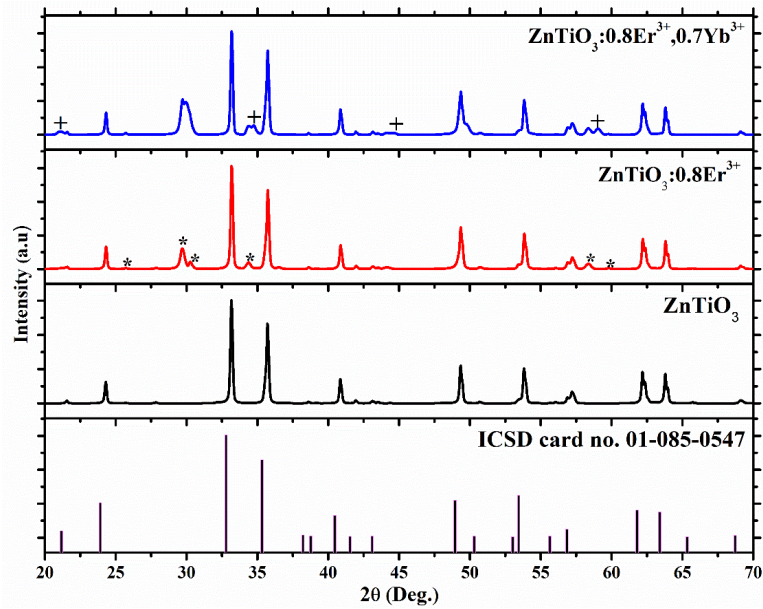


Figure 7.1: X-ray diffraction patterns of $\text{ZnTiO}_3:\text{Er}^{3+}, \text{Yb}^{3+}$ phosphors.

7.3.2. Morphological analysis

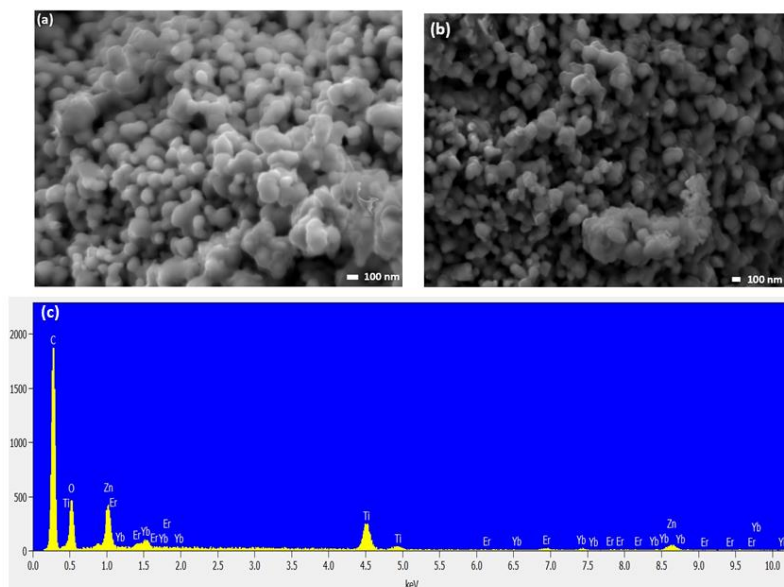


Figure 7.2: FE-SEM micrographs of (a) ZnTiO_3 , (b) $\text{ZnTiO}_3:0.8\text{Er}^{3+}, 0.7\text{Yb}^{3+}$ and (c) EDS spectra of $\text{ZnTiO}_3:0.8\text{Er}^{3+}, 0.7\text{Yb}^{3+}$ phosphors.

The SEM observations was carried out to study the particle morphology of the prepared samples. Fig. 7.2 shows the SEM images and EDS spectra of the $\text{ZnTiO}_3:\text{Er}^{3+}, \text{Yb}^{3+}$ phosphors. The images show that the prepared samples consisted of agglomerated and uniform particle shapes. The observed agglomerated morphology is due to annealing the samples at high temperature [32]. However, the SEM results shows that incorporation of Er^{3+} and Yb^{3+} ions did not affect the surface morphology of ZnTiO_3 . The EDS spectra show the presence of all elements in $\text{ZnTiO}_3:\text{Er}^{3+}, \text{Yb}^{3+}$, respectively.

7.3.3. UV-Vis-NIR analysis

UV-Vis-NIR absorption spectroscopy was used to probe the absorption characteristics of the phosphor samples. Fig. 7.3 (a) displays the UV-Visible diffuse reflectance spectra (UV-Vis DRS) collected in the 200 - 850 nm region. The spectra show the absorption edge lower than 420 nm, which is attributed to electronic transition between valence and conduction bands of ZnTiO_3 [18, 33]. In addition, the spectra show a blue shifted absorption edge due to Er^{3+} doping and $\text{Er}^{3+}/\text{Yb}^{3+}$ co-doping in ZnTiO_3 . Several absorption bands observed in the 430 – 850 nm spectral region are assigned to characteristic $4f - 4f$ transitions of Er^{3+} ions in zinc titanate [14, 34]. The inset in Fig. 7.3 (a) shows a broad absorption cross section in the NIR spectral region. These bands correspond to the overlapping transitions of Er^{3+} ($^4\text{I}_{15/2} \rightarrow ^4\text{I}_{11/2}$) and Yb^{3+} ($^2\text{F}_{7/2} \rightarrow ^2\text{F}_{5/2}$) ions. The results indicate that the prepared samples can absorb more NIR photons due to the observed high absorption cross section in the NIR region. The Kubelka-Munk transformation

$$F(R) = (1-R)^2/(2R) \quad [7.1]$$

was used to determine the band gap energy of the ZnTiO_3 phosphors from the reflectance data R . Fig. 7.3 (b) shows a plot of $(F(R) \times hv)^{1/2}$ as a function of the photon energy hv , where h is Planck's constant and ν is the radiation frequency [35]. Extrapolation of the linear region or point of inflection gives the band gap value of the materials on the energy axis. The estimated optical band gap value for undoped ZnTiO_3 was determined as 2.92 eV, which increased to 3.01 eV and 3.03 eV for Er^{3+} doped and $\text{Er}^{3+}/\text{Yb}^{3+}$ co-doped samples. This could be because of the unoccupied lowest states in the conduction band of ZnTiO_3 , which are filled by excessive doping, thereby tuning the band gap [36, 37].

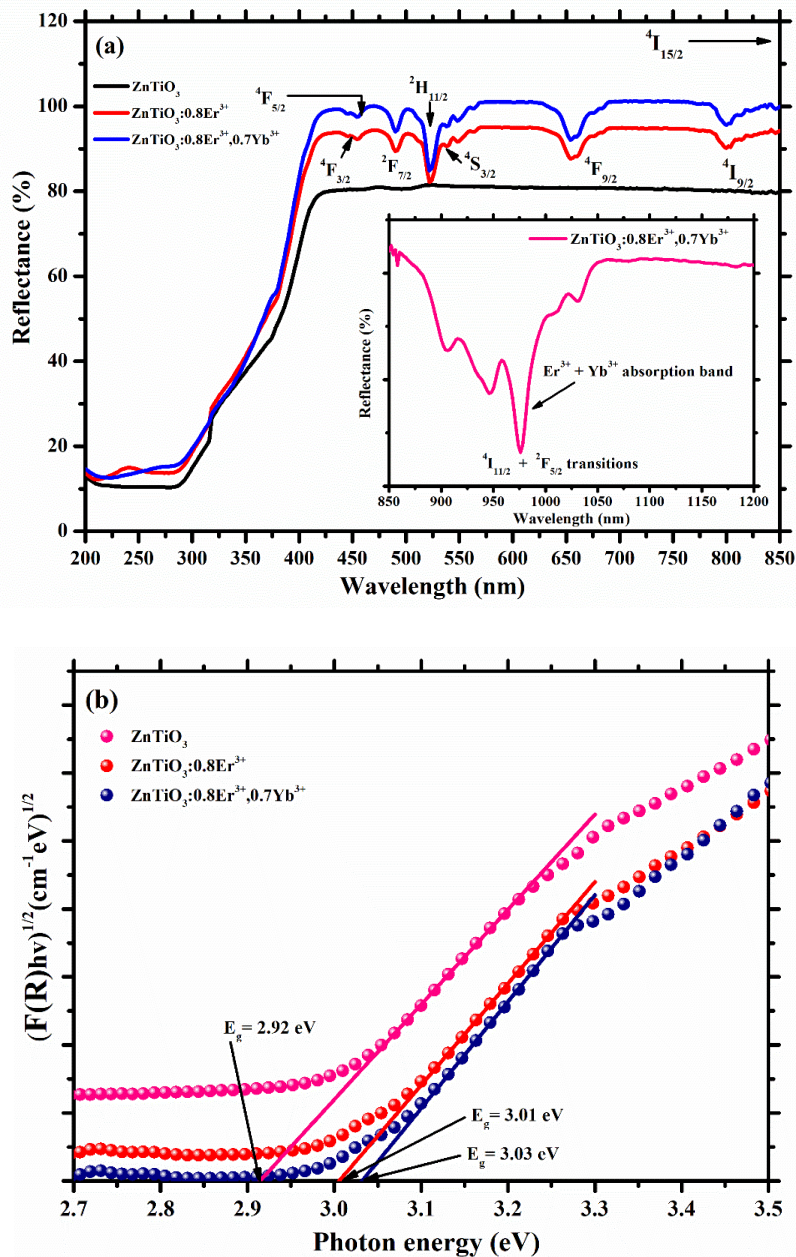
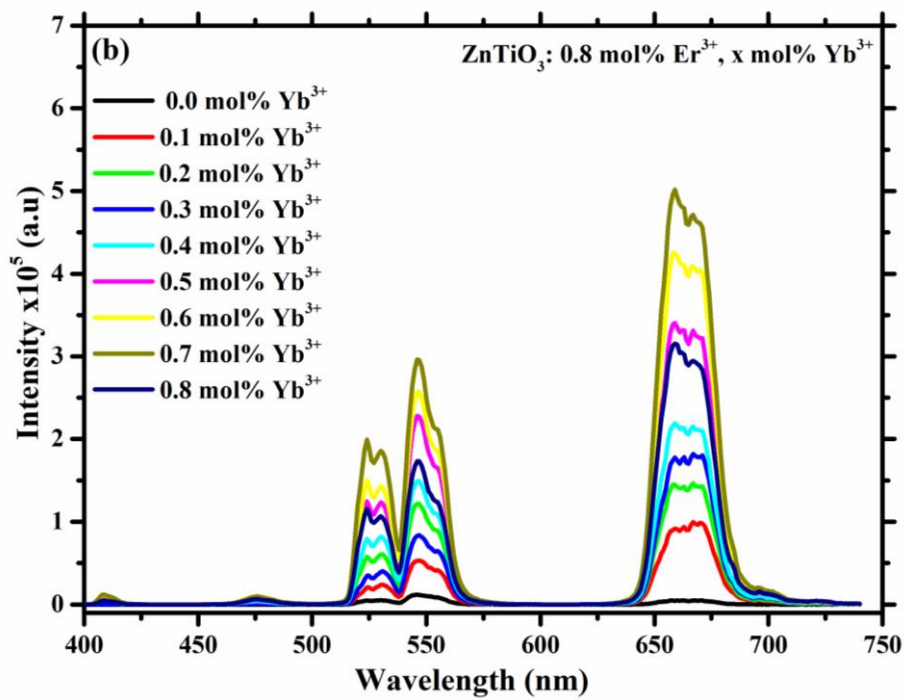
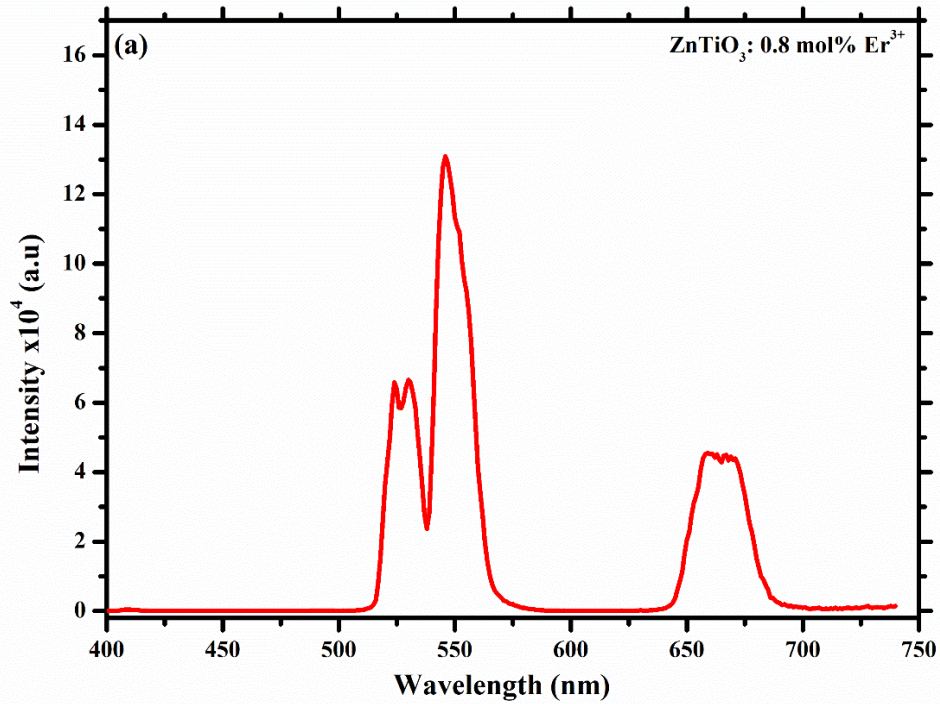


Figure 7.3: (a) The diffuse reflectance spectra and (b) Kubelka Munk's plots of ZnTiO₃, ZnTiO₃: Er³⁺ and ZnTiO₃: Er³⁺, Yb³⁺ phosphors.

7.3.4. Up-conversion luminescence analysis

The UC spectra of optimized ZnTiO₃:Er³⁺ and ZnTiO₃:Er³⁺,Yb³⁺ phosphor were measured under 980 nm excitation, using a continuous laser diode (laser power 1500 mW). As shown in Fig. 7.4 (a) the UC emission spectra show green emission lines centred at ~527 nm, ~545 nm and red emission line centred at ~665 nm. The UC emission lines correspond to the ²H_{11/2} →

$^4I_{15/2}$, $^4S_{3/2} \rightarrow ^4I_{15/2}$ and $^4F_{9/2} \rightarrow ^4I_{15/2}$ electronic transitions of Er^{3+} ions, respectively [31, 38, 39]. The intensity of the 0.8 mol % Er^{3+} ions was increased with the variation of the Yb^{3+} content and then decreased after reaching the maximum intensity due to the concentration quenching.



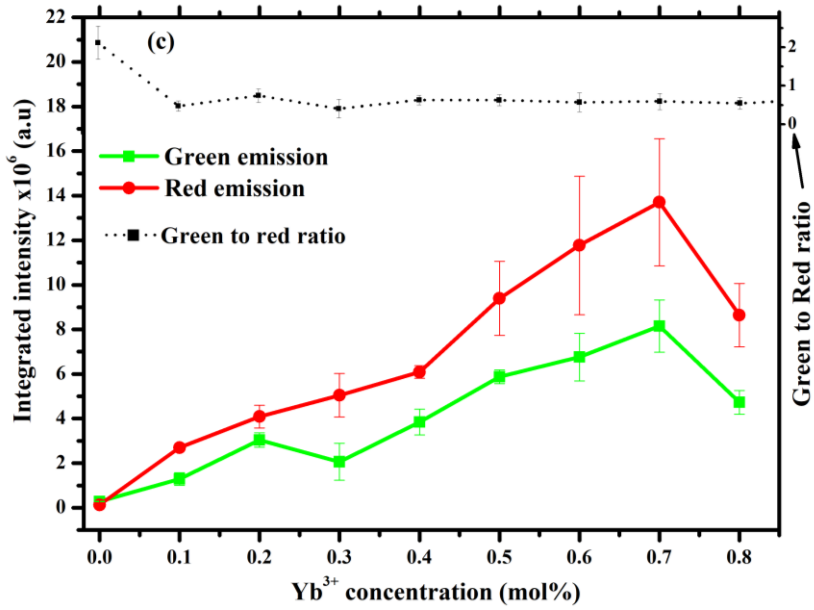


Figure 7.4: Up-conversion emission spectra of (a) $\text{ZnTiO}_3:0.8\text{mol}\%\text{Er}^{3+}$ and (b) $\text{ZnTiO}_3:0.8\text{mol}\%\text{Er}^{3+}, x\text{mol}\%\text{Yb}^{3+}$ ($x = 0.1 - 0.8$ mol%) phosphors under 980 nm excitation wavelength. (c) Comparison of integrated intensities of green and red emission emissions of $\text{ZnTiO}_3:0.8\text{mol}\%\text{Er}^{3+}, x\text{mol}\%\text{Yb}^{3+}$ phosphors.

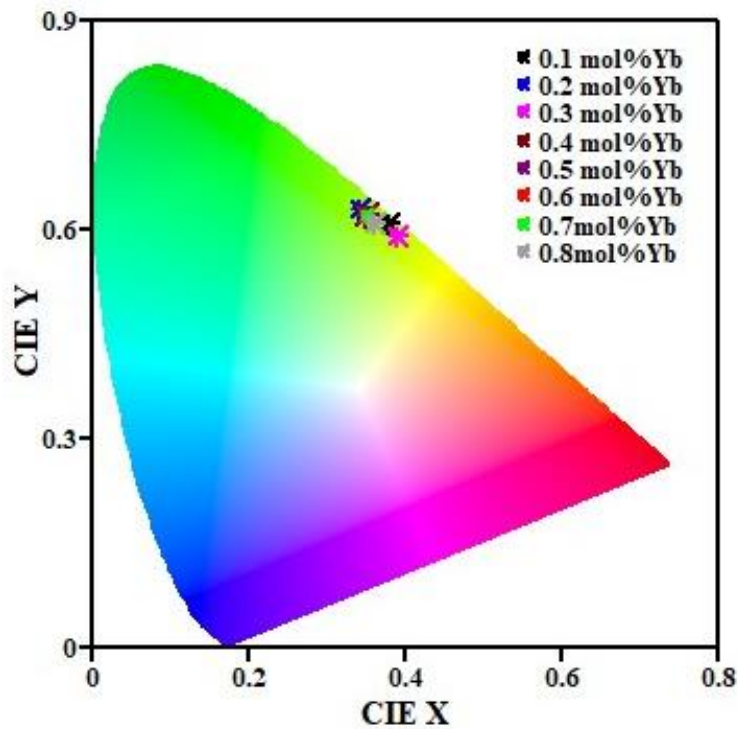


Figure 7.5: The CIE colour chromaticity diagram of $\text{ZnTiO}_3:0.8\text{mol}\%\text{Er}^{3+}, x\text{mol}\%\text{Yb}^{3+}$ phosphors.

The optimum concentration for $\text{Er}^{3+}/\text{Yb}^{3+}$ -co-doped samples showing the strongest UC emission intensity were found to be 0.8 mol% Er^{3+} and 0.7 mol% Yb^{3+} as shown in Fig. 7.4 (b). The optimum UC emission intensity of the $\text{ZnTiO}_3:\text{Er}^{3+}, \text{Yb}^{3+}$ phosphor was determined by fixing the optimum concentration of the activator Er^{3+} ion with variable concentration of sensitizer Yb^{3+} ion, respectively. Weak violet and blue up-converted emission lines were observed around 410 and 480 nm, which were attributed to the ${}^2\text{H}_{9/2} \rightarrow {}^4\text{I}_{15/2}$ [40] and ${}^4\text{F}_{7/2} \rightarrow {}^4\text{I}_{15/2}$ electron transition of Er^{3+} [41], respectively. It is also noted that the emission intensity of Er^{3+} ions was increased in samples co-doped with Yb^{3+} ions. The distinct new violet emission and the increase in green and red emissions shown in Fig. 7.4 (b) are due to effective energy transfer of $\text{Yb}^{3+} \rightarrow \text{Er}^{3+}$ [42, 43] in ZnTiO_3 compound. The ratio of the emission intensity of the green to red emission changed when the concentration of Yb^{3+} ion was increased, as shown in Fig. 7.4 (c). Fig. 7.4 (c) demonstrate the integrated green to red intensity ratios varied from 0.36 to 2.15 for the fixed Er^{3+} concentration with variable Yb^{3+} concentration. The Commission Internationale de l'Eclairage (CIE) colour coordinates of Yb^{3+} emissions have been calculated by using the GoCIE software to study their photometric characteristics. Fig. 7.5 show the CIE diagrams of the emission of $\text{ZnTiO}_3:0.8 \text{ mol}\% \text{Er}^{3+}, x \text{ mol}\% \text{Yb}^{3+}$ phosphors obtained under the 980 nm laser excitation. From the figure, it has been observed that the colour co-ordinate for the $\text{ZnTiO}_3:0.8 \text{ mol}\% \text{Er}^{3+}, x \text{ mol}\% \text{Yb}^{3+}$ phosphor manifest greenish yellow. The calculated CIE coordinates are given in Table 7.1.

Table 7.1: Representation of the concentration and calculated Commission Internationale de l'Eclairage (CIE) coordinates of $\text{ZnTiO}_3:0.8 \text{ mol}\% \text{Er}^{3+}, x \text{ mol}\% \text{Yb}^{3+}$ phosphors.

Yb^{3+} concentration	X	Y
0.1	0.38	0.61
0.2	0.34	0.63
0.3	0.39	0.59
0.4	0.35	0.62
0.5	0.35	0.62
0.6	0.35	0.62
0.7	0.35	0.62
0.8	0.36	0.61

Fig. 7. 6 (a) shows up-conversion emission spectra of $\text{ZnTiO}_3: 0.8\text{mol}\% \text{Er}^{3+}, x\text{mol}\% \text{Yb}^{3+}$ obtained by varying the laser power. The variation in laser power changed the intensity of the up-conversion emission bands but did not change their overall shape of emissions as shown in both figures, which suggests that the samples exhibit excellent stability under laser excitation energy [31]. The power dependent spectra to analyse the physical mechanism of the UC process

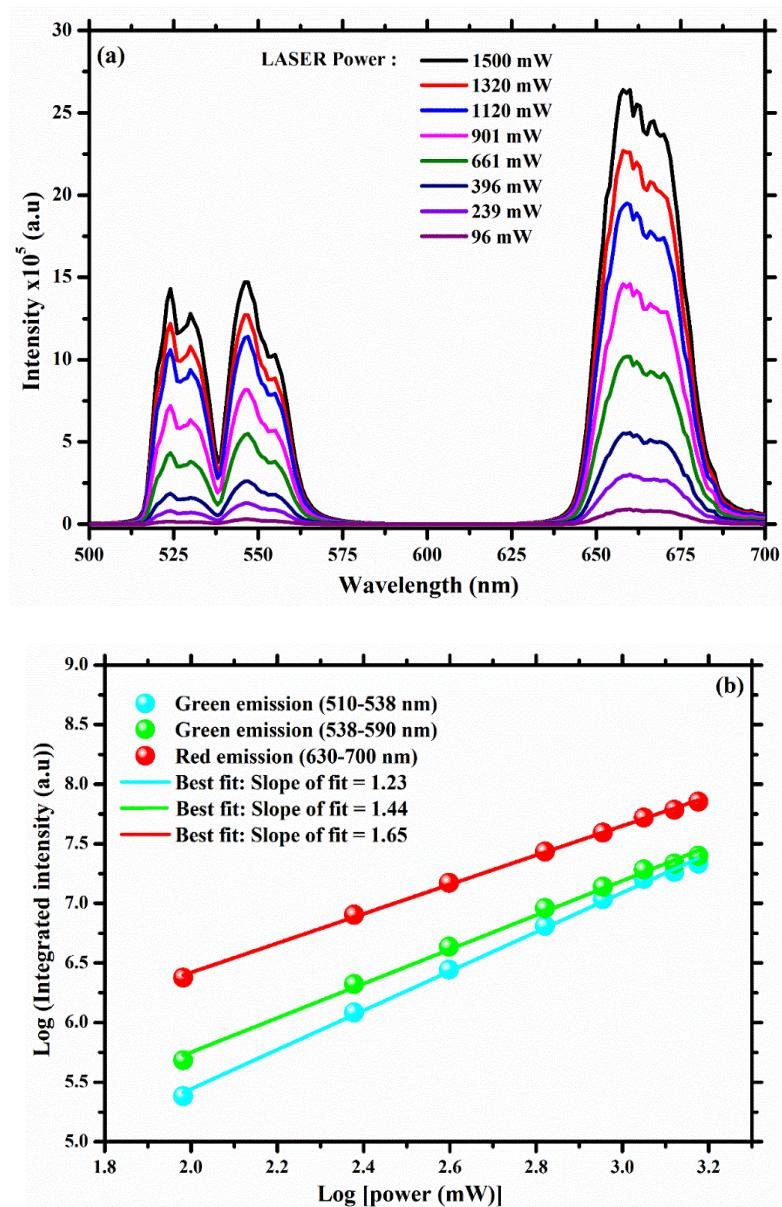


Figure 7.6: (a) Power dependence of up-conversion emission spectra of $\text{ZnTiO}_3:0.8\text{mol}\% \text{Er}^{3+}, 0.7\text{mol}\% \text{Yb}^{3+}$ under 980 nm excitation wavelength within a laser power range of 96 to 1500 mW, together with (b) logarithmic dependence of intensity versus power of these samples, respectively.

involved in the ZnTiO₃: 0.8mol%Er³⁺, xmol%Yb³⁺ phosphors under 980 nm laser excitation is presented in Fig. 7.6 (b). According to the relation $f(P) = AP^n$ where $f(P)$ is the UC emission intensity, A is a constant, P is the excitation power, and the quantity n (slope of logarithm curve) gives the minimum number of pumping photons required for the transition from the ground state to the luminescence emitting excited state [44]. As demonstrated in Fig. 7.6 (b), the observed slope values of the linear fitting for green emission are 1.23, 1.44 and 1.65. These slopes have values smaller than 2 for both green and red emissions, suggesting a two-photon process is involved for UC luminescence in the prepared materials.

The process of up-conversion mechanism in ZnTiO₃:Er³⁺,Yb³⁺ phosphor can be interpreted by the energy level diagram in Fig. 7.7, and this make easier to understand the proposed up-conversion mechanisms of green and red emission lines in the prepared phosphor. The schematic diagram illustrates the probable excitation pathways populating different UC emission states through possible energy transfer processes. Ground state absorption (GSA) is the first transition of Yb³⁺ and Er³⁺ ions whereby 980 nm excitation is absorbed by this GSA and populates the excited metastable levels [31, 45]. Yb³⁺ ions are excited from their fundamental ²F_{7/2} energy level and populate ²F_{5/2} energy level and Er³⁺ ions are excited from ⁴I_{15/2} ground state to the excited state ⁴I_{11/2} through GSA. Generally, the absorption cross section of Yb³⁺ ions at 980 nm is relatively large compared to Er³⁺ ions in the co-doped suitable hosts. Efficient energy transfer (ET) from Yb³⁺ to Er³⁺ ions may occur, physically corresponding to energy transfer up-conversion (ETU) represented by the black dashed arrows in Fig. 7.7 [31, 45, 46]. In this context, the ⁴I_{11/2} energy level of Er³⁺ is also populated through energy transfer from Yb³⁺ ions [31, 46] which can be expressed as the energy transition process: ²F_{5/2}(Yb³⁺) + ⁴I_{15/2}(Er³⁺) → ²F_{7/2}(Yb³⁺) + ⁴I_{11/2}(Er³⁺). The process of energy transition after GSA is the excited state absorption (ESA) of Er³⁺ ions by populating ⁴I_{9/2}, ²F_{7/2} and ²G_{11/2} energy levels of Er³⁺. In addition, ⁴I_{9/2}, ²F_{7/2} and ²G_{11/2} energy levels of Er³⁺ are populated through energy transfer from ²F_{5/2} energy level of Yb³⁺ ions. These processes can be expressed as energy transition process: ²F_{5/2}(Yb³⁺) + ⁴I_{13/2}(Er³⁺) → ²F_{7/2}(Yb³⁺) + ⁴I_{9/2}(Er³⁺), ²F_{5/2}(Yb³⁺) + ⁴I_{11/2}(Er³⁺) → ²F_{7/2}(Yb³⁺) + ⁴F_{7/2}(Er³⁺) and ⁴F_{9/2}(Yb³⁺) + ⁴I_{15/2}(Er³⁺) → ²F_{7/2}(Yb³⁺) + ⁴G_{11/2}(Er³⁺), respectively. Due to lack of stability of ions populating the ⁴G_{11/2} level of Er³⁺, some of the ions depopulate to excited metastable ²H_{9/2}, ⁴F_{7/2}, ⁴S_{3/2}, and ⁴F_{9/2} levels through non-radiative transition [47]. In addition, electrons at the ²F_{7/2} energy level of Er³⁺ are transferred non-radiatively to ⁴F_{9/2} energy level through a process called cross-relaxation (CR) energy

transfer given by ${}^4F_{7/2} \rightarrow {}^4F_{9/2}$ and ${}^4F_{9/2} \leftarrow {}^4I_{11/2}$ [45- 47]. Finally, electrons in the metastable levels of Er^{3+} relax to the ground state in the form of up-converted violet, blue, green and red luminescence due to ${}^2H_{9/2} \rightarrow {}^4I_{15/2}$, ${}^4F_{7/2} \rightarrow {}^4I_{15/2}$, ${}^4S_{3/2} \rightarrow {}^4I_{15/2}$ and $F_{9/2} \rightarrow {}^4I_{15/2}$ transitions at 410, 480, 545 and 665 nm.

There is a green emission at 527 nm, attributed to ${}^2H_{11/2} \rightarrow {}^4I_{15/2}$ transition as shown in Fig. 7.7. The excited Yb^{3+} ions in ${}^2F_{5/2}$ level completely transfer their energy to the ${}^2H_{11/2}$ energy level of Er^{3+} through ET or direct absorption of a 980 nm NIR photon through GSA from ${}^4I_{15/2}$ energy level to ${}^4I_{13/2}$ energy level. Also, through the ESA process from ${}^4F_{9/2}$ energy level to ${}^4G_{11/2}$ energy level of Er^{3+} ions and then the ions at ${}^4G_{11/2}$ energy level are transferred non-radiatively to the ${}^2H_{11/2}$ energy level through ${}^2H_{9/2}$, ${}^4F_{5/2}$ and ${}^4F_{7/2}$ energy levels. In addition, populating the ${}^2H_{11/2}$ energy level with ions is influenced by CR energy transfer process between Er^{3+} - Er^{3+} ions in the crystal field. The transitions taking place during the CR energy transfer is given by ${}^4I_{11/2} + {}^4I_{11/2} \rightarrow {}^4F_{7/2} + {}^4I_{15/2}$ [48]. Ions populated ${}^4F_{7/2}$ energy level through ET, CR or direct absorption of 980 nm decay non-radiatively to ${}^2H_{11/2}$ energy level of Er^{3+} , following a radiative decay to ${}^4I_{15/2}$ ground level in the form of green UC emission. The two transitions, ${}^2H_{11/2}$ (I) and ${}^2H_{11/2}$ (II) of the UC green emission in this case shows the Stark splitting of the ${}^2H_{11/2}$ energy level of Er^{3+} ions in the crystal field.

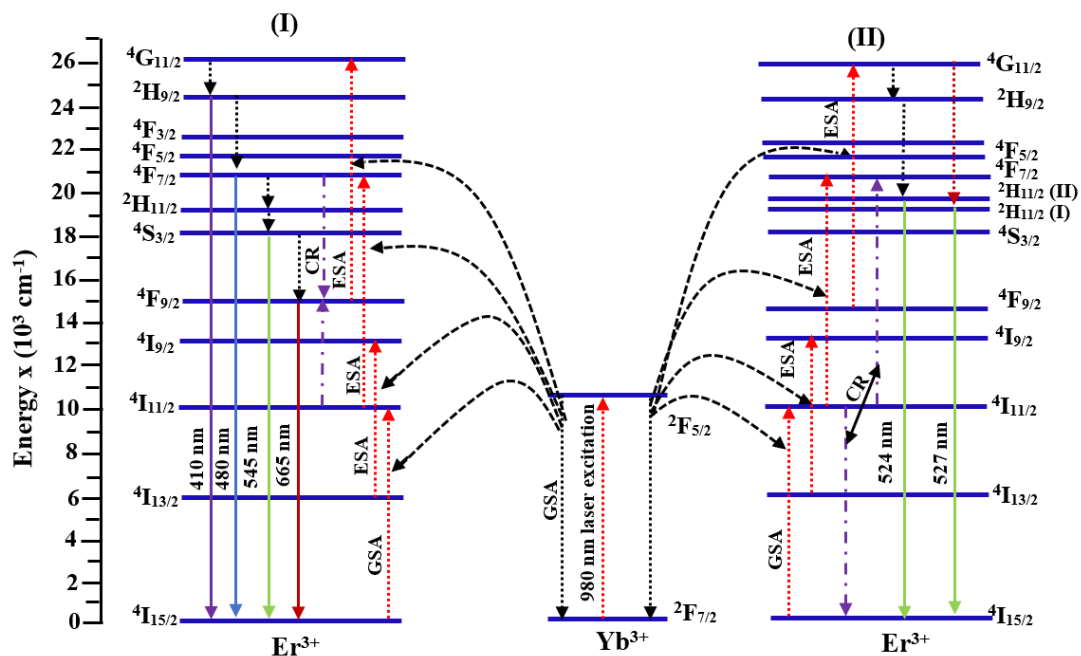


Figure 7.7: Schematic energy level diagram of $\text{Er}^{3+}/\text{Yb}^{3+}$ showing the possible energy transfer mechanism involved in UC process under an excitation of 980 nm.

For a better understating of energy transfer mechanism between Er^{3+} and Yb^{3+} ions in ZnTiO_3 host, the decay lifetimes (Fig. 7.8) at 550 nm associated with the ${}^4\text{F}_{9/2} \rightarrow {}^4\text{I}_{15/2}$ transition of Er^{3+} were measured with variable Yb^{3+} contents and 0.8 mol% fixed Er^{3+} content. The decay curves in Fig. 8 were fitted with the triple exponential function given by the following equation:

$$I(t) = I_0 + A_1 e^{-t/\tau_1} + A_2 e^{-t/\tau_2} + A_3 e^{-t/\tau_3} \quad [7.2]$$

where I and I_0 are the UC intensities at certain time t and 0 (from background), respectively, t is the time, A_1 , A_2 and A_3 are the fitting parameters, τ_1 , τ_2 and τ_3 are the decay components (lifetimes). The mean lifetime (τ) was be calculated by the following equation:

$$\tau = \frac{A_1 \tau_1^2 + A_2 \tau_2^2 + A_3 \tau_3^2}{A_1 \tau_1 + A_2 \tau_2 + A_3 \tau_3} \quad [7.3]$$

The calculated mean lifetimes of the ${}^4\text{F}_{9/2} \rightarrow {}^4\text{I}_{15/2}$ transition of Er^{3+} are shown in Table 2. The increase in lifetimes with Yb^{3+} co-doping system further suggest that more energy was transferred from Yb^{3+} to Er^{3+} ions.

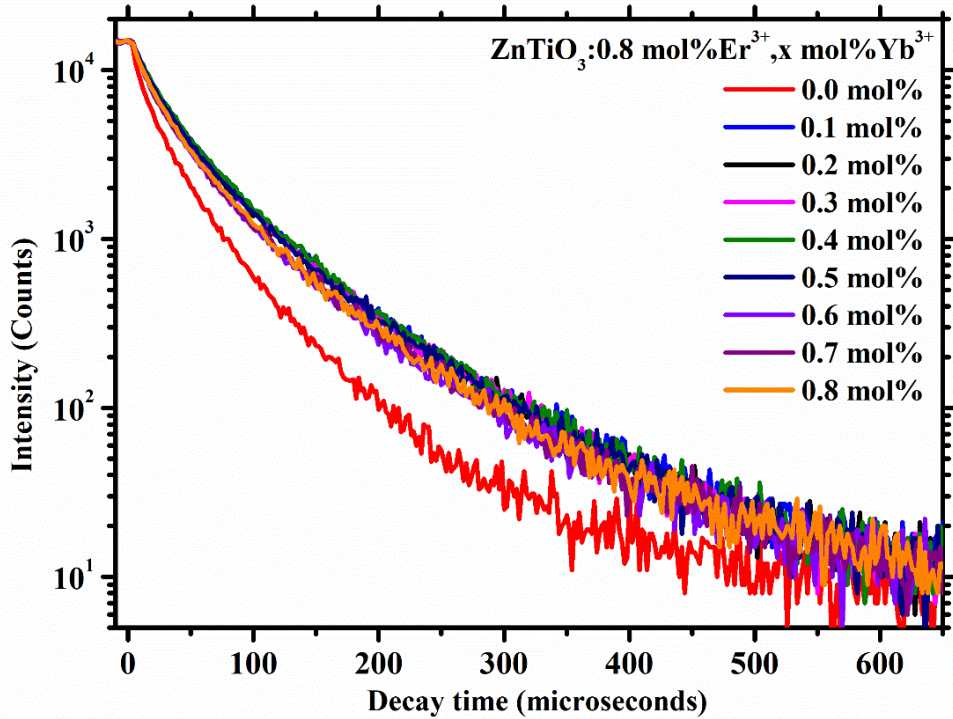


Figure 7.8: Decay curves of the ${}^4\text{F}_{9/2} \rightarrow {}^4\text{I}_{15/2}$ transition in $\text{ZnTiO}_3:\text{Er}^{3+}, \text{Yb}^{3+}$ phosphor.

Table 7.2: Photoluminescence decay lifetimes of ZnTiO₃:Er³⁺,Yb³⁺ phosphor.

Yb ³⁺ mol%	$\tau_1(\mu\text{s})$	$\tau_2(\mu\text{s})$	$\tau_3(\mu\text{s})$	$\tau_{\text{avg}}(\mu\text{s})$
0	14.8	43.3	136	44.5
0.1	20.2	54.3	130	62.4
0.2	19.2	55.9	135	61.6
0.3	19.9	54.8	127	61.4
0.4	20.5	61.4	157	63.2
0.5	18.2	52.4	124	61.2
0.6	17.7	53.1	138	57.8
0.7	16.4	50.7	126	58.6
0.8	18.5	53.4	133	58.8

7.4. Conclusion

ZnTiO₃:Er³⁺,Yb³⁺ up-converting phosphors have been successfully synthesized through a solid-state technique. XRD patterns confirmed that the phosphor crystallized in the eandrewsite structure with space group *R-3 (148)*. The morphology of the phosphors showed faceted particle shapes. The UC properties have been comprehensively investigated and the significant enhancement for UC emission intensity of Er³⁺ due to energy transfer from Yb³⁺ in co-doped samples has been observed. The observation of the nature of the energy transfer mechanism suggested that the cross-relaxation process was the preferred energy transfer between Er³⁺ and Yb³⁺ ions. With these observation, it is reasonable to conclude that ZnTiO₃:Er³⁺,Yb³⁺ may be suitable phosphor in NIR to visible up-converter for improvement of the power conversion efficiency of silicon solar cells.

7.5. References

- [1] P.M. Kumar, S.G.A. Josephine, G. Tamilarasan, A. Sivasamy and J. Sridevi. *J. Environ. Chem. Eng.* **6** (2018) 3907 – 3917.
- [2] E. Cerrato, C. Gionco, I. Berruti, F. Sordello, P. Calza and M.C. Paganini. *J. Solid State Chem.* **264** (2018) 42 – 47.
- [3] F. Zhou, C. Yan, Q. Sun and S. Komarneni. *Microporous Mesoporous Mater.* **274** (2019) 25 – 32.
- [4] M. Jalili, S. Basatani, M. Ghahari and E. Mohajerani. *Adv. Powder Technol.* **29** (2018) 855 – 862.
- [5] V. Kumar, A. Pandey, S.K. Swami, O.M. Ntwaeaborwa, H.C. Swart, and V. Dutta. *J. Alloys Compd.* **766** (2018) 429855 – 435.
- [6] R. Das, P. Phadke, N. Khichar and S. Chawla. *Superlattices Microstruct.* **83** (2015) 642 – 650.
- [7] W. Liua, H. Zhang, H. Wang, M. Zhanga, M. Guo. *Appl. Surf. Sci.* **422** (2017) 304 – 315.
- [8] H.N. Luitel, K. Ikeue, R. Okuda, R. Chand, T. Torikai, M. Yada and T. Watari. *Opt. Mater.* **36** (2014) 591 – 595.
- [9] K. Kobwittaya, Y. Oishi, T. Torikai, M. Yada, T. Watari, and H.N. Luitel. *Vacuum* **148** (2018) 286 – 295.
- [10] K. Kobwittaya, Y. Oishia, T. Torikai, M. Yada, T. Wataria, and H.N. Luitel. *Ceram. Int.* **43** (2017) 13505 – 13515.
- [11] E. Li, P. Zhang, S. Duan, J. Wang, Y. Yuan, B. Tang. Low temperature sintering of low-loss ZnTiO₃ microwave dielectric ceramics with Zn-B-Si glass. *J. Alloys Compd.* **647** (2015) 866 – 872.
- [12] J. Yu, D. Li, L. Zhu and X. Xu. *J. Alloys Compd.* **681** (2016) 88 – 95.
- [13] T. Surendar, S. Kumar and V. Shanker. *PCCP* **16** (2014) 728 – 735.
- [14] C. Wattanawikkam, T. Kansa-ard and W. Pecharapa. *Appl. Surf. Sci.* **474** (2019) 269 – 176.

- [15] S. Perween and A. Ranjan. *Sol. Energy Mater. Sol. Cells* **163** (2017) 148 – 156.
- [16] J.M.M. Buarque, D. Manzani, S.L. Scarpari, M. Nalin, S.J.L. Ribeiro, J. Esbenshade, M.A. Schiavon, and J.L. Ferrari. *Mater. Res. Bull.* **107** (2018) 295 – 307.
- [17] S. Lei, H. Fan, X. Ren, J. Fang, L. Ma and Z. Liu. *J. Mater. Chem. C* **2** (2017) 4040 – 4047.
- [18] R.S. Raveendrea, P.A. Prashanth, R.H. Krishna, N.P. Bhagya, B.M. Nagabhushana, H.R. Naika, K. Lingaraju, H. Nagabhushana and B.D. Prasa. *J. Asian Ceram. Soc.* **2** (2014) 357 – 365.
- [19] G. Xu, F. Liu, J. Lian, N. Wu, X. Zhang and J. He. *Ceram. Int.* **44** (2018) 19070 – 19076.
- [20] J. Benedek, T.T. Sebestyena and B. Bartok. *Renewable Sustainable Energy Rev.* **90** (2018) 516 – 535.
- [21] Y. Yang, S. Bremner, C. Menictas and M. Kay. *Renewable Sustainable Energy Rev.* **91** (2018) 109 – 125.
- [22] P. Acosta-Moraa, K. Domen, T. Hisatomi, H. Lyu, J. Mendez-Ramos, J.C. Ruiz-Morales, N.M. Khaidukov. *Opt. Mater.* **83** (2018) 315 – 320.
- [23] M. Rani and S.K. Tripathi. *Renew. Sust. Energ. Rev.* **61** (2016) 97 – 107.
- [24] D. Wang, H. Han, H. Gao, Z. Yang, Y. Xing, H. Cao, W. He, H. Wang, J. Gu and H. Hu. *Synth. Met.* **220** (2016) 41 – 47.
- [25] S.K. Ranjan, M. Mondal, V.K. Rai. *Mater. Res. Bull.* **106** (2018) 66 – 73.
- [26] J. Guo, W. Di, T. Aidilibike, Y. Li, X. Liu and W. Qin. *J. Rare Earths* **36** (2018) 461–467.
- [27] A. Zhou, F. Song, Y. Han, F. Song, D. Ju, K. Adnan, L. Liu and M. Feng. *J. Lumin.* **194** (2018) 225 – 230.
- [28] R. Rajeswaria, K. Susmitha, C.K. Jayasankar, M. Raghavender and L. Giribabua. *Sol. Energy* **157** (2017) 956 – 965.
- [29] D. Wang, B. Xu, K. Zou, M. Sun, G. Dong and J. Liu. *Opt. Mater.* **83** (2018) 124 – 130.

- [30] J. Mendez-Ramos, P. Acosta-Mora, J.C. Ruiz-Morales, M. Sierra, A. Redondas, E. Ruggiero, L. Salassa, M.E. Borges, and P. Esparza. *Opt. Mater.* **41** (2015) 98 – 103.
- [31] B.P. Kore, A. Kumar, L. Erasmus, R.E. Kroon, J.J. Terblans, S.J. Dhoble and H.C. Swart. *Inorg. Chem.* **57** (2018) 288 – 299.
- [32] W.O. Sung, J.B. Hyun, C.B. Young, S. Yang-Kook. *J. Power Sources* **173** (2007) 502 – 509.
- [33] B. Ozturk and G.S.P. Soyulu. *Ceram. Int.* **42** (2016) 11184 – 11192.
- [34] V. Singh, P. Haritha, V. Venkatramu and S.H. Kim. *Spectrochim. Acta, Part A* **126** (2014) 306 – 311.
- [35] K.M. Girish, S.C. Prashantha, and H. Nagabhushana. *J. Sci.: Adv. Mater. Devices* **2** (2017) 360 – 370.
- [36] H. Eskandarloo, A. Badiei, M.A. Behnajady, A. Tavakoli and G.M. Ziarani. *Ultrason. Sonochem.* **29** (2016) 258 – 269.
- [37] K. Joshi, M. Rawat, S.K. Gautam, R.G. Singh, R.C. Ramola and F. Singh. *J. Alloys Compd.* **680** (2016) 252 – 258.
- [38] J. Janek, R. Lisiecki, W. Ryba-Romanowski, J. Pisarska and W.A. Pisarski. *Opt. Mater.* **74** (2017) 105 – 108.
- [39] I. Soltani, S. Hraiech, K. Horchani-Naifer and M. Ferid. *Opt. Mater.* **77** (2018) 161 – 169.
- [40] R. Elleuch, R. Salhi, J.-L. Deschanvres and R. Maalej. *RSC Adv.* **5** (2015) 60246 – 60253.
- [41] A.J.M. Sales, D.G. Sousa, H.O. Rodrigues, M.M. Costa, A.S.B. Sombra, F.N.A. Freire, M.J. Soares, M.P.F. Graça and J. Suresh Kumar. *Ceram. Int.* **42** (2016) 6899 – 6905.
- [42] D. Hernandez-Pinilla, P. Molina, J.L. Plaza, L.E. Bausa, and M.O. Ramirez. *Opt. Mater.* **63** (2017) 173 – 178.
- [43] A. Shyichuk, S.S. Camara, I.T. Weber, A.N.C. Neto, L.A.O. Nunes, S. Lis, R.L. Longo and O.L. Malta. *J. Lumin.* **170** (2016) 560 – 570.
- [44] J. Grube and G. Krieke. *J. Lumin.* **203** (2018) 376 – 384.
- [45] S. Liu, S. Liu, M. Zhou, X. Ye, D. Hou and W. You. *RSC Adv.* **7** (2017) 36935 – 36948.

- [46] Y. Ma, G. Xiang, J. Zhang, Z. Liu, P. Zhou, W. Liu, X. Tang, S. Jiang, X. Zhou, L. Li, Y. Luo and Y. Jin. *J. Alloys Compd.* **769** (2018) 325 – 331.
- [47] X. Cheng, X. Ma, H. Zhang, Y. Ren, and K. Zhu. *Physica B* **521** (2017) 270 – 274.
- [48] D.H. Kim, J.H. Ryu, J.H. Chung, K.B. Shim, and S.Y. Cho. *J. Electrochem. Soc.* **158** (11) (2011) J345 – J348.

Chapter 8: Up-conversion luminescence properties of ZnTiO₃:Er³⁺,Yb³⁺ thin films synthesized by pulsed laser deposition

8.1. Introduction

The development of nanocrystalline semiconducting thin films has become the topic of interest in the field of research because of their many characteristic properties and diverse applications [1]. In the past years, research has been carried out on the application of the metal oxide semiconductor thin films on photovoltaic cells. They used either pure metal oxide semiconductors or those doped with down and up-converting rare-earth ions in the host lattice to enhance the efficiency of various photovoltaic cells [2 - 4]. An interesting research has been carried out for studying the optical properties of oxide materials such ZnTiO₃ [5, 6], Ta₂O₅:Eu, Ce [7], SiO₂-TiO₂:Er³⁺/Yb³⁺/Eu³⁺ [8], CeO₂:Er, Yb [9], etc on the photovoltaic cells. From among the oxide materials, zinc titanate (ZnTiO₃) is one of the most interesting oxide semiconductors that display good catalytic properties with different polymorphs and widely used in the fields of photovoltaic cells [10].

ZnTiO₃ is known as a ternary oxide material which is capable of enhancing the photovoltaic response, due to the larger electron mobility and wide band gap energy. There are different phases of zinc titanate, which include Zn₂Ti₃O₈, ZnTiO₃ and Zn₂TiO₄. These phases of zinc titanate crystallize at different temperatures. The Zn₂Ti₃O₈ is a metastable phase, which crystallizes at a temperature lower than 800 °C, ZnTiO₃ is thermodynamically stable between 800 and 850 °C and Zn₂TiO₄ is produced at annealing temperature above 850 °C. The ZnTiO₃ phase resembles a structure called rhombohedral ilmenite structure [11, 12]. Sau et al. [11], investigated the crystallographic phases of zinc titanate prepared at different temperatures for photovoltaic (PV) application. ZnTiO₃ absorbs certain wavelengths of the electromagnetic spectrum and hinders the efficiency of PVs when it is incorporated. To avoid this problem, the up-conversion rare earth ions are the ideal dopants due to their efficient up-conversion

luminescence from infrared to visible radiation [10]. The incorporation of rare earth ions in oxide materials increases the number of absorbed incident photons, and this effect can enhance the power conversion efficiency of PV cells. Er^{3+} coupled with Yb^{3+} ions have been used to convert infrared photons to visible photons, which are easily absorbed by PVs [13, 14]. In the $\text{Er}^{3+}/\text{Yb}^{3+}$ co-doped system, Er^{3+} ions are used as activators, and Yb^{3+} ions as sensitizers. The role of the latter is to enhance the emission intensity of the activators [15, 16].

In this work $\text{ZnTiO}_3:\text{Er}^{3+},\text{Yb}^{3+}$ powders were synthesized for the first time using the conventional solid-state reaction and annealed at different calcination temperature to get a pure ZnTiO_3 . Further, the $\text{ZnTiO}_3:\text{Er}^{3+},\text{Yb}^{3+}$ phosphor that presented the optimal luminescence intensity was ZnTiO_3 powder containing 0.8 mol% Er^{3+} and 0.7 mol% Yb^{3+} . This powder was deposited on the silicon (100) using pulsed laser deposition (PLD) technique, and it was investigated by heating the substrate temperature from 100 to 600°C during the deposition. The aim of this research was to fabricate $\text{ZnTiO}_3:\text{Er}^{3+},\text{Yb}^{3+}$ thin films and investigate their UC luminescence properties for PVs applications. The results demonstrate that the thin film with a substrate temperature of 500 °C shows the most intense emission intensity.

8.2. Experimental procedure

$\text{ZnTiO}_3:\text{Er}^{3+},\text{Yb}^{3+}$ thin films were prepared by conventional solid-state reaction technique. Commercial zinc oxide (ZnO , Sigma-Aldrich, purity 99.9%), titanium dioxide (TiO_2 , Sigma-Aldrich, purity 99.7%), erbium (III) acetate hydrate ($\text{Er}(\text{CH}_3\text{COO})_3\cdot\text{H}_2\text{O}$, Sigma-Aldrich, purity 99.9%) and ytterbium (III) acetate hydrate ($\text{Yb}(\text{CH}_3\text{COO})_3\cdot\text{H}_2\text{O}$, Sigma-Aldrich, purity 99.9%) were used as starting materials. The stoichiometric amounts of ZnO (1.00 g) and TiO_2 (0.98 g) were first mixed and ground together in a ball mill for 1 hour at room temperature. Different masses of erbium acetate were incorporated to the ball milled powder and mixed using a pestle and mortar. Similarly, with different masses of ytterbium acetate for the co-doped samples. The resulting powders were annealed at 800 °C for 3 hours in air, inside a furnace. Before preparing the thin films, the sample powder was pressed into a pellet inside a target sample holder. The pellet was annealed at 800 °C for 8 hours in air, and then mounted on the rotating target holder inside the PLD system. The thin films were deposited onto a silicon (100) substrate. Before the deposition, the Si substrate was cleaned with ethanol using an ultrasonic bath for 15 minutes, and then dried by blowing it with N_2 gas on the surface. The substrate was mounted on the substrate holder which was inserted parallel to the target inside

the PLD system. The distance between the Si substrate and the target was kept constant at 3.5 cm. The PLD chamber was pumped down to 3.00×10^{-5} mbar., and then O₂ was backfilled to obtain 10 mTorr. The 266 nm fourth harmonic of a Nd:YAG laser (8 ns, 40 mJ/pulse, 0.767 J/cm² and 10 Hz pulse repetition rate) was used for to evaporate the sample. The deposition time was 30 minutes for all the samples. The substrate temperature was varied from 100 to 600 °C, at intervals of 100 °C.

The phase formation of the thin films was examined using an X-ray diffractometer (XRD) from Rigaku Smartlab, which was equipped with a monochromatic CuK α ($\lambda = 0.15405$ nm) irradiation source that was operated at 200 mA current and 45 kV. The particle surface morphology was studied using the Jeol JSM-7800 field emission scanning electron microscope (FE-SEM). The distribution of the ions on the surface and the 3D thin film maps were obtained using the time of flight secondary ion mass spectroscopy (TOF-SIMS). A pulsed 30 kV Bi₁⁺ primary ion beam operated at a DC current of 0.4 pA and pulse repetition rate of 10 kHz (100 μ s), was used to probe the surface. The diffused reflectance measurements of the thin films were done using the Perkin Elmer Lambda 1050 UV-Vis-NIR absorption spectrometer. The photoluminescence (PL) measurements were conducted using an Edinburgh Instruments FLS980 system with a 980 nm diode laser as an excitation source for up-conversion measurements.

8.3. Results and discussion

8.3.1. Structural and morphological analysis

Fig. 8.1 depicts the XRD patterns and the peak intensities of the ZnTiO₃: Er³⁺, Yb³⁺ thin film deposited on the silicon (100) which was heated at different temperatures. Almost similar XRD peaks were obtained under all different substrate temperature; this is evidence for efficient inter-diffusion between ZnTiO₃: Er³⁺, Yb³⁺ to silicon substrate. The figure shows that the XRD patterns of the samples exhibits crystalline phase of eandrewsite trigonal ZnTiO₃ (ICSD file number 01-026-1500) with space group **R-3 (148)** and cell parameters $a = b = 5.078$ Å $c = 13.927$ Å. The XRD results revealed the presence of by-products of Er₂O₃ (ICSD file no. 01-077-6226) and Yb₂O₃ (ICSD file no. 01-07-6635). All the diffraction peaks of ZnTiO₃ can be indexed to (1 0 1), (1 1 0), (2 0 2), (2 0 5), and (0 1 8) reflections at $2\theta = \sim 33.0^\circ, 35.5^\circ, 43.3^\circ, 53.4^\circ, \text{ and } 57.3^\circ$, respectively. The diffraction peaks of the by-product phases of Er₂O₃ can be

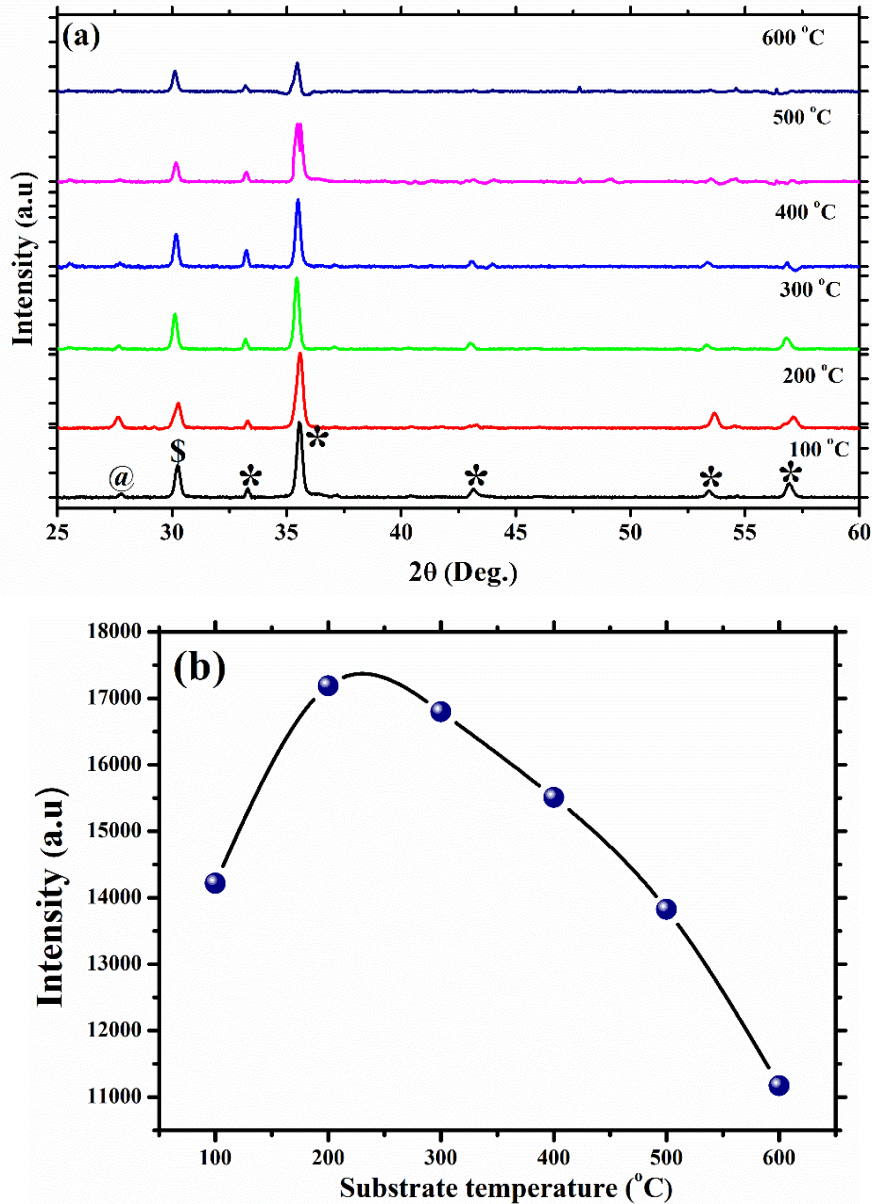


Figure 8.1: (a) X-ray Diffraction patterns and (b) peak intensities of the ZnTiO₃: Er³⁺,Yb³⁺ thin film deposited on the silicon (100) and heated at different temperatures.

indexed to (3 1 0) reflection at $2\theta = \sim 26.9^\circ$, while that one of Yb₂O₃ can be indexed to (2 2 2) reflection at $2\theta = \sim 29.9^\circ$. The formation of Er₂O₃ and Yb₃O₃ phases due to doping is explained in detail in chapter 7. Comparing the intensity along (110) orientation of the samples grown at different substrate temperature, the XRD peaks intensity slightly increased from the 100 °C to 200 °C and decreased significantly at temperature up to 600 °C as shown in Fig. 8.1 (b). This might be due to the enhanced thickness of the films as it increased and decreased or the enhancement of the crystallinity of ZnTiO₃:Er³⁺,Yb³⁺ thin films [17].

Fig. 8.2 depicts the scanning electron microscopy (SEM) image of $\text{ZnTiO}_3: \text{Er}^{3+}, \text{Yb}^{3+}$ thin film deposited at 500 °C. We can see in Fig. 8.2 that the surface morphology of the $\text{ZnTiO}_3: \text{Er}^{3+}, \text{Yb}^{3+}$ thin film shows large spherical particles which are segregated embedded on an amalgamate small spherical particles. The inset in the Fig. 8.2 shows the SEM image of $\text{ZnTiO}_3: \text{Er}^{3+}, \text{Yb}^{3+}$ powder. The SEM depicts that the $\text{ZnTiO}_3: \text{Er}^{3+}, \text{Yb}^{3+}$ powder consisted of spherical particles, with some degree of faceting, agglomerated together.

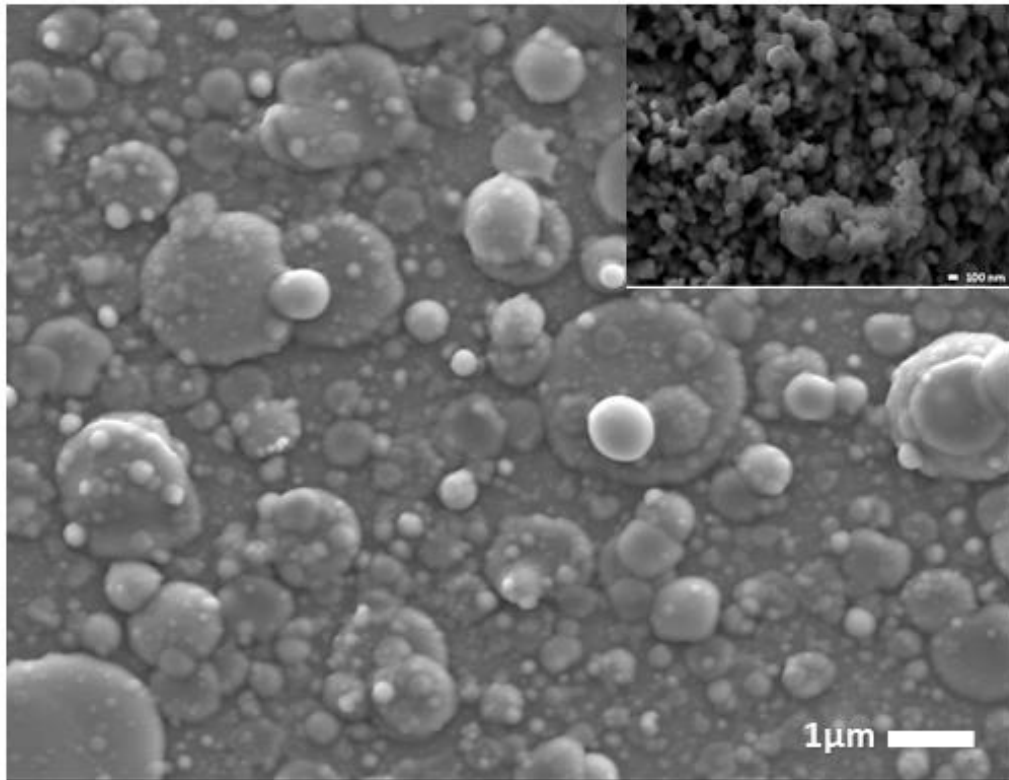


Figure 8.2: FE-SEM image of $\text{ZnTiO}_3: \text{Er}^{3+}, \text{Yb}^{3+}$ thin film deposited at 500 °C .

8.3.2. TOF-SIMS analysis

Fig. 8.3 (a) – (d) depicts the distribution of the Er^{3+} and Yb^{3+} ions in ZnTiO_3 phosphor which was investigated using the TOF-SIMS, from the 0.8 mol% Er^{3+} and 0.7 mol% Yb^{3+} co-doped ZnTiO_3 thin film fabricated at temperature of 500 °C. The surface mapping of the film was obtained over an area of 100 x 100 μm^2 . Fig. 8.3 (a) depicts the image overlay of the mapped ions, which shows homogenous distribution of the Er^{3+} and Yb^{3+} ions, indicating that they were successful incorporated in ZnTiO_3 . The distribution of the ions on the surface of the films are shown in figure 8.3 (c) – (d); Zn^+ , TiO^+ , Er^+ and Yb^+ . A red colour for both Zn^+ and TiO^+

shown in Fig. 8.3 (b) is due to the overlapping of the peaks of Zn^+ and TiO^+ ions. Also, the relative sensitivity factor for Zn^+ is very small/low compared to TiO^+ and Si.

Fig. 8.4 shows a 3D overlay analysis of the inter-diffusion process of Zn^+ , TiO^+ , Er^+ and Yb^+ ions at different substrate temperatures. In the figures, the green layer indicates the thin film, blue the Si substrate, and the cyan the inter-diffusion layer between the thin film and the substrate. From the images, it is observed that the increment in temperature increased inter-diffusion. It was also observed that the inter-diffusion process can be locally enriched by increasing the Si substrate temperature or heat treatment, as also revealed by Balakrishna et al. [18]. The TOF-SIMS depth profiles for $\text{ZnTiO}_3: \text{Er}^{3+}, \text{Yb}^{3+}$ thin films were collected in order to investigate the elemental distribution with depths from the surface down to the substrate.

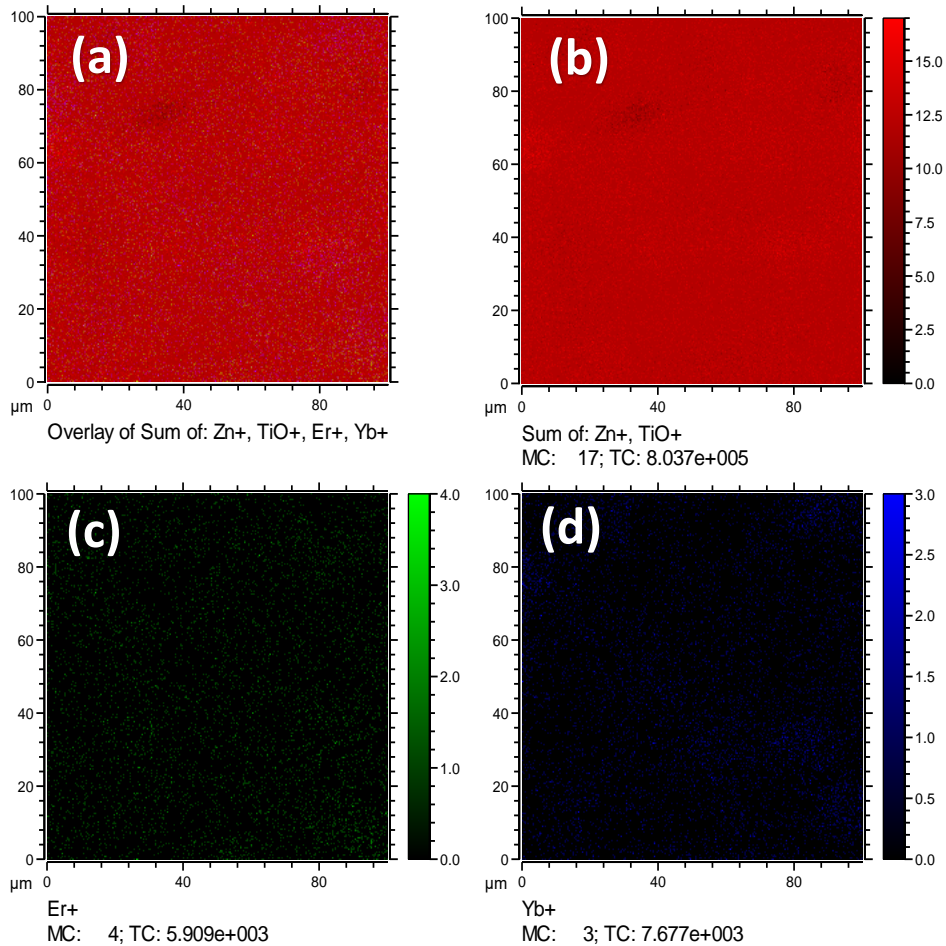


Figure 8.3: A TOF-SIMS maps of the ions on the surface of the 0.8 mol% Er^{3+} and 0.7 mol% Yb^{3+} co-doped ZnTiO_3 thin film fabricated at temperature of 500 °C.

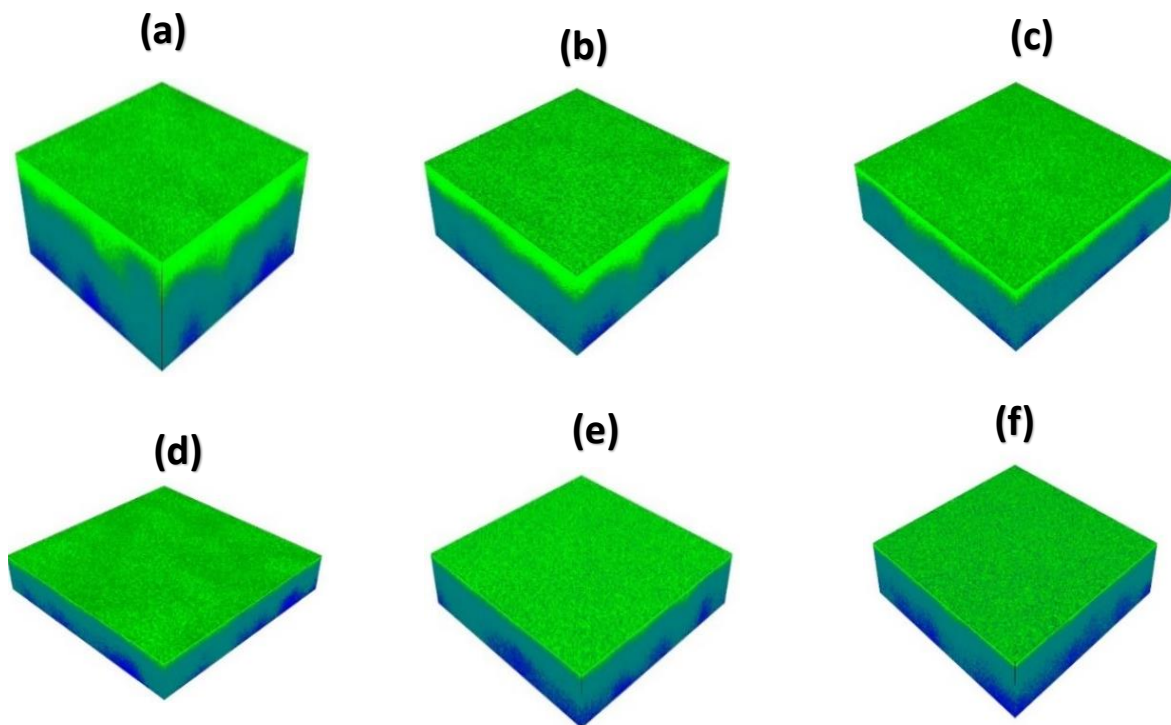


Figure 8.4: 3D overlay chemical composition of $\text{ZnTiO}_3: \text{Er}^{3+}, \text{Yb}^{3+}$ thin film fabricated at (a) 100 °C, (b) 200 °C, (c) 300 °C, (d) 400 °C, (e) 500 °C and (f) 600 °C.

The TOF-SIMS depth profile for the thin films were recorded in a positive secondary ion mode by the Bi_1^+ ion beam as shown in Fig. 8.5, by monitoring the TiO^+ and Si^+ , Er^+ , Yb^+ ions. As mentioned above, the Zn^+ and TiO^+ peaks overlap and therefore the TiO^+ was used to monitor ZnTiO_3 with respect to Si. Looking at the thin film fabricated at 100 °C, the C_2H_3^+ , Er^+ and Yb^+ profiles were highly suppressed by the profiles of Si and TiO^+ . On the surface there was more ZnTiO_3 as indicated by the TiO^+ depth profiles, which decreased as the substrate temperature increases. The enrichment of the region with Si^+ ions occurred with an increase in substrate temperature. The fact that the Si^+ region enriched with substrate temperature was due to the continued effectiveness of the inter-diffusion of Si^+ at the film/ Si^+ interfaces, respectively. However, the results from Fig. 8.4 and 8.5 clearly shows that the thin films at a lower substrate temperature was thicker and become thinner with an in increase in substrate temperature.

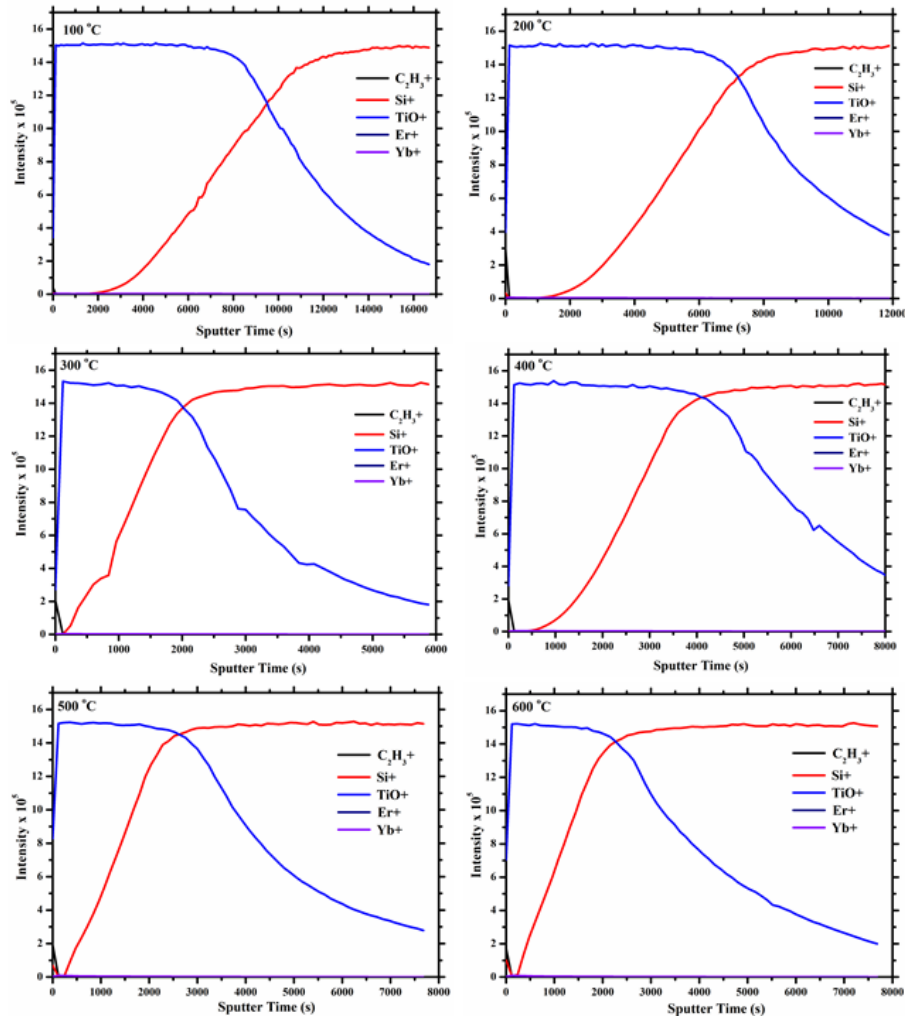


Figure 8.5: TOF-SIMS depth profiles of the ZnTiO₃: Er³⁺, Yb³⁺ thin film deposited at different substrate temperatures as indicated.

The diffuse reflectance spectra of ZnTiO₃: Er³⁺, Yb³⁺ thin films deposited at different temperatures were recorded, as shown in Fig. 8.6. The samples show a very low reflectance (25 - 45%) in the visible spectral region (i.e., 400 – 800 nm) and 12 - 35% reflectance in the UV region of light. In addition, the region between 330 and 400 nm corresponds to the absorption edge of ZnTiO₃. As seen from the spectra, the reflectance percentages of the samples vary with the substrate temperature due to the differences in the thickness and morphological roughness of the films [19]. The observed bands below 330 nm in the reflectance spectra are an indication of additional absorbing centres within the conduction band of the material, which may be attributed to the deposition effects. As a result, the reflectance spectra show that the prepared thin films have a better absorption of ultraviolet electromagnetic waves.

8.3.3. UV-Vis-NIR analysis

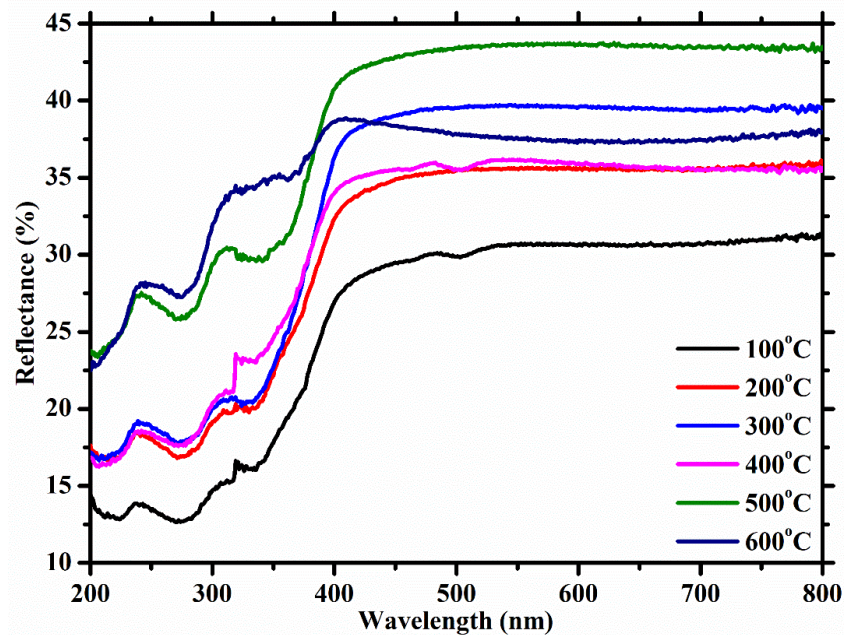


Figure 8.6: The optical reflectance spectra of ZnTiO₃:Er³⁺,Yb³⁺ thin films grown in different substrate temperatures.

8.3.4. Up-conversion luminescence analysis

Fig. 8.7 (a) depicts the visible emission spectra of ZnTiO₃:Er³⁺,Yb³⁺ thin films at different substrate temperatures, which were measured after exciting the samples with a 980 nm LED laser beam. The spectra show five emission peaks at 410, 480, 525, 547 and 660 nm, assigned to $^2H_{9/2} \rightarrow ^4I_{15/2}$, $^4F_{7/2} \rightarrow ^4I_{15/2}$, $^2H_{11/2} \rightarrow ^4I_{15/2}$, $^4S_{3/2} \rightarrow ^4I_{15/2}$ and $^4F_{9/2} \rightarrow ^4I_{15/2}$ electronic transitions of Er³⁺ ions, respectively [20-23]. The emission intensity was increased with an increase in substrate temperature and then decreased after reaching the maximum intensity due to luminescence thermal quenching [24] as shown in the inset of Fig. 8.7 (a). The optimum substrate temperature which is at 500 °C shows the strongest up-conversion emission intensity of the thin films. This points out that the growth of ZnTiO₃:0.8Er³⁺,0.7Yb³⁺ thin films on the substrate temperature of 500 °C is an optimum condition with intense up-conversion luminescence emission of Er³⁺/Yb³⁺ ions. According to Shewale et al. [25], the increase in luminescence emission intensity with the increase in the substrate temperature is due to the improvement of the crystal quality of the ZnTiO₃:Er³⁺,Yb³⁺ thin film at higher substrate temperature.

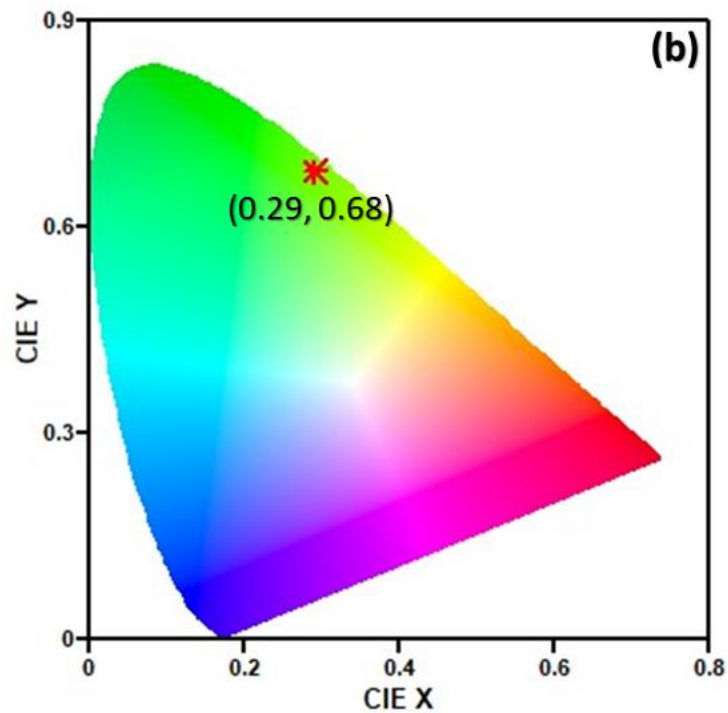
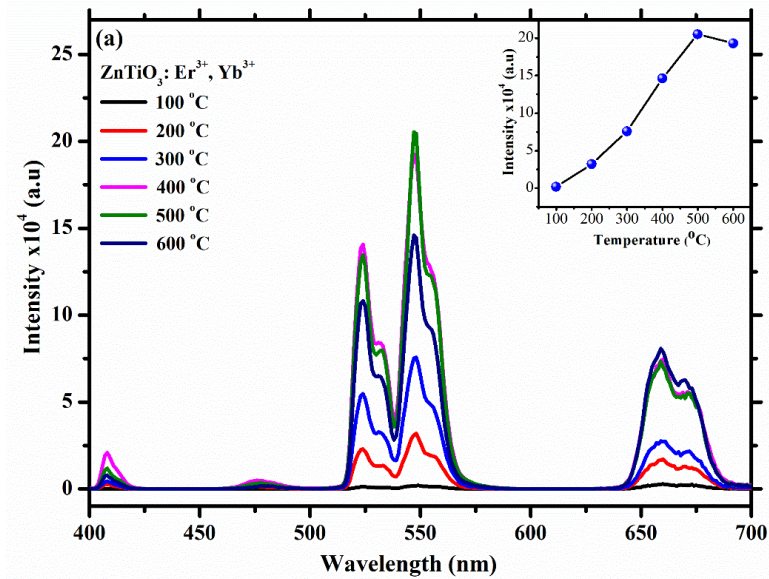


Figure 8.7: (a) PL spectra of $\text{ZnTiO}_3:\text{Er}^{3+}, \text{Yb}^{3+}$ thin film at different temperatures and (b) CIE chromaticity coordinates of $\text{ZnTiO}_3:\text{Er}^{3+}, \text{Yb}^{3+}$ thin film fabricated at 500 °C.

The Commission Internationale de l'Eclairage (CIE) colour coordinates was employed in order to evaluate the dominant characteristic emission colour of the optimized $\text{ZnTiO}_3:\text{Er}^{3+}, \text{Yb}^{3+}$ thin film as shown in Fig. 8.7 (b). The CIE chromaticity coordinate of the optimized $\text{ZnTiO}_3:\text{Er}^{3+}, \text{Yb}^{3+}$ thin film is (0.29, 0.68).

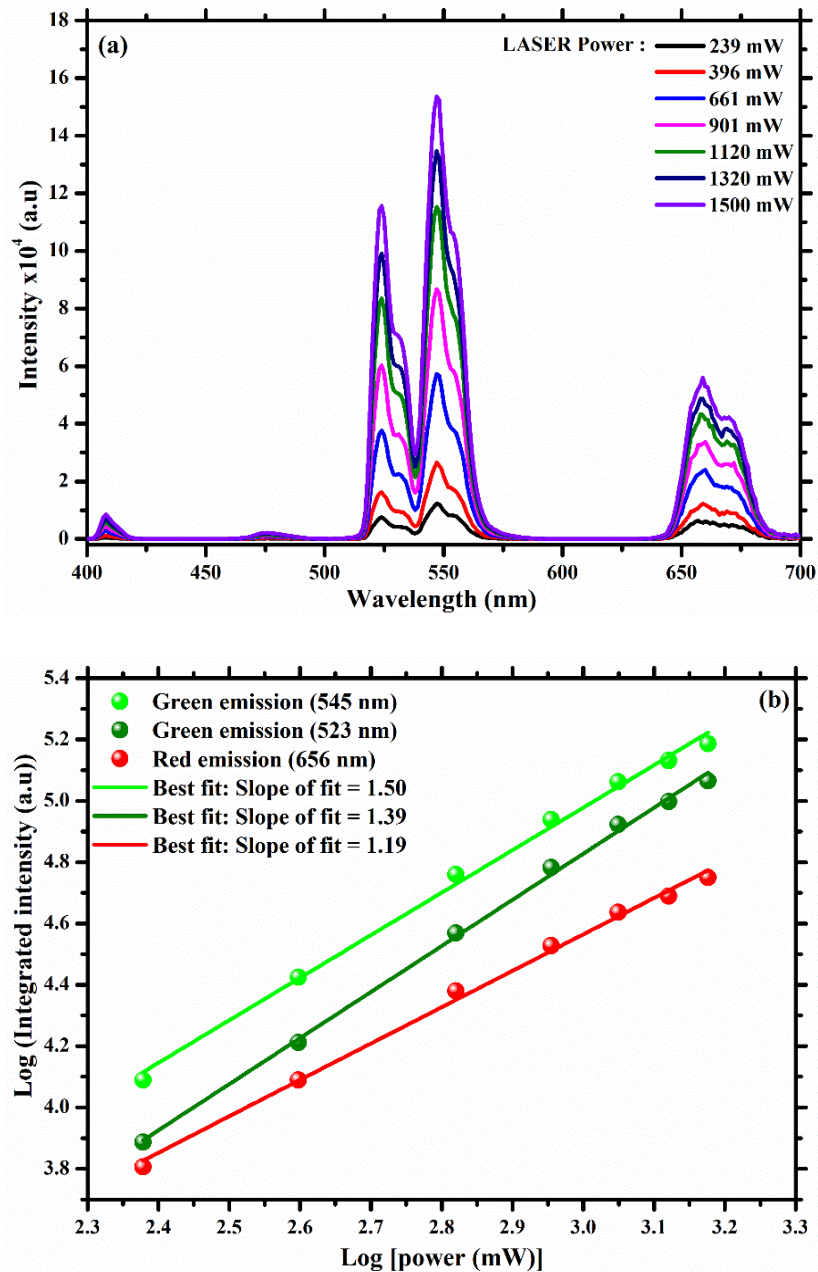


Figure 8.8: (a) Up-conversion emission spectra measured at different laser power and (b) logarithmic dependence of intensity versus power of ZnTiO₃:Er³⁺, Yb³⁺ thin film fabricated at 500 °C.

Fig. 8.8 (a) shows the emission spectra with the variation of laser power for ZnTiO₃:Er³⁺, Yb³⁺ thin film at a substrate temperature of 500 °C. It can be seen from the figure that the emission intensity of the sample increased with an increase in laser power. On the other hand, the pumping power dependence spectra of the up-conversion luminescence intensity for ZnTiO₃:Er³⁺, Yb³⁺ thin film under 980 nm laser excitation was investigated and presented in

Fig. 8.8 (b). The observed slope values of the linear fit of the log-log power dependences for both green emissions and red emission are 1.50, 1.39, and 1.19. The observed slope values suggest that one photon process is expected for up-conversion luminescence properties of ZnTiO₃:Er³⁺, Yb³⁺ thin film.

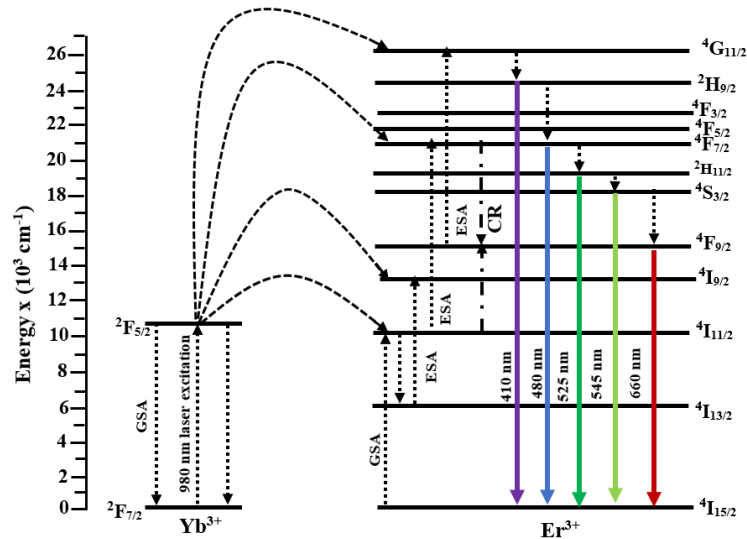


Figure 8.9: Energy transfer mechanism showing the radiative transitions for up-conversion process in ZnTiO₃:Er³⁺,Yb³⁺ films under an excitation of 980 nm.

The schematic energy level diagram of Er³⁺ and Yb³⁺ do-doped ZnTiO₃ film is shown in Fig. 8.9. The ground state absorption (GSA) is known as the first transition for Yb³⁺ and Er³⁺ ions under 980 nm excitation. Since the absorption cross section of Yb³⁺ is larger than that of Er³⁺, the 980 nm excitation is mostly absorbed by the Yb³⁺ ions [26]. In the case of ZnTiO₃:Er³⁺,Yb³⁺ thin films under an excitation of 980 nm, Yb³⁺ ions are excited from its fundamental ²F_{7/2} energy state and populate ²F_{5/2} energy state by absorbing 980 nm NIR photon via GSA process. In this case, the non-radiative relaxation takes place from ²F_{5/2} energy state back to ²F_{7/2} energy state and the ⁴I_{11/2}, ⁴I_{9/2}, ²F_{7/2} and ²G_{11/2} energy states of Er³⁺ are populated through the following energy transfer from excited state of Yb³⁺ ions [27]:

$$[{}^4I_{15/2}(\text{Er}^{3+}), {}^2F_{5/2}(\text{Yb}^{3+})] \rightarrow [{}^2F_{7/2}(\text{Yb}^{3+}), {}^4I_{11/2}(\text{Er}^{3+})] \quad (\text{i})$$

$$[{}^4I_{13/2}(\text{Er}^{3+}), {}^2F_{5/2}(\text{Yb}^{3+})] \rightarrow [{}^2F_{7/2}(\text{Yb}^{3+}), {}^4I_{9/2}(\text{Er}^{3+})] \quad (\text{ii})$$

$$[{}^4I_{11/2}(\text{Er}^{3+}), {}^2F_{5/2}(\text{Yb}^{3+})] \rightarrow [{}^2F_{7/2}(\text{Yb}^{3+}), {}^4F_{7/2}(\text{Er}^{3+})] \quad (\text{iii})$$

$$[{}^4I_{15/2}(\text{Er}^{3+}), {}^4F_{9/2}(\text{Yb}^{3+})] \rightarrow [{}^2F_{7/2}(\text{Yb}^{3+}), {}^4G_{11/2}(\text{Er}^{3+})] \quad (\text{iv})$$

In addition, the ions at the ${}^4G_{11/2}$ energy state of Er^{3+} depopulate to metastable ${}^2H_{9/2}$, ${}^4F_{7/2}$, ${}^4S_{3/2}$, and ${}^4F_{9/2}$ energy states through non-radiative transition while Er^{3+} ions in the ${}^2F_{7/2}$ energy state are transferred non-radiatively to ${}^4F_{9/2}$ energy state through a process called cross-relaxation (CR) energy transfer given by ${}^4F_{7/2} \rightarrow {}^4F_{9/2}$ and ${}^4F_{9/2} \leftarrow {}^4I_{11/2}$ [28, 29]. Eventually, the radiative decay of green and red emission due to ${}^2H_{9/2} \rightarrow {}^4I_{15/2}$, ${}^4F_{7/2} \rightarrow {}^4I_{15/2}$, ${}^4S_{3/2} \rightarrow {}^4I_{15/2}$ and ${}^4F_{9/2} \rightarrow {}^4I_{15/2}$ transitions at 410, 480, 545 and 660 nm are observed.

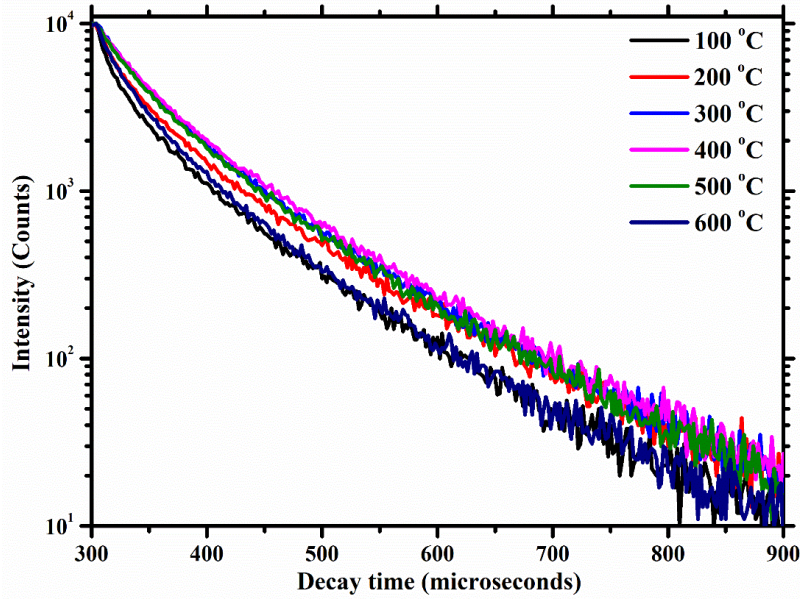


Figure 8.10: Photoluminescence decay curves of $\text{ZnTiO}_3:\text{Er}^{3+}, \text{Yb}^{3+}$ thin films at the emission centred at 547 nm.

Photoluminescence decay curve measurements for $\text{ZnTiO}_3:\text{Er}^{3+}, \text{Yb}^{3+}$ thin films fabricated at different temperatures, were recorded after exciting the sample with a 980 nm LED laser beam (Fig. 8.10). For these measurements, the 547 nm PL emission peak was monitored. The decay curves were fitted with the third exponential function and the average photoluminescent lifetime was estimated using Eq 2 [30]:

$$\tau_{\text{avg}} = \frac{\int t \cdot I(t) \cdot dt}{\int I(t) \cdot dt} \quad [8.1]$$

where I is the photoluminescent intensity and $I(t)$ is the photoluminescent intensity at time t . The average decay lifetimes of the samples were estimated and shown in Table 8.1. With the increase in substrate temperature, the lifetime of the luminescence emission increased up to the thin film fabricated at 500°C, and then decreased.

Table 8.1: Luminescence lifetimes of ZnTiO₃:Er³⁺,Yb³⁺ thin films fabricated at different temperatures

Substrate	$\tau_1(\mu\text{s})$	$\tau_2(\mu\text{s})$	$\tau_3(\mu\text{s})$	$\tau_{\text{avg}}(\mu\text{s})$
Temperature (°C)				
100	26	99	229	118
200	27	95	253	125
300	29	90	270	130
400	28	106	284	139
500	28	109	328	155
600	26	97	295	139

8.4. Conclusion

ZnTiO₃:Er³⁺,Yb³⁺ films deposited at different silicon substrate temperatures were prepared by pulsed laser deposition. The reflectance of the films is increasing with an increase in Si substrate temperature. Further increase in substrate temperature enriches the inter-diffusion process between Si and the ZnTiO₃ during the deposition which decreases the thickness of the films in the prepared samples. The results indicate that the Er³⁺ and Yb³⁺ ions are homogeneously distributed in the ZnTiO₃ host lattice. The luminescence properties of optimized ZnTiO₃:Er³⁺,Yb³⁺ films which deposited at a substrate temperature of 500 °C are superior as compared to other films. These studies revealed that optimized film can be used as a promising material for photovoltaic cells.

8.5. References

- [1] D. Prasanth, K.P. Sibin and H.C. Barshlia. *Thin Solid Films* **673** (2019) 78 – 85.
- [2] J. Yu, D. Li, L. Zhu and X. Xu. *J. Alloys Compd.* 681 (2016) 88 – 95.
- [3] S. Stojadinovic, N. Tadic and R. Vasilic. *J. Lumin.* **208** (2019) 296 – 301.
- [4] R. Tomala, K. Grzeszkiewicz, D. Hreniak and W. Strek. *J. Lumin.* **193** (2018) 70 – 72.
- [5] J. Yu, D. Li, L. Zhu and X. Xu. *J. Alloys Compd.* **681** (2016) 88 – 95.
- [6] K. Cherifi, A. Cheknane, A. Benghia, H.S. Hilal, K. Rahmoun, B. Benyoucef and S. Goumri-Said. *Mater. Today Energy* **13** (2019) 109 – 118.
- [7] M.B. de la Moraa, O. Amelines-Sarriab, B.M. Monroyd, C.D. Hernandez-Pereze and J.E. Lugo. *Sol. Energy Mater. Sol. Cells* **165** (2017) 59 – 71.
- [8] J.M.M. Buarque, D. Manzani, S.L. Scarpari, M. Nalin, S.J.L. Ribeiro, J. Esbenshade, M.A. Schiavon and J.L. Ferrari. *Mater. Res. Bull.* **107** (2018) 295 – 307.
- [9] G. Han, M. Wang, D. Li, J. Bai and G. Diao. *Sol. Energy Mater. Sol. Cells* **160** (2017) 54 – 59.
- [10] Y. Yan, H. Gao, J. Tian, F. Tan, H. Zheng and W. Zhang. *Ceram. Int.* **45** (2019) 11309 – 11315.
- [11] A. Sahu, R. Chaurashiya, K. Hiremath and A. Dixit. *Sol. Energy* **163** (2018) 338 – 346.
- [12] R.S. Raveendra, P.A. Prashanth, R.H. Krishna, N.P. Bhagya, B.M. Nagabhushana, H.R. Naika, K. Lingaraju, H. Nagabhushana and B.D. Prasad. *J. Asian Ceram. Soc.* **2** (2014) 357 – 365
- [13] K. Lemanski, M. Babij and P.J. Deren. *Solid State Sci.* **94** (2019) 127 – 132.
- [14] Zhe Shen, H. Li, H. Hao, Z. Chen, H. Hou, G. Zhang, J. Bi, S. Yan, G. Liu and W. Ga. *J. Photochem. Photobiol., A* **380** (2019) 111864.
- [15] D. Kasprowicz, A. Chiasera, A. Chappini, L. Zur, J. Gapinski, M. Chrunik, A. Majchrowski, R. Jastrzab and M. Ferrari. *Opt. Mater.* **88** (2019) 366 – 371.
- [16] T.P. Mokoena, E.C. Linganiso, H.C. Swart, V. Kumar and O.M. Ntwaeaborwa. *Ceram.*

Int. **43** (2017) 174 – 181.

[17] E.H.H.Hasabeldaim, O.M.Ntwaeaborwa, R.E.Kroon, E.CoetseeaH.C.Swart. *Superlattices Microstruct* **139** (2020) 106432 – 106440.

[18] A. Balakrishna, M.M. Duvenhage and H.C. Swart. *Vacuum* **157** (2018) 376 – 383.

[19] A. Shongalova, M.R. Correia, J.P. Teixeira, J.P. Leitao, J.C. González, S. Ranjbar, S. arud, B. Vermang, J.M.V. Cunha, P.M.P. Salome and P.A. Fernandes. *Sol. Energy Mater. Sol. Cells* **187** (2018) 219 – 226.

[20] D. Prasanth, K.P. Sibin and H.C. Barshilia. *Thin Solid Films* **673** (2019) 78 – 85.

[21] I. Soltani, S. Hraiech, K. Horchani-Naifer and M. Ferid. *Opt. Mater.* **77** (2018) 161 – 169.

[22] R. Elleuch, R. Salhi, J.-L. Deschanvresc and R. Maalej. *RSC Adv.* **5** (2015) 60246.

[23] A.J.M. Sales, D.G. Sousa, H.O. Rodrigues, M.M. Costa, A.S.B. Sombra, F.N.A. Freire, M.J. Soares, M.P.F. Graça and J. Suresh Kumar. *Ceram. Int.* **42** (2016) 6899 – 6905.

[24] X. Wang, P. Li, M.G. Brik, X. Li, L. Li and M. Peng. *J. Lumin.* **206** (2019) 84 – 90.

[25] P.S. Shewale, S.H. Lee and Y.S. Yu. *J. Alloys Compd.* **744** (2018) 849 – 858.

[26] T.P. Mokoena, E.C. Liganiso, V. Kumar, H.C. Swart, S.H. Cho and O.M. Ntwaeaborwa. *J. Colloid Interface Sci.* **496** (2017) 87 – 99.

[27] Y. Ma, G. Xiang, J. Zhang, Z. Liu, P. Zhou, W. Liu, X. Tang, S. Jiang, X. Zhou, L. Li, Y. Luo and Y. Jin. *J. Alloys Compd.* **769** (2018) 325 – 331.

[28] S. Liu, S. Liu, M. Zhou, X. Ye, D. Hou and W. You. *RSC Adv.* **7** (2017) 36935 – 36948.

[29] X. Cheng, X. Ma, H. Zhang, Y. Ren, and K. Zhu. *Physica B* **521** (2017) 270 – 274.

[30] J. Zhang, Y. Dai, B. Liu and B. Han. *Optik* **172** (2018) 1129 – 1133.

Chapter 9: Al³⁺ charge compensation in ZnTiO₃:Eu³⁺ phosphor synthesized by conventional solid-state reaction method

9.1. Introduction

The down-converted luminescence materials have attracted considerable attention in the field of research with variable applications in light emitting diodes (LEDs), solar spectrum conversion in photovoltaic cells and bioimaging owing to their exceptional luminescence efficiency [1- 4]. Down-conversion (DC) of luminescence is a phenomenon in which the materials absorb a single high energy photon and give emission of a lower energy photon. The DC process obeys Stoke's law known as Stokes shift which includes quantum-cutting (QC) and down-shifting (DS) processes [5]. Recently, ZnTiO₃ has been of great interest because of its wide bandgap, unique chemical and physical properties, which make it applicable for down-converted luminescence applications when doped with a suitable rare-earth (RE) ion [6, 7]. An example of such rare-earth ions includes the trivalent europium (Eu³⁺) ions, which efficiently converts ultraviolet photons to an emission that is in the visible range. When Eu³⁺ is incorporated into the lattice, it occupies the non-centrosymmetric sites, and it gives a strong red emission corresponding to the ⁵D₀ → ⁷F_n (n = 0, 1, 2, 3, 4) transition [8].

The ⁵D₀ → ⁷F₂ emission transition is known as a hypersensitive transition with sharp emission lines in the visible region of the electromagnetic spectrum. According to the literature, the intensity of ⁵D₀ → ⁷F₂ transition depends on the symmetry of the crystal field around the Eu³⁺ ion. As a result, the ⁵D₀ → ⁷F₂ transition is more intense when Eu³⁺ ions are located at site without inversion in the host lattice [8 - 10]. According to Rahimian et al., the ⁵D₀ → ⁷F₁ transition is a magnetic dipole transition and it is strongly dependent on the symmetry of the local site of the lattice where Eu³⁺ ions are substituted [8]. The Eu³⁺ doped ZnTiO₃ has successfully been explored in photocatalysis as indicated by Mengting et al. [11]. Herein, we prepared ZnTiO₃:Eu³⁺ phosphor co-doped with a charge compensator (Al³⁺) to enhance its luminescence emission intensity. Aluminium (Al³⁺) cation is a suitable charge compensator

because it enhances the luminescence of activators. Taking into account the excellent luminescent properties and optical responses, $\text{ZnTiO}_3:\text{Eu}^{3+},\text{Al}^{3+}$ phosphor should improve the spectral modifications for solar cells applications by means of down-converting process [12-14].

The utilization of a DC process composed of RE doped phosphors has been introduced into solar cells to improve their power conversion efficiency. The DC phosphor incorporated in a solar cell play a vital role due to their outstanding photoluminescence at different emission wavelengths. This process is achieved by enlarging the range of the electromagnetic waves that can be absorbed from the solar radiation by down-converting or shifting the spectrum into the region that is absorbable by the solar cells [15 - 19]. Most importantly, down-converting or shifting phosphor materials are normally situated on the front side of the light absorption layer in order to absorb ultraviolet light and be induced to generate more photons that can be absorbed and utilized by photosensitive layer to generate more electrons. The DC layer have been applied in majority of conventional photovoltaic cells such as dye sensitized solar cells, quantum dot-sensitized solar cells and silicon solar cells. The advantage of using down-conversion and shifting processes in photovoltaic cells is to minimize the excess of high energy photons of absorption layer that is lost to lattice thermalization [16, 20]. The mechanism of DC in solar cells can be investigated through materials doped with single RE ions or via energy transfer processes between RE ions. This research is aimed at studying the effect of Al^{3+} charge compensation in the Eu^{3+} doped ZnTiO_3 . The Eu^{3+} characteristic emission lines from the green to red emitting electron transitions were successfully observed. The corresponding luminescent mechanism was proposed.

9.2. Experimental results

$\text{ZnTiO}_3:\text{Eu}^{3+},\text{Al}^{3+}$ phosphor powders were synthesized by the conventional solid-state reaction method. The starting materials were commercial ZnO (99.9%), TiO_2 (99.7%), $\text{Eu}(\text{NO}_3)_3 \cdot 5\text{H}_2\text{O}$ (99.9%) and $\text{Al}(\text{NO}_3)_3 \cdot 9\text{H}_2\text{O}$ (99.9%), respectively. In a typical preparation, stoichiometric amounts of ZnO (1.00 g) and TiO_2 (0.98 g) were first mixed and ground together with a ball miller for 1 hour, at room temperature. Different masses of europium nitrate were incorporated to the ball milled powder and mixed using a pestle and mortar. Similarly, with different masses of aluminium nitrate for the co-doped samples. The resulting milled powders were further calcined at 800 °C for 3 hours in air. The calcined powders were ground into fine powders.

9.3. Results and discussion

9.3.1. Morphological and structural analysis

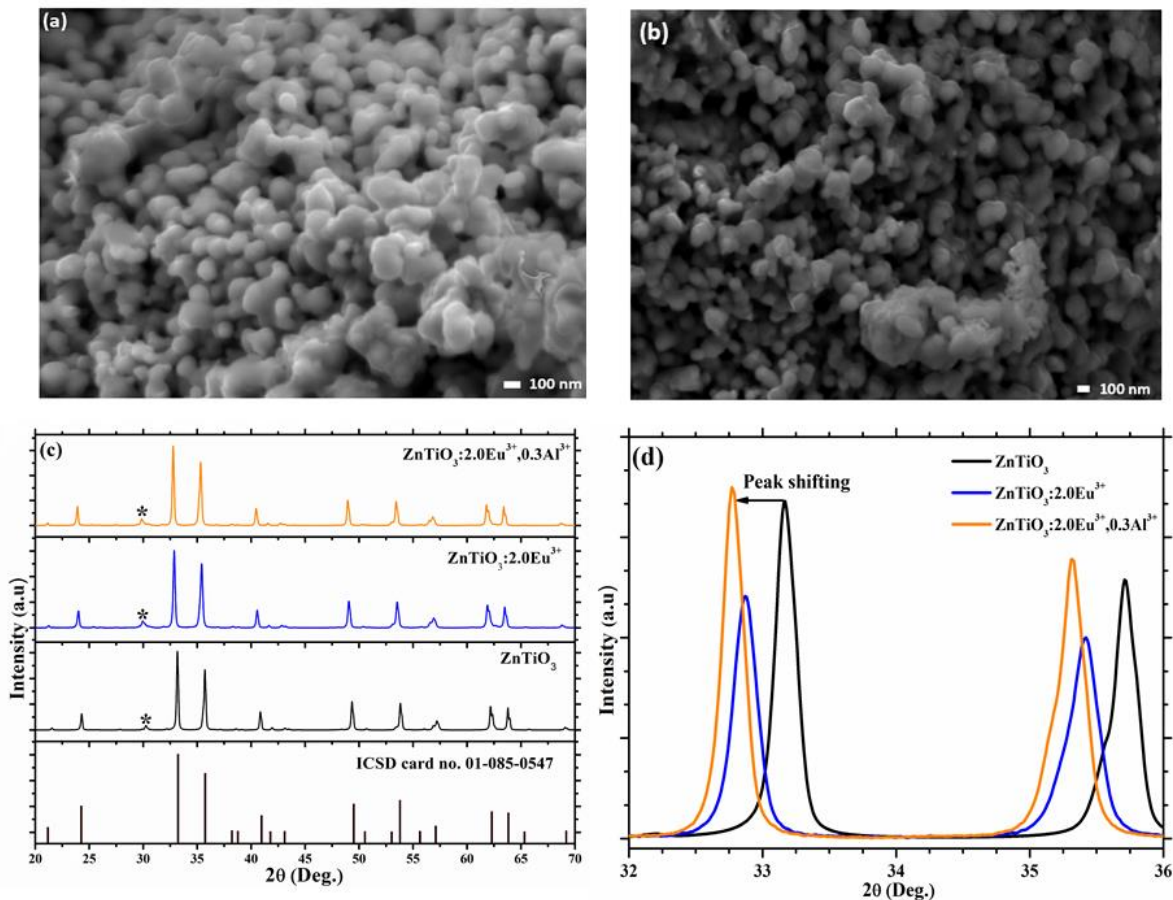


Figure 9.1: FE-SEM image of (a) ZnTiO_3 and (b) $\text{ZnTiO}_3:\text{Eu}^{3+},\text{Al}^{3+}$; (c) XRD patterns of undoped, Eu^{3+} doped and $\text{Eu}^{3+}/\text{Al}^{3+}$ co-doped ZnTiO_3 annealed at 800°C and (d) close inspection of the XRD patterns.

The SEM images of ZnTiO_3 and $\text{ZnTiO}_3:\text{Eu}^{3+},\text{Al}^{3+}$ annealed at 800°C are shown in Fig. 9.1 (a) and (b), respectively. The two images show particles that are of irregular shape, with the same sizes, and are agglomerated due to high calcination temperature [21]. It is clear from the images that the incorporation of Eu^{3+} and Al^{3+} ions has no effect on the surface morphology of ZnTiO_3 . Fig. 9.1 (c) shows the x-ray diffraction patterns of ZnTiO_3 without and with dopant ions. All the diffraction peaks of the samples match with the standard eandrewsite ZnTiO_3 (ICSD card No. 01-085-0547), suggesting that a single phase of the compound was obtained. The diffraction peaks found at $2\theta = 30.2^\circ$ (marked with asterisk *) is relating to secondary phase similar to hexagonal (wurtzite) structure of pure (112) ZnTiO_3 (JCPDS No. 26-1500)

indicating the wurtzite composition [22]. In addition, there are no traces of extra peaks in the XRD profiles of the doped and co-doped systems and this is an indication that Eu^{3+} and Al^{3+} ions were successfully incorporated into the ZnTiO_3 host lattice without the formation of secondary phases. Since the ionic radius of Eu^{3+} is much larger than the radius of Zn^{2+} , partial Eu^{3+} ions substitutes the lattice sites of Zn^{2+} ions, resulting in a lower-angle-shift of the diffraction peaks [23]. At a closer look at the XRD peaks (Fig. 1d) 2θ angle around 33° and 35° , there is a small shift to lower angles with the incorporation of Eu^{3+} and Al^{3+} , and this is in line with Vegard's theory [24]. Since the ionic radius of Eu^{3+} is much larger than the radius of Zn^{2+} , partial Eu^{3+} ions substitutes the lattice sites of Zn^{2+} ions, resulting in a lower-angle-shift of the diffraction peaks [24].

9.3.2. Optical properties analysis

Fig. 9.2 (a) shows the luminescence spectra of Eu^{3+} activated ZnTiO_3 phosphor, with varied Eu^{3+} concentrations. The spectra exhibit five emission peaks located at 578, 590, 611, 650 and 702 nm which correspond to ${}^5\text{D}_0 \rightarrow {}^7\text{F}_0$, ${}^5\text{D}_0 \rightarrow {}^7\text{F}_1$, ${}^5\text{D}_0 \rightarrow {}^7\text{F}_2$, ${}^5\text{D}_0 \rightarrow {}^7\text{F}_3$ and ${}^5\text{D}_0 \rightarrow {}^7\text{F}_4$ transitions of Eu^{3+} ions, respectively [25, 26]. The yellow emission from ${}^5\text{D}_0 \rightarrow {}^7\text{F}_1$ ($\Delta J = \pm 1$) transition located at 590 nm is a magnetic dipole allowed transition whose intensity does not easily influenced by the crystal field strength while the intense red emission from ${}^5\text{D}_0 \rightarrow {}^7\text{F}_2$ ($\Delta J = \pm 2$) transition at 611 nm is due to electric dipole allowed transition with hypersensitive nature whose intensity is strongly sensitive to the local environment of Eu^{3+} ion sites [27, 28]. In addition, Eu^{3+} ions normally occupy a site with inversion symmetry when the emission peak from the ${}^5\text{D}_0 \rightarrow {}^7\text{F}_1$ transition is the most intense and occupy a site without symmetry when the emission arising from the ${}^5\text{D}_0 \rightarrow {}^7\text{F}_2$ transition is the most prominent emission in the host. Fig. 9.2 (a) shows that the ${}^5\text{D}_0 \rightarrow {}^7\text{F}_2$ transition emission is the most intense and stronger than the emission resulting from the ${}^5\text{D}_0 \rightarrow {}^7\text{F}_1$ transition, indicating that the Eu^{3+} ions are located in a site without inversion symmetry in the ZnTiO_3 lattice [26]. The luminescence intensity was enhanced by increasing Eu^{3+} concentration up to 2 mol% and then gradually decreased as a result of concentration quenching effect [25]. The concentration quenching effect occurs as a result of energy transfer between activator and host lattice or nonradiative energy transfer among rare-earth ions, which is mainly caused by several factors such as excitation energy migration, multipole–multipole interaction cross relaxation, radiation reabsorption among others [27-30]. The inset in Fig. 9.2 (a) shows the variation in relative emission intensity

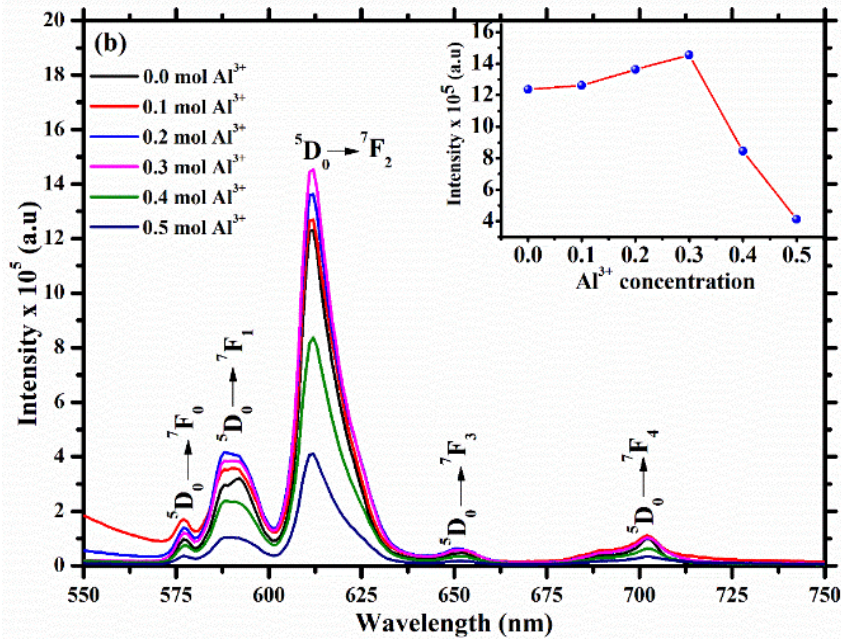
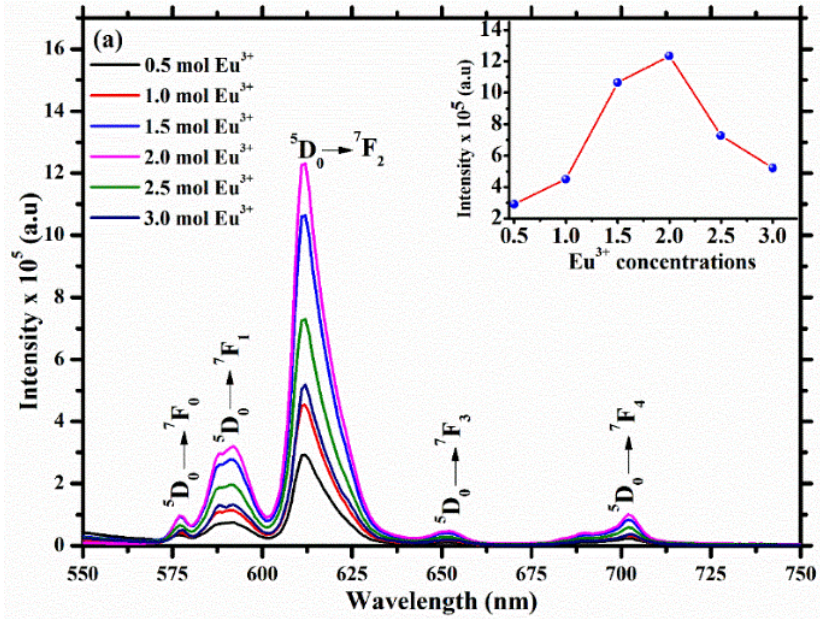


Figure 9.2: PL emission spectra of (a) $\text{ZnTiO}_3:\text{xmol}\%\text{Eu}^{3+}$ and (b) $\text{ZnTiO}_3:2.0\text{mol}\%\text{Eu}^{3+}, \text{xmol}\%\text{Al}^{3+}$.

as a function of concentration of Eu^{3+} ions in ZnTiO_3 lattices. In order to evaluate the mechanism of concentration quenching of the $\text{ZnTiO}_3:\text{Eu}^{3+}$ the separation between the Eu^{3+} ions were calculated using the following equation given by Blasse [31]:

$$R_{\text{Eu}} = 2 \left(\frac{3V}{4\pi X_c N} \right)^{\frac{1}{3}} \quad [9.1]$$

where R_{Eu} is the critical distance between the Eu^{3+} ions, V represents the unit cell volume of $ZnTiO_3$ ($V = 31.1095 \text{ nm}^3$), X_c represents the dopant concentration corresponding to the highest emission intensity ($X_c = 0.02$) and N is the number of the available sites for the dopants in the unit cell of the $ZnTiO_3$ ($N=6$). The critical distance (R_{Eu}) was calculated to be 1.7 nm for $ZnTiO_3:Eu^{3+}$. When the critical distance between the activator ions is less than the theoretical critical distance ($R_c = 0.5 \text{ nm}$), the exchange interaction mechanism of energy transfer takes place and the multipole-multipole interaction mechanisms takes place if the critical distance is bigger than 0.5 nm [24, 31]. Therefore, the calculated critical distance suggests that multipole-multipole interaction mechanisms of energy transfer was responsible for the concentration quenching of the prepared samples.

Fig. 9.2 (b) shows the emission spectra of $ZnTiO_3:2.0\text{mol}\%Eu^{3+}$, $x\text{mol}\%Al^{3+}$ ($x = 0.1, 0.2, 0.3, 0.4$ and 0.5). The Al^{3+} co-doping did not influence the shape and peak positions of the Eu^{3+} ions, indicating that the emission centre still corresponds to Eu^{3+} ions. What is observed is the change in the luminescent intensity. The emission intensity of the 2.0 mol% of Eu^{3+} increased with an increase in the concentration of the Al^{3+} cations up to 0.3 mol% (see the inset in Fig 9.2 (b)), and then began to decrease. This is because doping only Eu^{3+} ions in the $ZnTiO_3$ host result in the crystallization of electron-positivity defects. However, the role of Al^{3+} in the $ZnTiO_3:2.0\%Eu^{3+}$ phosphor is to serve as a charge compensator to promote a charge balance in the prepared samples by forming electronegativity defects which neutralize the electron-positivity and enhance the Eu^{3+} emission. This means that the Al^{3+} cations occupy and substitute the lattice of Ti^{4+} in the form of Al^{3+} to maintain the charge balance in the $ZnTiO_3:Eu^{3+}$ phosphor by suppressing the defects. As a result, an increase in concentration of charge compensator Al^{3+} in $ZnTiO_3:2.0\text{mol}\%Eu^{3+}$ phosphor generate more electro-negativity defects and gradually decrease the emission intensity of the phosphor at a concentration above 0.3mol% [32, 33].

Fig. 9.3 shows the diffused reflectance spectra of the undoped $ZnTiO_3$ together with luminescence intensity optimized $ZnTiO_3:2\text{mol}\%Eu^{3+}$ and $ZnTiO_3:2\text{mol}\%Eu^{3+},0.3\text{mol}\%Al^{3+}$ phosphors. The spectra of the samples show major absorption at $\sim 287 \text{ nm}$, corresponding to the fundamental band to band electron transition of $ZnTiO_3$ host [35, 36]. In addition, the single doped and co-doped phosphors had absorption bands at ~ 465 and $\sim 534 \text{ nm}$, which correspond to the ${}^7F_0 \rightarrow {}^5D_2$ and ${}^7F_1 \rightarrow {}^5D_1$ transitions of Eu^{3+} ions, respectively [36].

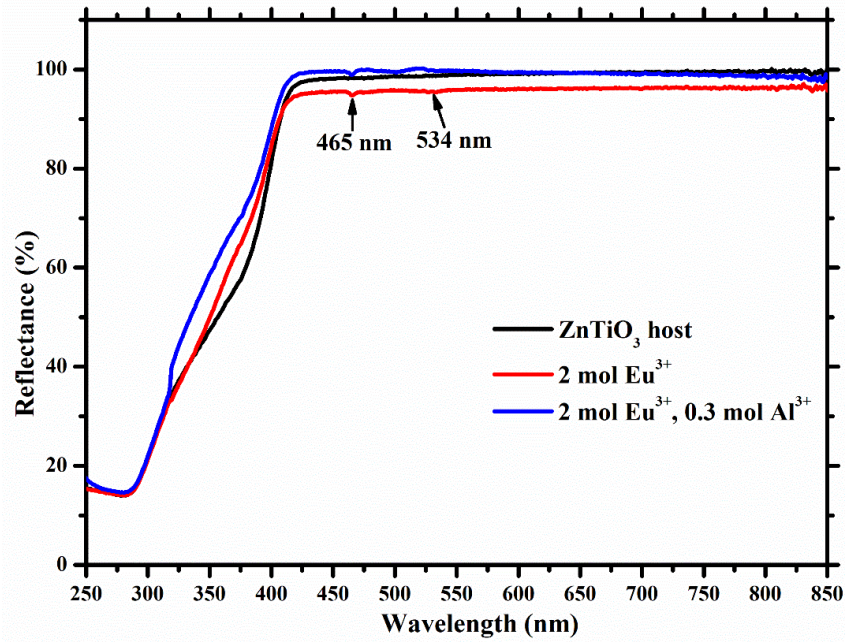


Figure 9.3: The diffuse reflectance spectra of $\text{ZnTiO}_3:\text{Eu}^{3+},\text{Al}^{3+}$ thin films.

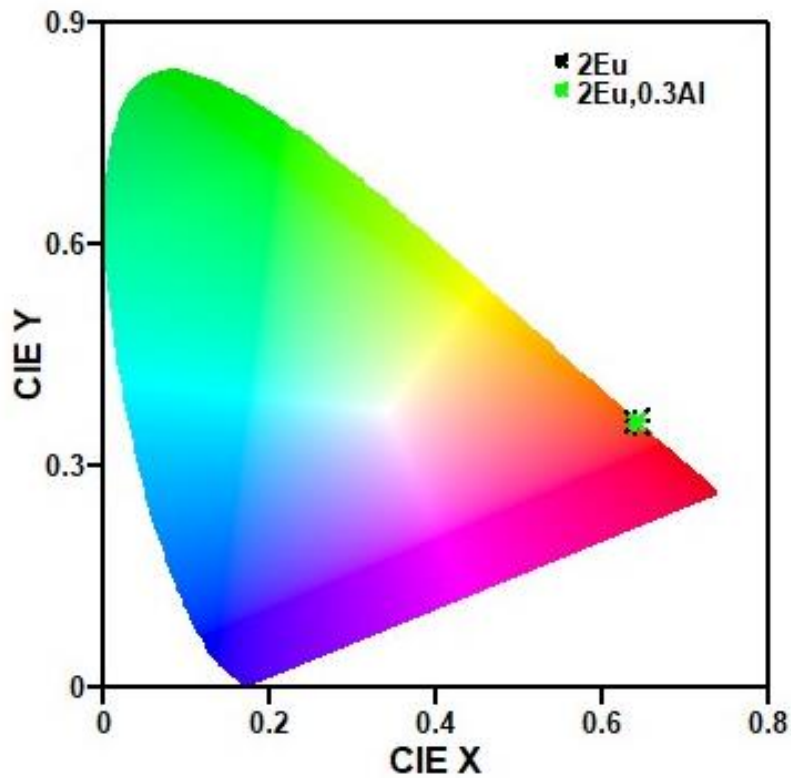


Figure 9.4: The Commission Internationale de l'éclairage (CIE) diagram showing chromaticity points of $\text{ZnTiO}_3:2\text{mol}\%\text{Eu}^{3+}$ and $\text{ZnTiO}_3:2\text{mol}\%\text{Eu}^{3+},0.3\text{mol}\%\text{Al}^{3+}$.

The Commission Internationale de l'Éclairage (CIE) chromaticity coordinates of the ZnTiO₃:2mol% Eu³⁺ and ZnTiO₃:2mol% Eu³⁺,0.3mol%Al³⁺ under the excitation of 395 nm were calculated and shown in Fig. 9.4. The CIE coordinates were calculated to be (0.64, 0.36) for both ZnTiO₃:2mol% Eu³⁺ and ZnTiO₃:2mol% Eu³⁺,0.3mol%Al³⁺ phosphors respectively. The figure shows that the prepared samples exhibit a strong red emission and the position of the CIE coordinates of sample giving the intense emission is closer to the standard red chromaticity of National Television Standard Committee (0.67, 0.33) [38].

The luminescence decay curves of the ZnTiO₃:2.0mol%Eu³⁺ and ZnTiO₃:2.0mol%Eu³⁺,xAl³⁺ samples are shown in in Fig. 9.5 (a) & (b), respectively. The decay curves of the sample were recorded using the ⁵D₀ → ⁷F₂ transition and fitted with a tripple exponential decay function (Eq. 9.2) [39, 40], as shown for ZnTiO₃:2.0mol%Eu³⁺ in Fig. 9.5 (a).

$$I(t) = I_0 + B_1e^{-t/\tau_1} + B_2e^{-t/\tau_2} + B_3e^{-t/\tau_3} \quad [9.2]$$

where I and I_0 are the UC intensities at certain time t and 0 (from background), respectively, t is the time, A_1 , A_2 and A_3 are the fitting parameters, τ_1 , τ_2 and τ_3 are the decay components.

The corresponding decay time parameters for the first, second and third order, are presented in table 9.1. In addition, the average lifetimes (τ) of Eu³⁺ were calculated by using the following relation:

$$\tau_{\text{average}} = \frac{B_1\tau_1^2 + B_2\tau_2^2 + B_3\tau_3^2}{B_1\tau_1 + B_2\tau_2 + B_3\tau_3} \quad [9.3]$$

The corresponding average decay times are presented in Table 9.1. The Al³⁺ co-doped samples had a decay time that was shorter than that of the sample without co-dopant ions. According to Wu et al., this phenomenon is caused by the reduction of the critical distance between Eu³⁺ ions inside the host lattices due to co-doping. The incorporation of Al³⁺ decreases the defects in the ZnTiO₃ host lattice, and this shows that it has an effect on the resonant energy transfer which significantly acts as an additional channel to the non-radiative centres and, so, the luminescence lifetimes decreases [40].

The mechanism of the charge compensator co-doped ZnTiO₃:2mol%Eu³⁺ is illustrated in Fig. 9.6. After the 395 nm excitation wavelength, electrons (e⁻) are excited from its ground state to the excited states of the host matrix; then, return to the defects states of the ZnTiO₃ through a process called non-radiative transition (NR). In this case, there is a charge imbalance for the

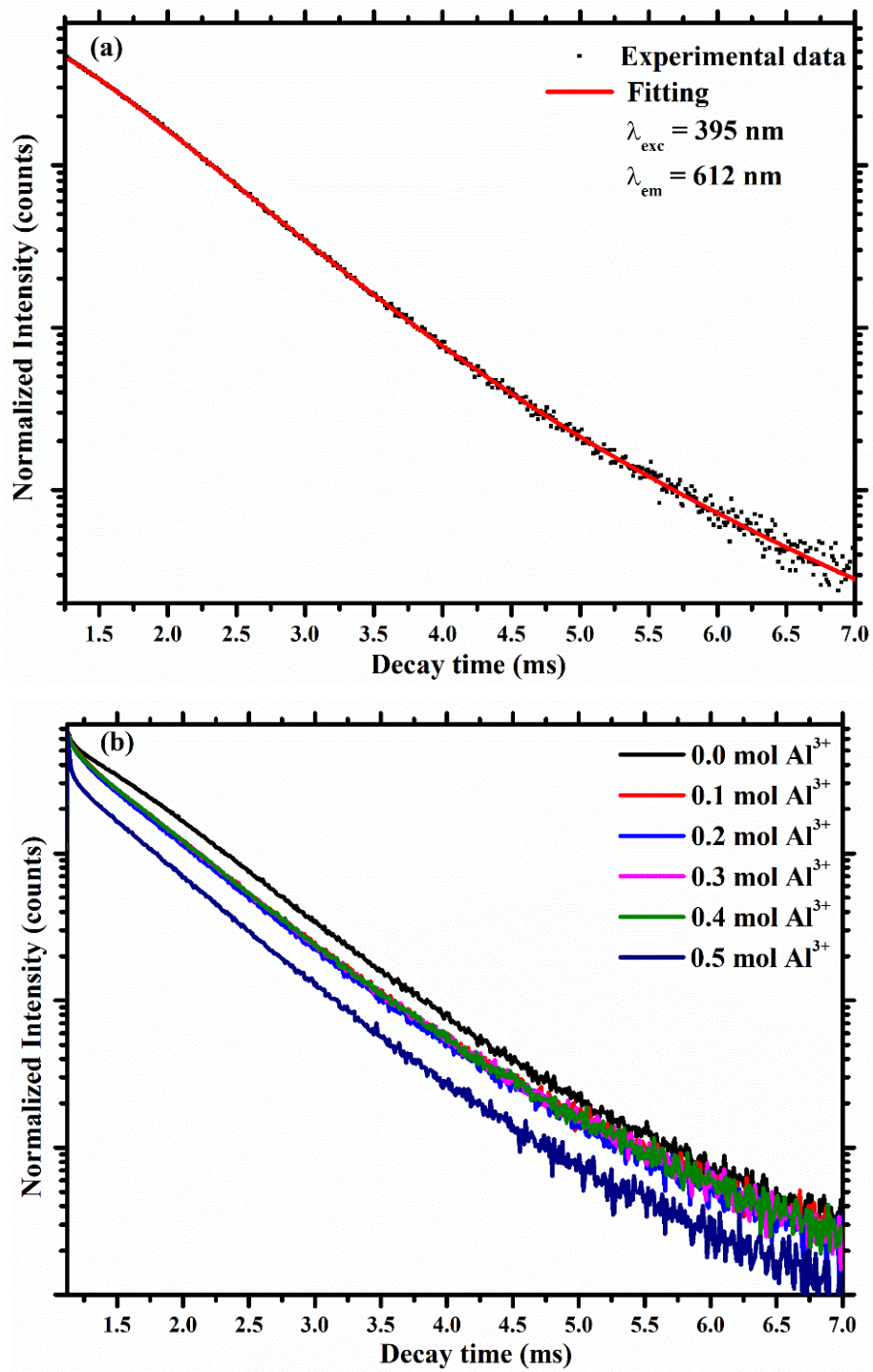


Figure 9.5: Decay curves of the ${}^5D_0 \rightarrow {}^7F_2$ transition in (a) $\text{ZnTiO}_3:\text{Eu}^{3+}$ sample and (b) $\text{ZnTiO}_3:\text{Eu}^{3+}, \text{Al}^{3+}$ samples excited at 395 nm.

Table 9.1: Photoluminescence lifetimes of $\text{ZnTiO}_3:2.0\text{mol}\% \text{Eu}^{3+}$ and $\text{ZnTiO}_3:2.0\text{mol}\% \text{Eu}^{3+}$, $x\text{mol}\% \text{Al}^{3+}$ samples.

Eu^{3+} conc.	Al^{3+} conc.	$\tau_1(\mu\text{s})$	$\tau_2(\mu\text{s})$	$\tau_3(\mu\text{s})$	$\tau_{\text{average}}(\mu\text{s})$
2.0	-	329	659	1318	1639
2.0	0.1	313	626	1252	647
2.0	0.2	309	619	1238	637
2.0	0.3	309	619	1239	849
2.0	0.4	312	625	1251	646
2.0	0.5	292	584	1169	745

$\text{ZnTiO}_3:\text{Eu}^{3+}$ phosphor which generating negative oxygen (O_i'') point defects residing in the forbidden region to neutralize the positive zinc (Zn_i'') point defect. The O_i'' are temporary trapping the holes (h^+) in the valence band and releases them to the ${}^7\text{F}_j$ ($j = 0, 1, 2, 3$ and 4) states. On the other hand, the Zn_i'' trap the electron (e^-) and release them from the conduction band. This process lead to the generation of the negative zinc vacancies (V_{Zn}'') that trap and hold h^+ and the oxygen vacancies (V_o'') which tend to trap and release the carriers. The carriers trapped by V_{Zn}'' are then released from its ground state to recombine with Zn_i'' from the excited states of the host matrix through a process called non-radiative recombination. However, incorporation of the charge compensator Al^{3+} tends to compensate these defects in the $\text{ZnTiO}_3:\text{Eu}^{3+}$ by suppressing the effect of non-radiative process after occupying the Ti^{4+} positions. The reduced non-radiative transition is due to Al^{3+} charge compensation process that ensures more supply of carriers to the Eu^{3+} centres. In addition, the reduction of the defects in the system enhances the energy transfer process from the host defects level to the excited states of Eu^{3+} because there will now be less amount of defects being quenched by the Al^{3+} charge compensator and transfer more electrons to Eu^{3+} states. The electrons at the highest excited state return to the lowest excited state ${}^5\text{D}_0$ of Eu^{3+} ions via a non-radiative transition and therefore finally decay to ${}^7\text{F}_j$ states where $j = 0, 1, 2, 3$ and 4 . Though there is a reduction of amount of defects in the system due to incorporation of Al^{3+} co-dopant, the emission intensity of $\text{ZnTiO}_3:\text{Eu}^{3+}$ is enhanced [1, 41].

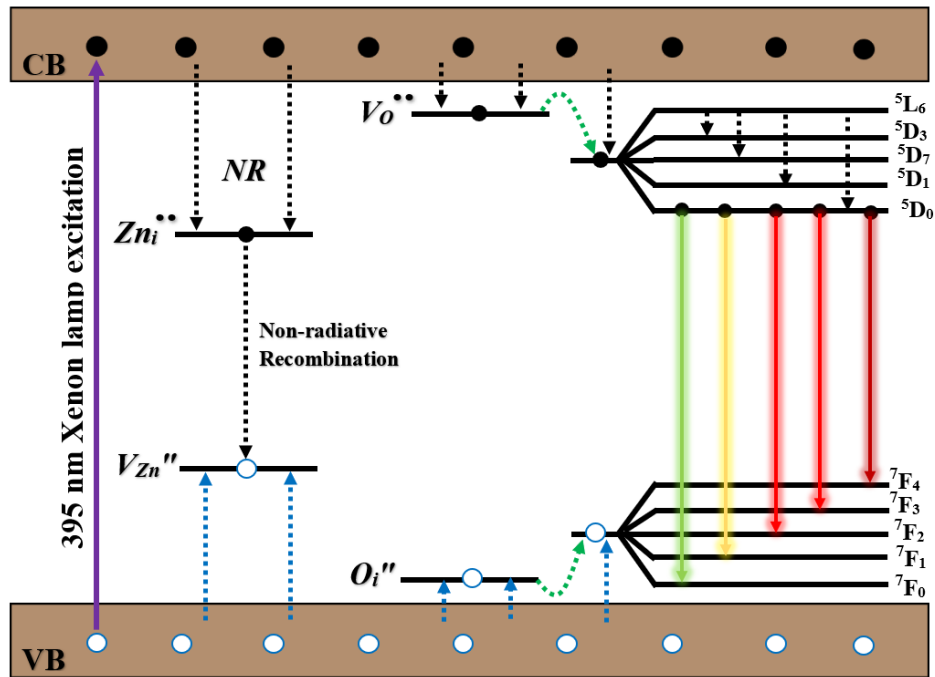


Figure 9.6: Schematic energy level diagram of ZnTiO₃:Eu³⁺, Al³⁺ which is not drawn to scale.

9.4. Conclusion

In summary, the ZnTiO₃:Eu³⁺, Al³⁺ samples were successfully synthesized using conventional solid-state reaction method. Eu³⁺ ions locate in a site without inversion symmetry when incorporated in the ZnTiO₃ lattice. The ZnTiO₃:Eu³⁺ samples show intense red emission under 395 nm excitation. The multipole-multipole interaction mechanisms of energy transfer were effective for the concentration quenching. From optical properties, it was observed that the visible emission of Eu³⁺ has enhanced due to the effective aluminium (Al³⁺) charge compensator inside the host ZnTiO₃:Eu³⁺. The optimum concentration of charge compensator in ZnTiO₃:Eu³⁺ was observed to be 0.3 mol%. The lifetime of these phosphors decreased by the incorporation of charge compensator due to reduced defects. Hence the prepared samples could serve as a promising candidate for down-converting UV region.

9.5. References

- [1] D.C. Arantes, C. de Mayrinck, J.D. Santos, L.F. Maia, L.F.C. Oliveira, M.A. Schiavon, D. Pasquini, R.C. de Lima, L.C. de Moraes, J. Esbenshade and J.L. Ferrari. *Opt. Mater.* **88** (2019) 522 – 533.
- [2] A. Verma and S.K. Sharma. *Ceram. Int.* **43** (2017) 8879 – 8885.
- [3] J.M.M. Buarque, D. Manzani, S.L. Scarpari, M. Nalin, S.J.L. Ribeiro, J. Esbenshade, M.A. Schiavon and J.L. Ferrari. *Mater. Res. Bull.* **107** (2018) 295 – 307.
- [4] P.S. David, P. Panigrahi and G.S. Nagarajan. *Mater. Lett.* **249** (2019) 9 – 12.
- [5] M. Hanioka, S. Arimoto and H. Samata. *Optik* **154** (2018) 226–233
- [6] J. Yu, D. Li, L. Zhu and X. Xu. *J. Alloys Compd.* **681** (2016) 88 – 95.
- [7] Y. Yan, H. Gao, J. Tian, F. Tan, H. Zheng and W. Zhang. *Ceram. Int.* **45** (2019) 11309 – 11315.
- [8] H. Rahimian, H. Mokhtari and S. P. Shirmardi. *J. Lumin.* **187** (2017) 535 – 539.
- [8] M.S. Niasari, F. Soofivand, A.S. Nasab, M.S. Arani, A.Y. Faal and S. Bagheri. *Adv. Powder Technol.* **27** (2016) 2066 – 2075.
- [9] J. Zhao, L. Huang, T. Liang, S. Zhao and S. Xu. *J. Lumin.* **205** (2019) 342–345.
- [10] Y. Bu and X. Yan. *J. Lumin.* **190** (2017) 50–55.
- [11] L. Mengting and J. Baoxiang. *J. Rare Earths* **33(3)** (2015) 231 – 238.
- [12] Y. Zuo, W. Ling and Y. Wang. *J. Lumin.* **132** (2012) 61 – 63.
- [13] X. Xu, Y. Tang, F. Mo and L. Zhoun, B. Li. *Ceram. Int.* **40** (2014) 10887 – 10892.
- [14] S.J. Yoon, J.W. Pi and K. Park. *Dyes Pigm.* **150** (2018) 231 – 240.
- [15] L. Wang, W. Guo, H. Hao, Q. Su, S. Jin, H. Li, X. Hu, L. Qin, W. Gao and G. Liu. *Mater. Res. Bull.* **76** (2016) 459 – 465.
- [16] X. Hou, T. Xuan, H. Sun, X. Chen, H. Li and L. Pan. *Sol. Energ. Mat. Sol. C.* **149** (2016) 121–127.

- [17] V. Kumar, S.K. Swami, A. Kumar, O.M. Ntwaeaborwa, V. Dutta and H.C. Swart. *J Colloid. Interf. Sci.* **484** (2016) 24 – 32.
- [18] S.K. Karunakaran, C. Lou, G.M. Arumugam, C. Huihui and D. Pribat. *J. Sol. Energy* **188** (2019) 45 – 50.
- [19] J.A.M. Garciaa, L. Bontempo, L.A. Gomez-Malagon and L.R.P. Kassa. *Opt. Mater.* **88** (2019) 155 – 160.
- [20] D. Fang, X. Zhang, C. Zhao, X. Liu, X. Shu and J. Wang. *Opt. Mater.* **88** (2019) 80–90.
- [21] S.W. Oh, H.J. Bang, Y.C. Bae and Y.K. Sun. *J. Power Sources* **173** (2007) 502 – 509.
- [22] H. Jahangiri and M. L. Öveçoğlu. *Mater.* **178** (2016) 193 – 196.
- [23] O.M. Ntwaeaborwa, S.J. Mofokeng, V. Kumar and R.E. Kroon. *Spectrochim. Acta, Part A* **182** (2017) 42 – 49.
- [24] M.S. Mendhe, S.P. Puppalwar and S.J. Dhoble. *Opt. Mater.* **82** (2018) 47 – 55.
- [25] K. Park, D.A. Hakeem, J.W. Pi and G.W. Jung. *J. Alloys Compd.* **772** (2019) 1040 – 1051.
- [26] Z. Wang, P. Li, Z. Yang and Q. Guo. *Opt. Commun.* **321** (2014) 100 –103.
- [27] M. De, S. Sharma and S. Jana. *Physica B* **556** (2019) 131 – 135.
- [28] D. Komaraiah, E. Radha, J. James, N. Kalarikkal, J. Sivakumar, M.V. R. Reddy and R. Sayanna. *J. Lumin.* **211** (2019) 320 – 333.
- [29] A.I. De Vries, J.P.M. Van Vliet and G. Biasse. *Phys. Status Solidi B* **149** (1988) 391 – 401.
- [30] S. Sun, L. Wu, H. Yi, L. Wu, J. Ji, C. Zhang, Y. Zhang, Y. Kong and J. Xu. *Opt. Mater. Express* **6(4)** (2016) 1172 – 1185.
- [31] C. Wang, J. Jiang, J. Wang, S. Xin, Y. Shi and G. Zhu. *J. Lumin.* **215** (2019) 116606.
- [32] Y. Wu, M. Chen, K. Qiu, W. Zhang, and Q. Tang. *Opt. Laser Technol.* **118** (2019) 20 – 27.
- [33] B. Ozturk and G.S.P. *Ceram. Int.* **42** (2016) 11184 – 11192.

- [34] R.S. Raveendra, P.A. Prashanth, R.H. Krishna, N.P. Bhagya, B.M. Nagabhushana, H.R. Naika, K. Lingaraju, H. Nagabhushana and B.D. Prasad. *J. Asian Ceram. Soc.* **2** (2014) 357 – 65.
- [35] I.I. Kindrat, B.V. Padyak, B. Kukliński, A. Drzewiecki and V.T. Adamiv. *J. Lumin.* **204** (2018) 122 – 129.
- [36] C. Liu, Z. Zhou and Y. Zhang. *J. Alloys Compd.* **787** (2019) 1158 – 1162.
- [37] D.V.K. Reddy, Sk Taherunnisa, A.L. Prasanna, T.S. Rao, N. Veeraiah and M. Rami Reddy. *J. Mol. Struct.* **1176** (2019) 133 – 148.
- [38] X. Tian, G. Jiang, Y. Chen and M. Yin. *Curr. Appl Phys.* **14** (2014) 1612 – 1615.
- [39] Y. Wu, K. Qiu, Q. Tang, W. Zhang and J. Wanga. *Ceram. Int.* **44** (2018) 8190 – 8195.
- [40] S.K.L. Devi, K.S. Kumar and A. Balakrishnan. *Mater.* **65** (2011) 35 – 37.
- [41] L.L. Noto, S.S. Pitale, M.A. Gusowki, J.J. Terblans, O.M. Ntwaeaborwa, H.C. Swart, , *Powder Technol.* **237** (2013) 141–146.

Chapter 10: Summary and Future work

10.1. Summary

The thesis report the up and down-conversion luminescence properties of $\text{ZnTiO}_3\text{-Zn}_2\text{TiO}_4\text{:Er}^{3+}$ composites, $\text{ZnTiO}_3\text{:Er}^{3+}, \text{Yb}^{3+}$ and $\text{ZnTiO}_3\text{:Eu}^{3+}, \text{Al}^{3+}$ for photovoltaic application. The main aim of the research was to study the up and down-conversion mechanisms involved in the prepared phosphors to improve the power conversion efficiency of photovoltaic cells. $\text{ZnTiO}_3\text{-Zn}_2\text{TiO}_4\text{:Er}^{3+}$, $\text{ZnTiO}_3\text{:Er}^{3+}, \text{Yb}^{3+}$ and $\text{ZnTiO}_3\text{:Eu}^{3+}, \text{Al}^{3+}$ phosphors were all prepared by conventional solid-state reaction method with different concentrations of $\text{Er}^{3+}, \text{Yb}^{3+}, \text{Eu}^{3+}$ ions and Al^{3+} cations. The samples were characterized using different techniques such as x-ray diffractometer, field emission scanning electron microscopy, time of flight secondary ion mass spectroscopy, UV-Vis-NIR absorption spectrometer and photoluminescence spectroscopy, respectively.

The $\text{ZnTiO}_3\text{-Zn}_2\text{TiO}_4$ composite phosphor doped with different concentration of Er^{3+} ions were successfully synthesized using conventional solid-state reaction method and annealed at 1100 °C. The morphological properties of the $\text{ZnTiO}_3\text{-Zn}_2\text{TiO}_4$ composite phosphor showed the agglomerations of faceted spheres and hexagons. The charge transfer state that overlaps the band gap was observed from the diffuse reflectance spectra. The phosphors displayed prominent visible green and red emission lines observed at 541–574 nm and 640–690 nm, corresponding to ${}^2\text{H}_{11/2} \rightarrow {}^4\text{I}_{15/2}$, ${}^4\text{S}_{3/2} \rightarrow {}^4\text{I}_{15/2}$ and ${}^4\text{F}_{9/2} \rightarrow {}^4\text{I}_{15/2}$ f-f electronic transitions of Er^{3+} ions. The emission intensity of the green and red emission lines was enhanced with an increase in concentration of Er^{3+} ions, and the 0.8 mol% Er^{3+} gave the most intense emission, respectively. The Commission Internationale de l'Eclairage (CIE) coordinates of the $\text{xmol}\%\text{Er}^{3+}$ indicated that the displayed emission resembled a greenish-yellow colour with a luminescent lifetime of 0.267.4 ms.

A $\text{ZnTiO}_3\text{:Er}^{3+}$ phosphor was prepared using conventional solid-state reaction method and annealed at 800 °C for 3 hours. An eandrewsite single phase of ZnTiO_3 with space group

R-3 (148) was obtained and confirmed by XRD. The morphology of the prepared $\text{ZnTiO}_3:\text{Er}^{3+}$ samples consist of agglomerated and uniform particle shapes due to annealing of the samples at high temperatures. From the luminescence spectra of $\text{ZnTiO}_3:\text{Er}^{3+}$ phosphor, the emission lines corresponding to Er^{3+} transitions were also observed under the excitation wavelength of 980 nm. Furthermore, the luminescence results showed that the nature of the energy transfer mechanism suggested that the cross-relaxation process was the preferred energy transfer between Er^{3+} ions in ZnTiO_3 compound. This compound is a better phosphor compared with the composite due to some impurities scribed to rutile TiO_2 and $\beta\text{-Zn}_2\text{TiO}_4$ phases in the composite phosphor.

The up-conversion luminescence and energy transfer mechanism of $\text{ZnTiO}_3:\text{Er}^{3+},\text{Yb}^{3+}$ phosphor synthesized by conventional solid-state reaction method was investigated and the phosphors were excited by 980 nm. The luminescence results showed the emission bands centred at 410, 480, 545 and 665 nm which are attributed to Er^{3+} ions. An increase in concentration of Yb^{3+} ions intensified the emission intensity of the optimal concentration of Er^{3+} ions and increased the mean lifetime of Er^{3+} , pointing to the occurrence of the efficient energy transfer from Yb^{3+} to Er^{3+} ions. Similarly, the variation of laser power increased the intensity of the emission and did not change the peak positions and shapes, implying the excellent stability of samples under laser excitation energy. The results from UC measurements suggest that the combination of Yb^{3+} and Er^{3+} offer a great advantage as an up-converter over Er^{3+} alone. This was ascribed to an enhanced emission intensities and longer lifetime of the phosphors due to the efficient energy transfer from Yb^{3+} to Er^{3+} ions.

The $\text{ZnTiO}_3:\text{Er}^{3+}, \text{Yb}^{3+}$ thin films phosphor were successfully deposited on silicon substrate using the pulsed laser deposition at different substrate temperature. The particles of the thin films showed large grains which are very segregate embedded on an amalgamate fine grains. Homogeneity of the distribution of ions was investigated by TOF-SIMS and the images indicated the successful incorporation of Er^{3+} and Yb^{3+} ions in ZnTiO_3 compound. Five f-f electronic transitions from Er^{3+} were observed at 410, 480, 525, 545 and 660 nm. The most dominant transition was red emission from ${}^4\text{F}_{9/2} \rightarrow {}^4\text{I}_{15/2}$ transition. The emission intensity and lifetimes of the lumenscence of $\text{ZnTiO}_3:\text{Er}^{3+}, \text{Yb}^{3+}$ thin films were enhanced by an increase in silicon substrate temperature.

A $\text{ZnTiO}_3:\text{Eu}^{3+},\text{Al}^{3+}$ phosphor with red emission was synthesized using conventional solid-

state reaction method. Eucandrewsite phase was obtained as proved by XRD pattern. The surface morphology carried out by SEM shows that the particles were agglomerated, and they were of irregular shapes. The $\text{ZnTiO}_3:\text{Eu}^{3+}$ phosphors show intense red emission at 611 nm which corresponds to the ${}^5\text{D}_0 \rightarrow {}^7\text{F}_2$ transition of Eu^{3+} ion. The multipole-multipole interaction mechanisms of energy transfer were effective for the concentration quenching. Al^{3+} was co-doped in $\text{ZnTiO}_3:\text{Eu}^{3+}$ phosphor to charge compensate and enhance the visible emission of Eu^{3+} by reducing the quantity of defects. The optimum concentration of charge compensator in $\text{ZnTiO}_3:\text{Eu}^{3+}$ was observed to be 0.3 mol% and for higher doping concentration the luminescence intensity quenched. The luminescence lifetime of these phosphors decreased by the incorporation of charge compensator due to reduced defects. The results also demonstrated that the composite phosphor reported in chapter 5 had longer lifetime compared to single phase phosphor reported in chapter 6.

The optical responses of the phosphors investigated revealed that the phosphors exhibited strong absorptions that are attributed to inter-band transitions. Er^{3+} activated $\text{ZnTiO}_3\text{-Zn}_2\text{TiO}_4$ composite and ZnTiO_3 powders showed f-f absorptions of Er^{3+} in the visible region in addition to strong absorption of ZnTiO_3 . Similarly, $\text{ZnTiO}_3:\text{Eu}^{3+}, \text{Al}^{3+}$ phosphors revealed the f-f absorptions of Eu^{3+} in the visible region in addition to strong absorption of ZnTiO_3 . The band gaps were estimated using Kubelka Munk function. When evaluating the effect of Er^{3+} and Yb^{3+} , the band gap of ZnTiO_3 increased, respectively. The luminescence results confirmed a successful up and down-conversion of the phosphors and the energy transfer occurred effectively from Yb^{3+} to Er^{3+} in ZnTiO_3 phosphor.

The $\text{ZnTiO}_3:\text{Er}^{3+}, \text{Yb}^{3+}$ powder samples and $\text{ZnTiO}_3:\text{Er}^{3+}, \text{Yb}^{3+}$ thin films fabricated by the PLD were comparatively investigated. In addition, the results imply that these phosphors are suitable for up conversion improvement of the power conversion efficiency of photovoltaic cells. It was found that the luminescent properties of $\text{ZnTiO}_3:\text{Er}^{3+}, \text{Yb}^{3+}$ thin films showed more emission bands compared to the results obtained for the $\text{ZnTiO}_3:\text{Er}^{3+}, \text{Yb}^{3+}$ powder samples. These luminescence results suggested that the $\text{ZnTiO}_3:\text{Er}^{3+}, \text{Yb}^{3+}$ thin films might be used as an up-converter for the improvement of power efficiency of the solar cell.

10.2. Future work

Efficient up and down-conversion luminescence phosphors-based oxides semiconductors play a crucial role in enhancing the power conversion of a solar cell. There are several parameters

that can be employed and investigated in the up and down-conversion luminescence mechanisms of the phosphor materials. This include the effect of temperature, host matrix, impurity doping, incorporation of charge compensator, lanthanides concentration, sensitizers, activators and photo-physical properties. However, it is imperative to investigate the effects of these parameters and the rate of energy transfer from the sensitizer to activator in a suitable host matrix. Furthermore, the XRD analysis of the phosphors prepared by convectional solid-state reaction in this study showed a successful preparation of a single phase of ZnTiO_3 as a host which was annealed at 800 °C. Further studies at annealing temperature above 800 °C can be done to form spinel Zn_2TiO_4 phase as a host for up and down-conversion luminescence phosphors that is expected to influence the lanthanides concentrations and luminescence properties of lanthanides ions. This would assist in determining which host among ZnTiO_3 and Zn_2TiO_4 can be a good host for up and down-conversion process. The study could also be extended on the energy transfer from Yb^{3+} ion to other up-converting lanthanides ions in order to efficiently up-convert NIR light to visible light. Future work can also include varying the Yb^{3+} concentration (fixed in this study) and incorporate the phosphors into solar cell device to assess the change in power efficiency. The efficiency of the prepared phosphors will be tested by assembling the DSSC with a phosphor/ TiO_2 nanoparticles bilayer electrode. The advantage of this phosphor will be a practical too that contributes highly on enhancing the efficiency of a DSSCs.

10.3. List of publications

- 10.3.1. Odirileng Martin Ntwaeaborwa, **Sefako J. Mofokeng**, Vinod Kumar, Robin E. Kroon. *Structural, optical and photoluminescence properties of Eu^{3+} doped ZnO nanoparticles*. Spectrochimica Acta Part A: Molecular and Biomolecular Spectroscopy. Volume 182, 5 July 2017, Pages 42 – 49.
doi.org/10.1016/j.saa.2017.03.067.
- 10.3.2. **S.J. Mofokeng**, V. Kumar, R.E. Kroon, O.M. Ntwaeaborwa. *Structure and optical properties of Dy^{3+} activated sol-gel ZnO-TiO₂ nanocomposites*. Journal of Alloys and Compounds. Volume 711, 15 July 2017, Pages 121 – 131.
doi.org/10.1016/j.jallcom.2017.03.345.

- 10.3.3. Luyanda L. Noto, **Sefako J. Mofokeng**, Nolufundo Sintwa, Mokgaotsa J. Mochane, Bakang M. Mothudi. *Deriving luminescent materials from seashell waste*. Book Chapter. Volume 1, Published by Nova Science Publishers, Inc New York. Pages 39-59. ISBN:978-1-53613-236-6 (e-book).
- 10.3.4. Kingsley O. Obodo, Luyanda L. Noto, **Sefako J. Mofokeng**, Cecil N.M. Ouma, Moritz Braun, Mokhotjwa S. Dhlamini. *Influence of Tm, Ho and Er dopants on the properties of Yb activated ZnTiO₃ perovskite: a density functional theory insight*. Material Research Express. Volume 5, Number 10, 29 August 2018, Pages 106202 –106212. doi.org/10.1088/2053-1591/aadaf2.
- 10.3.5. **Sefako J. Mofokeng**, Vinod Kumar, Robin E. Kroon, So-Hye Cho, and Odireleng M. Ntwaeaborwa. *Enhanced red emission of Eu³⁺ in ZnO-TiO₂:Dy³⁺, Eu³⁺ nanocomposites by UV downconversion process*. Journal of Vacuum Science & Technology B. Volume 37, 30 January 2019, Pages 022901 – 022909. <https://doi.org/10.1116/1.5081953>.
- 10.3.6. F V Molefe, **S J Mofokeng**, M Khenfouch, M Achehboune, M S Dhlamini, B M Mothudi, and L F Koao. *The effect of Zn²⁺ on the anion vacancies in ZnO thin-films grown using chemical bath deposition*. Journal of Physics: Conference Series. Volume 1292 (2019) Pages 012016 – 012023. doi:10.1088/1742-6596/1292/1/012016.
- 10.3.7. **S.J. Mofokeng**, L.L. Noto, D.V. Mlotswa, V.R. Orante-Barrón, M.S. Dhlamini. *Thermoluminescence properties of MgO:Al³⁺,Li⁺ prepared by microwave assisted solution combustion method*. Physica B: Condensed Matter. Volume 552, 11 January 2020, Pages 412008 – 412016. doi.org/10.1016/j.physb.2020.412008.
- 10.3.8. Luyanda L. Noto, **Sefako J. Mofokeng**, Fokotsa V. Molefe, Angelina S. Tebele, Hendrik C. Swart, Mokhotjwa S. Dhlamini. Book Chapter: *Luminescent Dynamics of Rare Earth doped CaTiO₃ phosphor*. Spectroscopy of Lanthanides Doped Oxide Materials. Woodhead Publishing Series in Electronic and Optical Materials. January 2020, Pages 57– 86, doi.org/10.1016/B978-0-08-102935-0.00003-4.

- 10.3.9. **S.J. Mofokeng**, L.L. Noto, R.E. Kroon, O.M. Ntwaeaborwa and M.S. Dhlamini. *Up-conversion luminescence and energy transfer mechanism of ZnTiO₃: Er³⁺, Yb³⁺ phosphor*. Journal of Luminescence, March 2020, 117192, <https://doi.org/10.1016/j.jlumin.2020.117192>
- 10.3.10. **Sefako J. Mofokeng**, Luyanda L. Noto, Kingsly O. Obodo, Odireleng M. Ntwaeaborwa, Robin E. Kroon, and Mkhlotjwa S. Dhlamini. *Synthesis and up-conversion properties of Er³⁺ doped ZnTiO₃-Zn₂TiO₄ composite phosphor*. Journal of Vacuum Science & Technology B, Volume 38, 29 July 2020, 052802, <https://doi.org/10.1116/6.0000330>.
- 10.3.11. D.V. Mlotswa, L.L. Noto, **S.J. Mofokeng**, V.R. Orante-Baron, B.M. Mothudi. *Luminescence dynamics of MgGa₂O₄ prepared by solution combustion synthesis*, Optical Materials, Volume 109, November 2020, 11013, <https://doi.org/10.1016/j.optmat.2020.110134>.
- 10.3.12. **S.J. Mofokeng**, L.L. Noto and M.S. Dhlamini, *Photoluminescence properties of ZnTiO₃:Eu³⁺ phosphor with enhanced red emission by Al³⁺ charge compensation*. Journal of Luminescence (Accepted).

10.4. Research presentations

- 10.4.1. **S.J. Mofokeng**, V. Kumar, R.E. Kroon and O.M. Ntwaeaborwa. *Synthesis and characterization of Zinc Oxide-Titanium Dioxide nanocomposites co-doped with dysprosium and europium ion*. 5th Joint Symposium on Advanced Materials and Application, Korea Institute of Science and Technology (KIST), South Korea, 23 – 28 April 2016.
- 10.4.2. **S.J. Mofokeng**, V. Kumar, R.E. Kroon and O.M. Ntwaeaborwa. *Preparation and characterization of UV down-converting ZnO-TiO₂:Dy³⁺, Eu³⁺ nanocomposites*. 06th International Conference on Nanoscience and Nanotechnology, UNISA, South Africa, 03– 06 April 2016.

- 10.4.3. **S.J. Mofokeng**, V. Kumar, R.E. Kroon and O.M. Ntwaeaborwa. *Structure and optical properties of ZnO-TiO₂:Dy³⁺ nanocomposites*. 06th Annual Gauteng Nanosciences Young Researcher's Symposium (NYRS), Mintek, South Africa, 18 November 2016.
- 10.4.4. G.L. Kabongo, P.S. Mbule, G.H. Mhlongo, B.M. Mothudi, K.T. Hillie, **S.J. Mofokeng** and M.S. Dhlamini. *Investigation of ZnO:RE³⁺ nanostructures for efficient transfer in hybrid based P3HT heterostructures*. 07th South African Conference on Photonic Materials, UFS, South Africa, 27 -31 March 2017.
- 10.4.5. **S.J. Mofokeng**, L.L. Noto, K.O. Obodo, O.M. Ntwaeaborwa, B.M. Mothudi and M.S. Dhlamini. *Preparation of and evaluating Er³⁺ doped ZnTiO₃-Zn₂TiO₄ nanopshosphor prepared by conventional solid-state reaction*. 62nd Annual Conference of the South African Institute of Physics (SAIP), Stellenbosch University, South Africa, 03-07 July 2017.
- 10.4.6. **S.J. Mofokeng**, L.L. Noto, K.O. Obodo, O.M. Ntwaeaborwa, B.M. Mothudi and M.S. Dhlamini. *Up-conversion luminescence properties of Er³⁺/Yb³⁺ co-doped ZnTiO₃ nano-particles*. International Conference on Surfaces, Coatings and Nanostructured Materials (NANOSMAT-Africa) Cape Town, South Africa, 19-23 November 2018.
- 10.4.7. **Sefako J. Mofokeng**, Luyanda L. Noto, Dumisani V. Mlotswa, Mokhotjwa S. Dhlamini and Victor R. Orante-Baron. *Stimulated luminescence study of MgO:Al³⁺,Li⁺ prepared by solution combustion*. The 8th South African Conference on Photonic Materials (SACPM2019), Kariega Game Reserve, South Africa, 06-10 May 2019.